Environmental effects in the photophysics of cryogenic carbon nanotubes

Jonathan Christian Noé

München 2019

Environmental effects in the photophysics of cryogenic carbon nanotubes

Dissertation
an der Fakultät für Physik
der Ludwig-Maximilians-Universität
München

vorgelegt von
Jonathan Christian Noé
aus München, Deutschland

München, 23.01.2019

Erstgutachter: Prof. Dr. Alexander Högele
Zweitgutachter: Prof. Dr. Achim Hartschuh
Tag der mündlichen Prüfung: 28. März 2019

Zusammenfassung

Halbleitende Kohlenstoffnanoröhren sind eindimensionale Zylinder mit durchmesserabhängigen optischen Übergangen, die vom Nahinfraroten bis hin zu Telekom-Wellenlängen reichen. Nanoröhren haben potenielle Anwendung in der Quanteninformationsverarbeitung, da die stark gebundenen Elektron-Loch-Paare (Exzitonen) in kryogenen Nanoröhren als Einzelphotonenquellen dienen können. Aufgrund des großen Oberflächen-Volumen-Verhältnisses ist die Photolumineszenz von Kohlenstoffnanoröhren jedoch sehr anfällig für äußere Einflüsse, die zu Frequenz- und Intensitätsfluktuationen sowie zu einer Vielfalt von spektralen Emissionsprofilen führen können. Diese Effekte treten verstärkt bei tiefen Temperaturen auf, weil dort die Lokalisierung von Exzitonen dominiert. Aus diesem Grund ist es für die Implementierung von Kohlenstoffnanoröhren in quantenoptischen Anwendungen unerlässlich, die Wechselwirkung von Exzitonen mit der dielektrischen Umgebung der Nanoröhre zu verstehen und so deren optische Eigenschaften zu kontrollieren und unerwünschte Effekte zu eliminieren.

In Rahmen dieser Arbeit wurde die Photolumineszenz von Kohlenstoffnanoröhren mit Fokus auf die Auswirkung von äußeren Einflüssen wie Füllung, Ummantelung und Trägermaterial untersucht. Die Streuung der Photolumineszenzenergien von Tensid- und DNS-umantelten Nanoröhren konnte mit einer Verformung durch das Tensid beziehungsweise mit dem Auftreten von niederenergetischen Defektzuständen in Verbindung gebracht werden. Weder die Ummantelung noch das Füllen der Nanoröhre mit Wasser oder Alkan-Molekülen hatten Auswirkungen auf die spektrale Linienform oder die zeitliche Entwicklung der Photolumineszenz.

Im nächsten Schritt wurden die photophysikalischen Eigenschaften verschiedener Nanoröhren mithilfe der Photolumineszenz-Anregungsspektroskopie untersucht. Die Anregungsresonanzen in Nanoröhren mit delokalisierten Exzitonen traten gleichzeitg mit resonant verstärkter Ramanstreuung auf und wurden von Phononen verursacht, deren Energien zwar von der Chiralität der Nanoröhre, nicht aber von äußeren Einflüssen abhingen. Defektzustände in Nanoröhren erbten die Anregungsresonanzen von höherenergetischen Übergängen und zeigten keine resonante Verstärkung der Ramanstreuung, was auf die Lokalisierung der Exzitonen durch den Defekt zurückgeführt wurde. Die Anregungsresonanzen von quantenpunktähnlichen Emittern in gewachsenen Nanoröhren zeigten Phononsignaturen des Trägersubstrats, aber keine Nanoröhren-spezifischen Resonanzen. Basierend auf diesen Ergebnissen wurde ein Model entwickelt, das die verschiedenen Anregungscharakteristiken mit unterschiedlich starker Lokalisierung von Exzitonen in Verbindung bringt.

Zuletzt wurde der Ursprung spektraler Fluktuationen anhand eines Vergleichs der zeitlichen Entwicklung des Photlumineszenzsignals von kryogenen Nanoröhren auf verschiedenen Trägersubstraten untersucht. Die Photolumineszenz von Kohlenstoffnanoröhren auf hexagonalem Bornitrid war um eine Größenordnung stabiler als die auf Siliziumoxid, und damit vergleichbar mit der von freihängenden Nanoröhren in der Nähe eines dielektrischen Substrats, wohingegen komplett freihängende Nanoröhren stärkere spektrale Fluktuationen aufwiesen. Die gemessenen spektralen Rauschdichten wurde mit Simulationen interpretiert, die auf der Wechselwirkung des elektrischen Dipolmoments eines lokalisierten Exzitons mit fluktuierenden Oberflächenladungen des dielektrischen Trägersubstrats basierten. Aufgrund dieser Ergebnisse wurden Ladungsfluktuationen des Trägersubstrats als Ursache für spektrale Fluktuationen in der Photolumineszenz von Nanoröhren identifiziert und gleichzeitig das Potential von Elektrometern auf Basis von Nanoröhren verdeutlicht.

Abstract

Semiconducting carbon nanotubes are one-dimensional cylinders with diameter-dependent optical transitions that range from the near infrared up to telecom wavelengths and are governed by strongly bound electron-hole pairs (excitons). The discovery of single-photon emission from cryogenic carbon nanotubes identified them as potential candidates for quantum information processing. Their large surface-to-volume ratio renders nanotubes highly susceptible to the local environment which causes spectral diffusion, blinking, and a variety of spectral emission profiles in the photoluminescence, especially at cryogenic temperatures where exciton localization dominates the photophysical properties. For nanotube-based quantum optics applications, it is therefore crucial to understand the interactions of nanotube excitons with the environment to eliminate detrimental effects and control the photoluminescence properties.

In the framework of this thesis, the photoluminescence of cryogenic carbon nanotubes was studied with a focus on the influence of environmental factors such as nanotube filling, surfactant, and substrate. The spread in the cryogenic photoluminescence energies of surfactant-coated nanotubes was related to surfactant-induced strain and to the occurrence of low-energy defect states for nanotubes with sodium deoxycholate and deoxyribonucleic acid surfactants, respectively. Neither the photoluminescence spectral lineshape nor the spectral dynamics were found to be strongly influenced by the surfactant or by encapsulation of water or alkane molecules inside the nanotube.

The photophysics of different nanotube materials was studied by photoluminescence excitation spectroscopy. The photoluminescence excitation resonances of delocalized nanotube excitons were accompanied by enhanced Raman scattering and governed by intrinsic chiral-angle dependent phonons insensitive to the environment. Defect states in nanotubes inherited resonances from states with higher energy and did not enhance Raman scattering which was attributed to the defect-localization of excitons. Signatures of substrate-specific phonons were observed in the photoluminescence excitation of quantum dot-like excitons, for which most nanotube-specific resonances were absent. Based on these results, a model was proposed to relate the various photoluminescence excitation characteristics to different degrees of exciton localization.

To study the origin of spectral fluctuations at cryogenic temperatures, the time evolution of the photoluminescence from as-grown nanotubes on various substrates was investigated. The spectral stability of nanotubes on electrostatically calm hexagonal boron nitride was increased by over an order of magnitude as compared to nanotubes on silicon oxide and was comparable to suspended nanotubes near a dielectric support, whereas completely suspended nanotubes exhibited larger spectral fluctuations. The experimentally obtained noise spectral densities were modeled by simulations based on the interaction of the permanent electric dipole moment of localized nanotube excitons with fluctuating surface charges in the dielectric support. These results establish exciton localization combined with charge fluctuations as the origin of spectral diffusion in cryogenic nanotubes and demonstrate the potential of nanotube-based electrometers.

Contents

Chapter 1

Introduction

"There's plenty of room at the bottom – An invitation to enter a new field of physics." This is the title of the famous talk given by the theoretical physicist and Nobel prize laureate Richard P. Feynman at the annual meeting of the *American Physical Society* at the *California Institute of Technology* on December 29th 1959 [1]. In his contribution, Feynman sketched the enormous scientific, technological and economic potential he envisioned for material design and control below the micrometer-scale down to atomic dimensions. Today, almost six decades later, nanotechnology, referring to the investigation and manipulation of matter on the nanometer-scale (one thousandth of a micrometer or one billionth of a meter), has developed into a huge network of interdisciplinary scientific research areas, a growing source of technological applications (over 13000 patents worldwide in 2015)[1] and is the basis of a market expected to exceed the 125 billion dollar mark by 2024.[2] A key requirement for this outstanding growth was the discovery that scaling matter down to nanoscopic dimensions does not only offer advantages regarding miniaturization, but also fundamentally changes the characteristics of a solid state system. In contrast to macroscopic crystals, the chemical and physical properties of crystalline nanosystems are not solely determined by the chemical elements and the crystal structure, but strongly depend on the spatial extent and dimensionality. These additional material parameters determine the characteristics of numerous novel nanomaterials, of which carbon nanotubes (CNT) are one of the most versatile and remarkable representatives.

Carbon nanotubes are one-dimensional (1D) cylindrical crystals constructed from a hexagonal carbon lattice and were first experimentally observed in 1991 [2]. They exhibit huge aspect ratios with diameters below a few nanometers (nm) and length scales ranging from a few micrometers up to hundreds of millimeters [3] as well as outstanding thermal conductivity, tensile strength, and hardness [4, 5]. Depending on their crystalline structure, CNTs are either metallic or semiconducting with diameter-dependent optical tranistions in the near infrared, covering a spectral range of almost

[1] according to the European patent office.

[2] Global Nanotechnology Market (by Component and Applications), Funding & Investment, Patent Analysis and 27 Companies Profile & Recent Developments - Forecast to 2024

700 nm including the telecom wavelength [6, 7]. Consequently, CNTs are an attractive material for diverse optoelectronic and photonic applications [8] such as infrared photodetectors [9–11], photovoltaic cells [12–14], and light emitting diodes [15, 16]. Due to the decreased screening of the Coulomb interaction in 1D, the electronic excitations in CNTs are described by tightly-bound electron-hole pairs, known as excitons [17–19]. By virtue of exciton binding energies of several hundreds of millielectronvolts, the photophysical properties of a CNT are dominated by highly mobile excitons that diffuse along the CNT axis even at room temperature [20–24].

These findings are contrasted by the photoluminescence (PL) characteristics of CNTs at cryogenic temperatures where asymmetric and multi-peak PL spectra [25–27] were observed together with single-photon emission as a hallmark of exciton localization [28–32]. These phenomena were attributed to unintentional localization of excitons by disorder potentials of a few tens of millielectronvolts [33] that inhibit exciton diffusion and create a collection of strongly localized quantum dot-like exciton states. Similar results were achieved by the intentional incorporation of defects into the CNT lattice by covalent side-wall chemistry with oxygen [34–36] or aryl and alkyl groups [37, 38]. This approach allows the tuning of CNT PL properties and thereby achieved single-photon emission even at room temperature [39, 40] which is a crucial step towards the application of CNTs in quantum information processing. However, despite recent progress in engineering of the photophysical properties of CNTs, the main challenge regarding their usability in quantum optics applications is the great sensitivity of the CNT surface excitons to environmental influences that is enhanced for localized excitons due to the formation of a permanent electric exciton dipole moment that renders the PL susceptible to local and global electric fields [41, 42]. The resulting instabilities in the PL, such as spectral variations [25] and emission intermittence [43], can be reduced by freely suspending CNTs [30, 31] or embedding them in passive dielectric environments such as polymers [29]. A part of the dielectric environment that, despite its close vicinity to the localized CNT excitons, was neglected in most cryogenic PL studies are surfactant molecules. Surfactant agents such as micelles, polymers, or DNA are essential for dispersing CNTs in solutionl to obtain highly sorted CNT materials for a deterministic selection of PL emission energies [44], to functionalize CNTs [34, 35, 37–40, 45, 46], and to deposit CNTs on any desired substrate. Understanding the influence of the aforementioned factors is pivotal to control the photophysical properties of CNTs and to eliminate detrimental effects that impede the successful implementation of carbon nanotubes in future quantum optics technologies.

In this thesis, the various aspects of the cryogenic PL of different CNT materials are studied in varying dielectric environments to discriminate intrinsic CNT properties from environmental effects and characterize the influence of external factors on the low-temperature CNT photophysics. To this end, the dependence of the CNT PL energy, the photoluminescence excitation (PLE) resonances, and the spectral dynamics on the substrate, the surfactant, and the CNT filling were studied.

This thesis is structured as follows: Chapter 2 gives a brief summary of the crystal

structure and the electronic properties of single-wall carbon nanotubes and introduces the concepts of exciton PL, phonon modes and Raman scattering. The design and the specifications of the confocal microscope used for the cryogenic PL spectroscopy is presented in Chapter 3 together with a description of the studied CNT samples and their preparation.

Chapter 4 presents studies on the effect of water or alkane molecules inside pristine CNTs and the influence of CNT encapsulation by sodium deoxycholate (DOC) and DNA surfactant on the PL spectral lineshape and energy. The results are complemented by a comparison to room temperature absorption measurements of CNTs dispersed in solution.

The results of PLE spectroscopy of various CNT materials, including the CNT-specific phonon energies, are described in Chapter 5. To explain the large differences in the PLE characteristics among CNTs with symmetric, asymmetric and ultra-narrow spectral emission lineshapes, a toy model is developed based on the interactions of localized and delocalized CNT excitons with the local environment.

In Chapter 6, the time-dependent spectral fluctuations of cryogenic CNT PL are discussed in the framework of surface charge interactions with the permanent electric dipole moment of localized excitons. The results demonstrate the qualities of hexagonal boron nitride over silicon oxide as an electrostatically passive substrate. In addition, Monte Carlo simulations were employed to reproduce the substrate-specific spectral noise distributions and to relate PL spectral diffusion characteristics to substrate topography. Finally a summary of the obtained results is given in Chapter 7 together with possible directions of future research.

Chapter 2

Fundamentals of single-wall carbon nanotubes

This chapter presents fundamental geometrical, mechanical, electronic, and optical properties of single-wall carbon nanotubes. Based on the results of tight binding calculations in graphene, the electronic dispersion relation of one-dimensional carbon nanotubes is derived by zone folding. The reduced dimensionality leads to a geometry-dependent quantization of the allowed energy states and results in nanotubes with metallic or semiconducting character with diameter-dependent optical transitions energies. These transitions are dominated by the a diverging density of states at the band edges and are governed by tightly bound electron-hole pairs called excitons due to the reduced screening of Coulomb interactions in one dimension. Finally, the phonon spectrum of carbon nanotubes is discussed with a focus on Raman scattering.

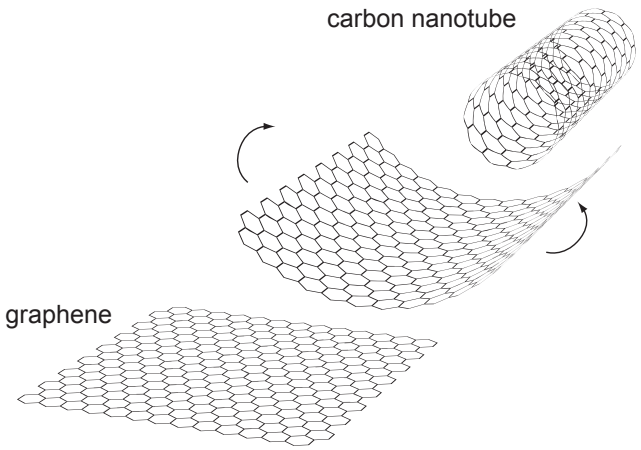

Figure 2.1: A carbon nanotube is constructed by rolling up a sheet of graphene to form a seamless cylinder.

2.1 The building block of carbon nanotubes: Graphene

As illustrated in Figure 2.1, a single-wall carbon nanotube (CNT) can be imagined as a sheet of graphene that is rolled up to form a seamless cylinder. For that reason, various properties of CNTs are inherited from graphene and only modified by the roll-up process. This section will discuss the crystal and electronic structure of graphene as the building block of CNTs.

2.1.1 Chrystal lattice and Brillouin zone

The electronic configuration of carbon in the atomic ground state is $1s^2 2s^2 2p^2$. In the crystalline phase it is, however, favorable to excite one electron from 2s to 2p, resulting in four valence electrons in the 2s, $2p_x$, $2p_y$, and $2p_z$ orbitals. A quantum mechanical superposition of the $2s$, $2p_x$, and $2p_y$ orbitals, called sp^2 hybridization, creates three covalent in-plane bonds to neighboring atoms. These σ-bonds with an angle of 120° form the two-dimensional (2D) hexagonal lattice of graphene shown in Figure 2.2a. The remaining electron in the p_z orbital, called π-electron, determines most of the electronic properties of graphene (see Section 2.1.2).

The real space unit vectors of the graphene lattice are given by [4]

$$\mathbf{a}_1 = \left(\frac{\sqrt{3}}{2}, \frac{1}{2}\right) \cdot a \,, \quad \mathbf{a}_2 = \left(\frac{\sqrt{3}}{2}, -\frac{1}{2}\right) \cdot a \,, \tag{2.1}$$

where $a = |\mathbf{a}_1| = |\mathbf{a}_2| = \sqrt{3} \cdot a_{C-C} = 2.46$ Å is the lattice constant of graphene and $a_{C-C} = 1.42$ Å is the distance between neighboring carbon atoms.[1] The unit cell spanned by $\mathbf{a}_1$ and $\mathbf{a}_2$ is indicated by the gray rhombus in Figure 2.2a. Because of the two carbon atoms in the unit cell, graphene can also be considered as the superposition of two sublattices

[1] In CNTs $a_{C-C} = 1.44$ Å due to curvature effects

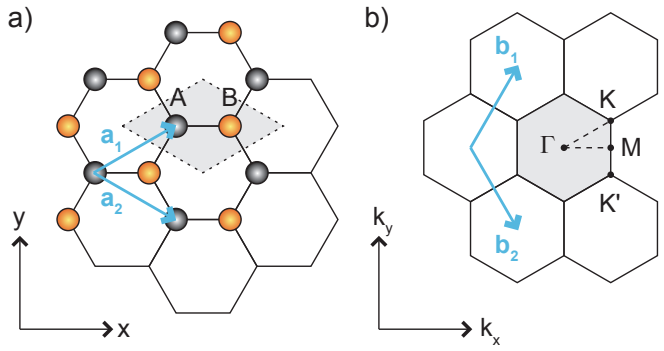

Figure 2.2: a) Graphene honeycomb lattice with unit vectors $\mathbf{a}_{1/2}$ (blue). Atoms belonging to different sublattices A and B are colored in gray and orange, respectively. The unit cell is indicated by the gray dashed rhombus. b) Corresponding reciprocal lattice with unit vectors $\mathbf{b}_{1/2}$. The gray hexagon is the graphene Brillouin zone with the high-symmetry points Γ, M, K, and K'.

A and B marked in gray and orange, respectively.

The reciprocal lattice of a crystal with unit vectors $\mathbf{a}_i$ is spanned by vectors $\mathbf{b}_i$ defined by the relation

$$\mathbf{a}_i \cdot \mathbf{b}_j = 2\pi\delta_{ij} \ , \tag{2.2}$$

where δ_{ij} is the Kronecker Delta. In the case of graphene, using Equation 2.1, this yields [4]

$$\mathbf{b}_1 = \left(\frac{1}{\sqrt{3}}, 1\right) \cdot \frac{2\pi}{a} \ , \ \mathbf{b}_2 = \left(\frac{1}{\sqrt{3}}, -1\right) \cdot \frac{2\pi}{a} \ . \tag{2.3}$$

Figure 2.2b depicts the reciprocal lattice of graphene spanned by $\mathbf{b}_1$ and $\mathbf{b}_2$ (blue) including the first Brillouin zone (BZ) of graphene (gray hexagon) with the high-symmetry points Γ, M, K, and K'.

2.1.2 Electronic structure

The electronic properties of graphene near the Fermi level are determined by the π-electrons of the two non-equivalent carbon atoms in the graphene unit cell mentioned in Section 2.1.1. A bonding (π) and an antibonding (π^*) quantum mechanical superposition of these orbitals forms the low-energy valence and conduction band of 2D graphene, respectively. According to the simple tight-binding approach for the π orbitals described in Ref. [4], the energy dispersion relation of graphene is calculated as

$$E_{\mathrm{g2D}}(\mathbf{k}) = \frac{\epsilon_{2p} \pm \gamma_0 \omega(\mathbf{k})}{1 \pm s\omega(\mathbf{k})} \ , \tag{2.4}$$

where the + and - sign correspond to the valence and the conduction band, respectively. The function $\omega(\mathbf{k})$ is given by

$$\omega(\mathbf{k}) = \sqrt{1 + 4\cos\frac{\sqrt{3}k_x a}{2}\cos\frac{k_y a}{2} + 4\cos^2\frac{k_y a}{2}} \ . \tag{2.5}$$

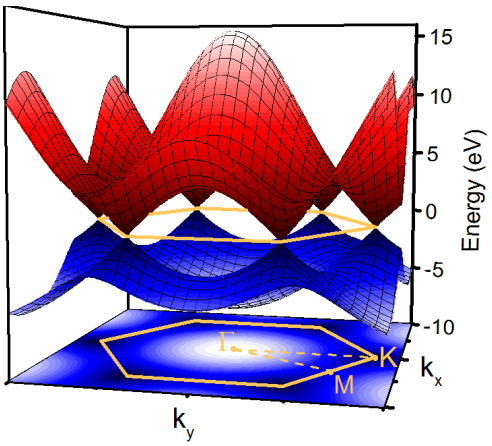

Figure 2.3: Energy dispersion relation of graphene. The valence band (blue surface) and the conduction band (red surface) are degenerate at the K and K' points of the first Brillouin zone (orange hexagon). The bonding π-band is projected onto the k_x, k_y-plane at the bottom.

Figure 2.3 shows the dispersion relation of graphene according to Equation 2.4 using the parameters $\epsilon_{2p} = 0$, $\gamma_0 = -3.033$ eV, and $s = 0.129$ [4]. The valence and the conduction band are degenerate at the K and K' points at the boundary of the first BZ. The density of states at these points is zero and therefore graphene is a semi-metal or zero-gap semiconductor. Since the energy dispersion relation is linear near the K and K' points, electronic excitations in graphene can be described as massless pseudo-relativistic particles.

The most relevant modifications of the graphene characteristics in CNTs are caused by the reduced dimensionality. As a consequence quantum mechanical periodic boundary conditions are imposed on the wavefunctions along the CNT circumference, which strongly modifies the electronic and vibrational properties obtained for graphene. The rest of this chapter will focus on the properties of CNTs.

2.2 Chrystal structure

A single-wall CNT can be considered as a graphene sheet rolled up to form a cylinder with a diameter between 0.7 – 10.0 nm, whereby the direction of the rolling-up with respect to the graphene lattice is determined by the chiral vector $\mathbf{C}_h$ that determines the CNT properties. The chiral vector $\mathbf{C}_h$ runs along the CNT circumference and is perpendicular to its axis. It is constructed from multiples of the graphene lattice vectors (Equation 2.1) as

$$\mathbf{C}_h = n \cdot \mathbf{a}_1 + m \cdot \mathbf{a}_2 \equiv (n, m) \tag{2.6}$$

where n and m are integers with $0 \leq m \leq n$. The intrinsic properties of a CNT are completely defined by its chiral vector and (n, m) is also referred to as the chirality of a CNT. The diameter of a CNT, which strongly affects the optical properties of semiconducting

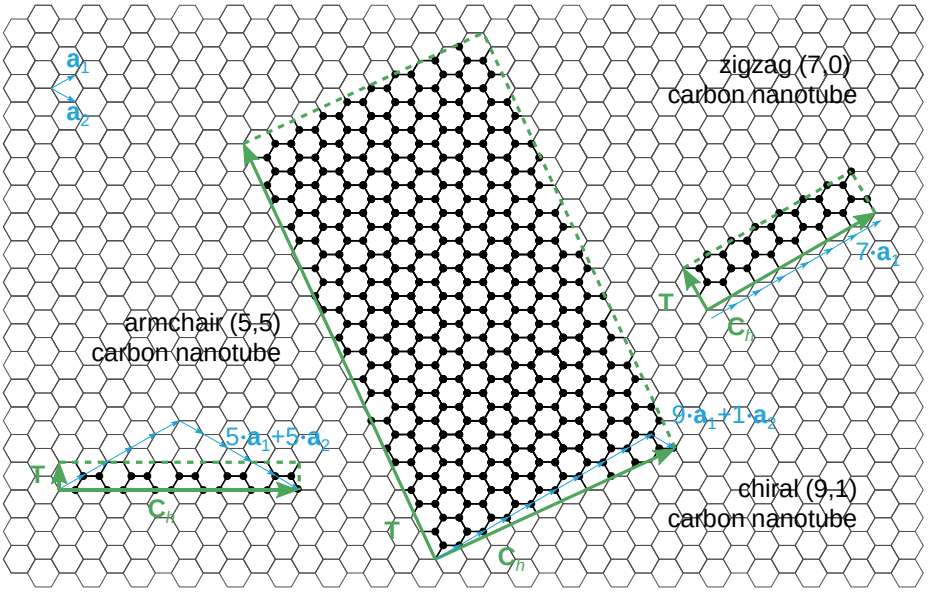

Figure 2.4: Schematic construction of CNTs from a graphene sheet. A nanotube chirality is defined by the chiral vector $\mathbf{C}_h$, a linear combination of the graphene lattice vectors $\mathbf{a}_1$ and $\mathbf{a}_2$ (blue arrows in the upper left corner). The CNT is constructed by rolling up the graphene ribbon along $\mathbf{C}_h$ to a seamless cylinder. The translation vector $\mathbf{T}$ and the chiral vector $\mathbf{C}_h$, indicated by green arrows, span the CNT unit cell. Depicted examples are an armchair (5,5), a zigzag (7,0), and a chiral (9,1) CNT.

CNTs (see Section 2.3), is determined by the chirality as

$$d_t = \frac{|\mathbf{C}_h|}{\pi} = \frac{a}{\pi}\sqrt{n^2 + nm + m^2} \ . \tag{2.7}$$

Another structural parameter is the chiral angle θ between $\mathbf{C}_h$ and the graphene lattice vector $\mathbf{a}_1$. It denotes the tilt angle of the carbon hexagons with respect to the CNT axis and only takes values in the range $0° \leq \theta \leq 30°$ due to the hexagonal symmetry of the graphene lattice. It is expressed by the relation

$$\cos\theta = \frac{\mathbf{C}_h \cdot \mathbf{a}_1}{|\mathbf{C}_h| \cdot |\mathbf{a}_1|} = \frac{2n+m}{2\sqrt{n^2 + nm + m^2}} \ . \tag{2.8}$$

Achiral CNTs with $\theta = 0°$ or $\theta = 30°$ have a higher symmetry as compared to chiral CNTs and are referred to as armchair (n,n) or zigzag $(n,0)$ nanotubes, respectively, due to the characteristic pattern along their chiral vectors.

Carbon nanotubes are one-dimensional lattices with cylindrical unit cells, since translational invariance only exists along one axis. The unit vector of this lattice is the translational vector $\mathbf{T}$, defined as the smallest combination of graphene lattice vectors that is perpendicular to $\mathbf{C}_h$ [4]

$$\mathbf{T} = \frac{2m+n}{d_R} \cdot \mathbf{a}_1 - \frac{2n+m}{d_R} \cdot \mathbf{a}_2 \ , \tag{2.9}$$

where d_R is the greatest common divisor of $2n+m$ and $2m+n$. Figure 2.4 depicts the

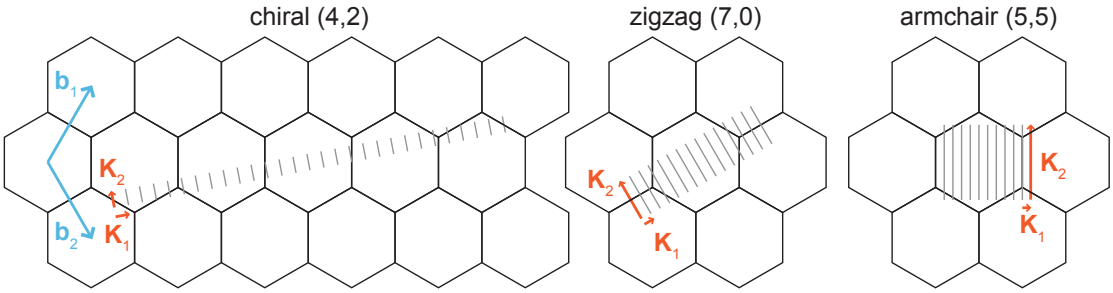

Figure 2.5: Hexagonal reciprocal graphene lattice including the reciprocal lattice vectors $\mathbf{b}_1$ and $\mathbf{b}_2$ of graphene (blue), and $\mathbf{K}_1$ and $\mathbf{K}_2$ of a (4,2), (7,0), and (5,5) CNT (orange). The one-dimensional first Brillouin zones of the CNTs are depicted as gray lines along $\mathbf{K}_2$. Quantization of the wave vector along the CNT circumference gives rise to N lines.

unrolled unit cells of a (5,5) armchair, a (9,1) chiral, and a (7,0) zigzag CNT that are spanned by $\mathbf{T}$ and $\mathbf{C}_h$ and contain N hexagons (black), with

$$N = \frac{|\mathbf{C}_h \times \mathbf{T}|}{|\mathbf{a}_1 \times \mathbf{a}2|} = \frac{2\left(n^2 + nm + m^2\right)}{d_R} \quad . \tag{2.10}$$

Using Equations 2.2, 2.3, 2.6, and 2.9, the reciprocal lattice vectors of a CNT are calculated as [4]

$$\mathbf{K}_1 = \frac{2n+m}{Nd_R}\mathbf{b}_1 + \frac{2m+n}{Nd_R}\mathbf{b}_2 \,, \quad \mathbf{K}_2 = \frac{m}{N}\mathbf{b}_1 - \frac{n}{N}\mathbf{b}_2 \,, \tag{2.11}$$

where $\mathbf{K}_1$ and $\mathbf{K}_2$ correspond to the chiral vector $\mathbf{C}_h$ and the translational vector $\mathbf{T}$, respectively. Both vectors are depicted in Figure 2.5 (orange) together with the reciprocal lattice vectors of graphene (blue). In the limit of an infinitely long CNT, wave vectors along the CNT axis, i.e. along $\mathbf{K}_2$, can take continuous values. Wave vectors along the circumference of the CNT, however, have to fulfill the periodic boundary condition

$$k_\perp = \mu \frac{2\pi}{|\mathbf{C}_h|} \quad . \tag{2.12}$$

The N wave vectors with $\mu = -\frac{N}{2}+1, \ldots, \frac{N}{2}$ all have non-equivalent positions with respect to the reciprocal lattice of graphene. Therefore, the 1D first Brillouin zone of a CNT consists of N equidistant lines as shown in Figure 2.5 for the example of a chiral (4,2), a zigzag (7,0), and an armchair (5,5) nanotube. Depending on the chirality (n,m), one of the N lines may include the K and K' point of the graphene BZ, which strongly affects the electronic properties of a CNT as discussed in the next section.

2.3 Band structure and optical band-to-band transitions

The electronic structure of CNTs can be derived from the electron dispersion relation of graphene discussed in Section 2.1.2 by the so-called zone-folding approach [4]. The dispersion relations along the N cutting lines shown in Figure 2.5 are then given by

$$E_\mu(k) = E_{g2D}\left(k\frac{\mathbf{K}_2}{|\mathbf{K}_2|} + \mu\mathbf{K}_1\right) \ , \ (\mu = 0, \ldots, N-1, \text{ and } -\frac{\pi}{|\mathbf{T}|} < k < \frac{\pi}{|\mathbf{T}|}) \ , \tag{2.13}$$

where $E_{g2D}(\mathbf{k})$ is the electron dispersion relation of graphene from Equation 2.4 and $\mathbf{K}_1$ and $\mathbf{K}_2$, $\mathbf{T}$ and N are given by Equations 2.11, 2.9, and 2.10, respectively. Folding these N dispersion relations to overlap with each other yields the 1D electronic band structure of a CNT. If one of the N cutting lines contains the K or K' point of the graphene BZ, the corresponding CNT is metallic. This condition is fulfilled for all armchair CNTs and more generally for all nanotubes with $(2n+m)\text{mod}3 = 0$. All other CNTs have a finite band gap and are therefore semiconducting. Since most of the results presented in this work were obtained by photoluminescence (PL) spectroscopy, which requires a non-zero band gap, the rest of this chapter will focus on semiconducting CNTs.

In addition to the band structure, the optical properties of a material are also determined by the density of states $D(E)$, that describes the number of states available in the energy interval $E + \Delta E$. In 1D systems with a parabolic dispersion relation, such as CNTs, $D(E)$ scales with $1/\sqrt{E}$. This scaling leads to a diverging density of states (DOS) at each energy band edge, known as Van Hove singularities (VHs), with a strongly enhanced optical transition probability. Figure 2.6a shows the first two VHs in the DOS (gray) of a semiconducting CNT. The VHs in the conduction and the valence band are numbered according to their order starting with the VHs at the band gap (c_1 and v_1, respectively). According to symmetry-based selection rules, an optical transition E_{ij} between the VHs of the i-th valence and the j-th conduction band is allowed if $i - j = 0$ or $i - j = \pm 1$ for light polarized along and perpendicular to the CNT axis, respectively, as illustrated in Figure 2.6a. However, due to a strong depolarization effect [47], optical excitation polarized perpendicular to the CNTs axis is suppressed [48], especially for small-diameter CNTs. By linearizing Equation 2.4 and Equation 2.5 near the K point, following the approach in Ref. [49], one finds that the energy of the E_{11} transition of semiconducting nanotubes depends on the CNT diameter as

$$E_{11}(d_t) = \frac{2a_{\text{C-C}}\gamma_0}{d_t} \ . \tag{2.14}$$

However, this approach does not consider curvature effects and deviations from the graphene bond length $a_{\text{C-C}}$. Therefore, it fails to fully reproduce experimental results, especially in the case of small-diameter CNTs for which these effects are most pronounced. A more accurate prediction of the E_{11} and E_{22} energies was achieved by empirical formulas presented in Ref. [50]. Using the results from this work the empirical Kataura plot depicted in Figure 2.6b was created showing the CNT transition energies as a function

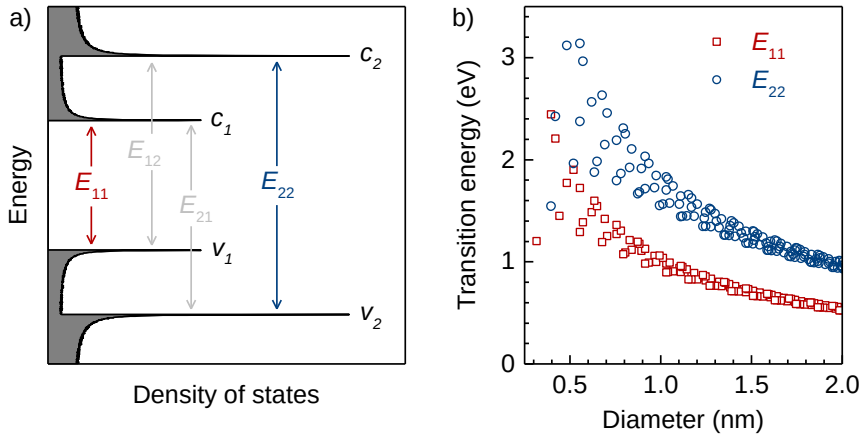

Figure 2.6: a) Density of states (gray) of a semiconducting CNT near the band gap. Starting from the band gap, the ith van Hove singularity (VHs) is marked with c_i and v_i for conduction and valence band, respectively. Red and blue arrows and light gray arrows mark optical transitions allowed for light polarized along and perpendicular to the CNT axis, respectively. b) Empirical Kataura plot of the transitions energies E_{11} and E_{22} of semiconducting single-wall CNTs as a function of the nanotube diameter d_t. Data points are predictions from the empirical fitting functions of Ref. [50].

of their diameter [51]. Here, the experimentally observed broadening in the energy distribution of CNTs with diameters below 1 nm is reproduced by using different formulas for semiconducting CNTs with $(2n-m)\text{mod}3 = 1$ and 2, respectively.

For large diameter nanotubes, a E_{22}/E_{11} ratio of about 1.75 was found experimentally [7], whereas a ratio of two was predicted by theory in the framework of free electrons and holes. This so-called "ratio problem" is resolved when electron and holes are not treated as free particles, but as states bound by Coulumb interaction called excitons [52]. The properties of these quasi-particles and their effect on the optical properties of CNTs are discussed in the next section.

2.4 Exciton photoluminescence

Photoluminescence refers to the radiative recombination of electrons and holes after optical excitation. So far, electrons and holes were described as non-interacting particles, which is a valid assumption for most conventional semiconductors at non-cryogenic temperatures. In contrast to three-dimensional bulk semiconductors, however, an enhanced Coulomb interaction between excited electron-hole pairs is expected for 1D CNTs [54]. Therefore, the electronic excitations in CNTs are more accurately described in the framework of tightly bound electron-hole pairs forming hydrogen-like states called excitons. First experimental evidence of these quasiparticles was found by two-photon absorption specroscopy [18, 19, 55]. In the single-particle picture, two-photon excitation with a photon energy $\hbar\omega_{\text{ex}}$ will be followed by the emission of one photon with energy $\hbar\omega_{\text{em}} = 2\hbar\omega_{\text{ex}}$ as illustrated in the energy diagram in Figure 2.7a. The discrete hydrogen-like energy levels of an exciton shown in Figure 2.7b, on the other hand,

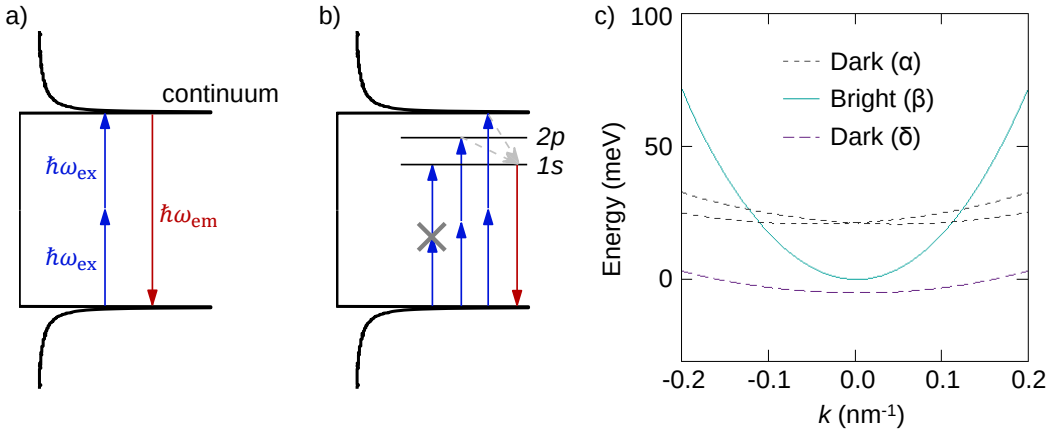

Figure 2.7: Schematic representation of the CNT density of states and a two-photon absorption process (blue arrows) followed by one-photon emission (red arrow) in the single particle and the exciton picture (a and b, respectively). In the exciton picture the $1s$ state is not accessible via two-photon excitation (gray cross). Energy relaxation from higher states to the exciton ground state $1s$ is indicated by gray dashed arrows. c) Singlet exciton energy bands of a (9,4) CNT. With respect to one-photon transitions, the finite angular momentum bands (α) and the zero angular momentum state of even parity (δ) are dark. The only optically active state is the zero angular momentum state with odd parity (β). Adapted from Ref. [53]

are not accessible for one-photon and two-photon processes simultaneously due to changing parity. The found mismatch between two-photon excitation and one-photon emission energies ($\hbar\omega_{em} < 2\hbar\omega_{ex}$) is therefore a direct proof of exciton PL [18]. The energy difference between the first VHs and the exciton ground state is the exciton binding energy E_B. Values of several hundred milli-electronvolts (meV) found for E_B in CNTs, compared to several tens of meV in bulk semiconductors, show that the photophysical properties of CNTs are dominated by excitonic effects even at room temperature. In addition to the formation of excitons, the strong Coulomb interaction in 1D renormalizes the energy of the band gap by E_{BGR}. Therefore the lowest optical tranistion energy is [56]

$$E_{opt} = E_{SP} + E_{BGR} - E_B \ , \tag{2.15}$$

where E_{SP} is the energy of the corresponding VHs in the single-particle picture. The transition energies observed in experiments, however, do not deviate much from the results calculated in the single-particle framework, since the contributions of E_{BGR} and E_B almost compensate each other [57]. In CNTs, only one exciton state is optically active (bright),[2] even though the degeneracy of the K and K' points together with the spin degree of freedom, give rise to 16 exciton states. Twelve of these states are, however, triplets with non-zero spin and therefore optically inactive (dark) [58]. Figure 2.7c shows the energy dispersion of the remaining four singlet states for the example of a (9,4) CNT [53]. Two singlet states are intervalley excitons consisting of an electron at K and a

[2] Considering one-photon transitions

hole at K' or vice versa (α). These states have finite angular momentum and therefore do not couple to photons. The remaining intravalley singlet states hybridize due to short range Coulomb interaction and form a bonding and an antibonding superposition $K^{\pm} = \frac{1}{\sqrt{2}}\left(|KK\rangle \pm |K'K'\rangle\right)$. The singlet state with the lowest energy K^{-} (δ) is dark due to even parity and only the bonding odd-parity state K^{+} (β) is optically active. Throughout this thesis, E_{11} will refer to the optical active exciton transition. The parity-forbidden singlet state and the spin-forbidden triplet states have a lower energy as compared to the bright exciton [59, 60]. Hence, non-radiative decay of excitons into these states may be a major reason for the low PL quantum yield of CNTs [61].

2.5 Phonon modes and Raman scattering

The energy and momentum of the vibrational quanta in solid state crystals, called phonons, are determined by the crystal lattice. Phonons with a linear dispersion relation $\omega(k)$ near the Γ point of the BZ and with $\omega(k=0)=0$ are termed acoustic phonons. They represent the 3 possible in-phase vibrations of all atoms in the unit cell. In 1D systems like CNTs an additional acoustic phonon mode exists that corresponds to the rotation or "twisting" around the CNT axis. Unit cells containing M atoms give rise to additional $3M-3$ optical phonons that correspond to the out-of-phase vibrations of the atoms in the unit cell and are characterized by a finite energy at $k=0$. Due to the additional acoustic phonon, only $3M-4$ optical phonons exist in CNTs [4].

Similar to the electronic bands in Section 2.3, the phonon structure of CNTs can be obtained from the phonon dispersion relations of graphene shown in Figure 2.8a. The result for a (10,10) CNT, calculated in Ref. [62], is shown in Figure 2.8b. Corresponding to the two carbon atoms in the unit cell, $3M=6$ phonon modes exist in graphene: The out-of-plane transverse acoustic (oTA), the in-plane transverse acoustic (iTA), the longitudinal acoustic (LA), the out-of-plane transverse optic (oTO), the in-plane transverse optic (iTO), and the longitudinal optic (LO). Due to the large number of carbon atoms per CNT unit cell, the number of phonon modes can be very large compared to 2D or 3D crystals, depending on the CNT chirality. Following Equation 2.10, the studied chiral (9,1) and (6,5) CNTs, both exhibit 1092 phonon branches. In this work, however, the concepts of CNT phonons will only be used in the framework of Raman scattering processes in Chapter 5. This greatly reduces the number of relevant phonon modes, because only few CNT phonons are Raman active due to symmetry. Chiral (9,1) and (6,5) CNTs are described by the D_N symmetry group and have 15 first-order Raman active phonon modes [63] with A, E_1, and E_2 symmetry.[3]

A first-order Raman process is the inelastic scattering of a photon with energy $\hbar\omega_{\mathrm{L}}$ by a single phonon with energy $\hbar\omega_{\mathrm{ph}}$ in a molecule or solid. The energy of the scattered photon $\hbar\omega_{\mathrm{scat}}$ is given by energy conservation

$$\hbar\omega_{\mathrm{scat}} = \hbar\omega_{\mathrm{L}} \mp \hbar\omega_{\mathrm{ph}} \ , \tag{2.16}$$

[3] Basis functions: x^2+y^2, z^2; $yz-zx$; and $xx-yy, xy$ for A, E_1, and E_2 symmetry, respectively

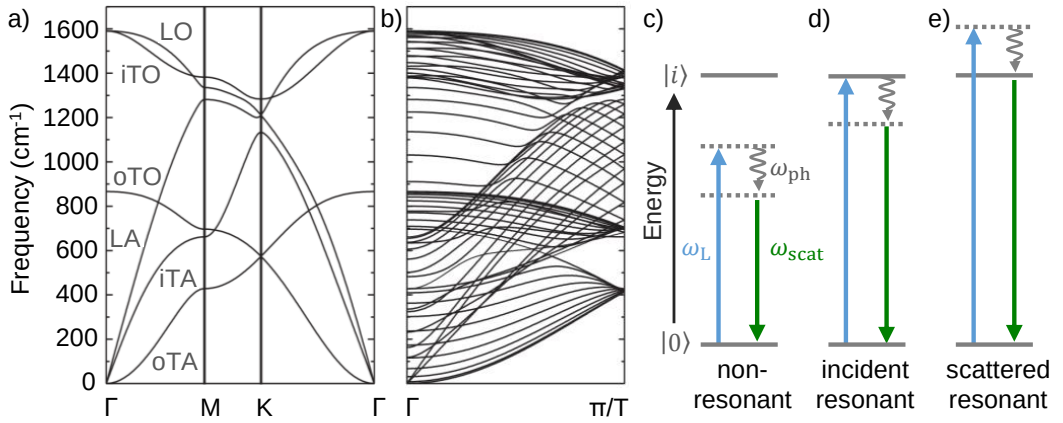

Figure 2.8: a) Phonon dispersion of graphene. The phonon branches are labeled: out-of-plane transverse acoustic (oTA), in-plane transverse acoustic (iTA), longitudinal acoustic (LA), out-of-plane transverse optic (oTO), in-plane transverse optic (iTO), and longitudinal optic (LO). b) Calculated phonon dispersion relations of a (10,10) CNT using the zone folding procedure. Adapted from Ref. [62]. c-e) Schematic energy diagram of three Raman scattering processes. Laser exciation with energy $\hbar\omega_{\mathrm{L}}$ (blue) from the ground state $|0\rangle$ is followed by the emission of a phonon with energy $\hbar\omega_{\mathrm{ph}}$ (gray wiggled arrow) and subsequent emission of the low-energy Raman photon with energy $\hbar\omega_{\mathrm{scat}}$ (green). In a non-resonant Raman processes (c) all involved excited states are virtual (gray dashed lines). If the photon is absorbed or emitted at an exciton state $|i\rangle$ of the CNT, the Raman process is termed incident resonant (d) or scattered resonant (e), respectively.

where the minus and the plus sign correspond to the creation (Stokes) and the annihilation (anti-Stokes) of a phonon, respectively. The amplitude of anti-Stokes scattering depends on the number of thermally excited phonons in the involved phonon mode. At a temperature T, the number of thermally excited phonons n in the μ-th phonon mode with wave vector q is given by the Bose Einstein statistics

$$n(q,\mu) = \frac{1}{\exp\left(\hbar\omega_{\mathrm{ph}}(q,\mu)/k_{\mathrm{B}}T\right)-1} \quad . \tag{2.17}$$

In all cryogenic Raman studies in this work $n(q,\mu)$ was approximately zero and therefore only Stokes Raman scattering is considered in the following.

Figure 2.8c-e shows the schematic energy diagrams of three Raman Stokes processes. In the case of the non-resonant Raman scattering in Figure 2.8c, a laser photon with energy $\hbar\omega_{\mathrm{L}}$ (blue) is absorbed by a virtual state (dashed line), decays into a lower virtual state via the emission of a phonon with energy $\hbar\omega_{\mathrm{ph}}$ (gray wiggled arrow) and decays radiatively by emitting a photon with energy $\hbar\omega_{\mathrm{scat}}$ (green). If one of the excited states coincides with an exciton state $|i\rangle$ of the CNT, the Raman scattering is termed incident (Figure 2.8d) or scattered resonant (Figure 2.8e), respectively. Considering only the $i-$th optical transition $|i\rangle$ with energy E_i of a CNT, the Stokes Raman intensity I_i can be

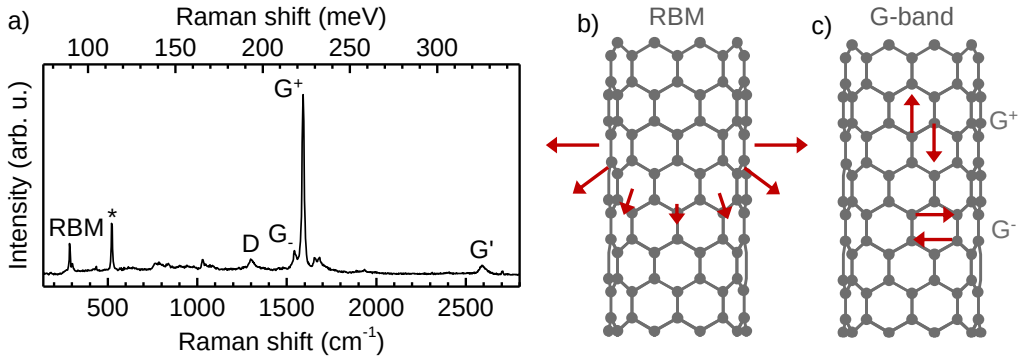

Figure 2.9: a) Raman spectrum of a CNT. The most prominent Raman signatures are the radial breathing mode (RBM), the defect-induced D-mode, the tangential G-band (composed of G^+ and G^-) and the overtone of the D-mode G'. The Raman peak labeled with the asterisk stems from the silicon substrate. b) and c) Illustrations of the CNT lattice vibrations for the RBM and G-band, respectively. The RBM corresponds to a radial in-phase vibration of all carbon atoms. Stretching of the C-C bonds along the CNT axis and along its circumference corresponds to the G^+ and G^- band, respectively.

expressed as a function of the laser excitation energy E_L by

$$I_i(E_\mathrm{L}) \propto \left| \frac{M_{\text{ex-op}}(a) M_{\text{ex-ph}}(a \rightarrow b) M_{\text{ex-op}}(b)}{\left[E_\mathrm{L} - E_i + i\gamma\right]\left[E_\mathrm{L} - E_i - \hbar\omega_{\text{ph}} + i\gamma\right]} \right|^2 , \tag{2.18}$$

with the exciton-photon matrix element $M_{\text{ex-op}}$ and the exciton-phonon matrix element $M_{\text{ex-ph}}$ as defined in Ref. [64]. The exciton states before and after the scattering event are denoted by a and b, respectively. From the denominator of Equation 2.18, it can be seen that the Raman intensity is strongly enhanced when one of the resonance conditions in Figure 2.8d or e is fulfilled. The resonance is finite due to the resonance width γ associated with the finite lifetime of the scattering event corresponding to an energy of the order of 60 meV [65]. It has to be noted that, even if a process is Raman active, its scattering amplitude can be vanishingly small and therefore not detectable. The vanishing photon momentum only allows coupling to phonons near the Γ point of the BZ with wave vector $\mathbf{q} = 0$ in first-order Raman processes. In second-order Raman processes, however, also phonons at the K and K' points with $\mathbf{q}$ and $-\mathbf{q}$ can take part in the scattering event. Second-order Raman scattering involves either two phonons, such as overtones and combination modes, or a phonon and a crystal impurity, like the Raman defect-mode in CNTs and graphene.

Figure 2.9a shows the Raman spectrum of a CNT with first-order and second-order, one- and two-phonon Raman modes. The three first-order modes are the radial breathing mode (RBM), the G^--, and the G^+-band. The RBM is only observed in CNTs and corresponds to an in-phase oscillation of all carbon atoms in radial direction as illustrated in Figure 2.9b. Its frequency is calculated as $\omega_{\text{RBM}}[\mathrm{cm}^{-1}] = \frac{277}{d_t[\mathrm{nm}]}\sqrt{1 - C d_t^2[\mathrm{nm}^2]}$ where C describes interactions with the environment [66]. The dependence on the diameter comes from the fact, that the combined mass of all carbon atoms along the

circumferential direction depends on the CNT diameter. The G-band is an in-plane stretching mode present in all sp^2-hybridized carbon materials, that is split in CNTs due to the symmetry breaking caused by the rolling-up of the graphene sheet (Figure 2.9c). The Raman mode corresponding to a bond-stretching along the CNT axis is called G^+ and has an energy of about 1590 cm^{-1} (199 meV) independent of the CNT diameter. The G^- mode with lower energy is related to in-plane stretching along the CNT circumference and consequently depends on the nanotube diameter [67]. The defect-induced D-band is a second-order one-phonon Raman mode with an energy around 1300 cm^{-1} (160 meV) [62]. In this Raman process, the exciton is scattered by a phonon with momentum $\mathbf{q}$ and the momentum $-\mathbf{q}$ to compensate the photon-phonon momentum mismatch is provided by a defect in the CNT lattice. Therefore, the occurrence of the D-mode is an indicator for defects or impurities in the CNT lattice and the ratio of the G^+-band and D-band Raman intensities is often used as a measure for the purity of CNT materials [68–71]. The G'-band around 2600 cm^{-1} (320 meV) is a second-order two-phonon process, namely the overtone of the D-band. In contrast to its first harmonic it is also observable in the absence of lattice impurities. Next to these dominant phonon modes, several combination modes involving acoustic and optical phonons exist in the energy range between the RBM and the G-band, called the intermediate frequency modes (IFM) [62]. The origin of the IFM modes and of further second-order Raman features above the G-band will be discussed in more detail in Section 5.3.

Chapter 3

Experimental methods

Photoluminescence spectroscopy was performed in a home-built confocal microscope at 300 K and 4.2 K. To optically excite individual carbon nanotubes, a titanium-sapphire laser was focused to a diffraction-limited spot onto the samples with an apochromatic objective optimized for the near infrared wavelengths of the experiment. The photoluminescence signal was dispersed using a monochromator and detected by silicon-based photodetectors.

Samples were prepared either by direct growth of carbon nanotubes using chemical vapor deposition or by drop-casting nanotubes dispersed in solution. Small-diameter nanotubes were grown over trenches, on silicon oxide, and on hexagonal boron nitride. Chirality-sorted pristine (9,1) and alkyl-doped (6,5) carbon nanotubes with sodium deoxycholate and DNA surfactants, filled with water or alkane molecules, were applied to a fused silica solid immersion lens by drop-casting.

3.1 Confocal microscopy setup

Optical excitation of carbon nanotubes (CNT) for confocal microscopy was performed by a titanium-sapphire laser,[1] that was tunable in wavelength in the range of 685 – 1000 nm. The laser was operated in continuous wave (cw) mode. The output power was stabilized and regulated using a home-built intensity stabilization based on an acousto-optic modulator. A detailed description of the stabilization setup can be found in Ref. [72]. The intensity-stabilized laser beam was coupled into an optical single-mode fiber and guided to the horizontal excitation arm of the confocal microscope depicted in Figure 3.1, where the laser beam (blue) was collimated. Photons generated by Raman processes in the optical fiber were removed by a short-pass filter. The following beam sampler with anti-reflective coating split the excitation beam into a reflected part directed towards the sample and a transmitted part, whose intensity was measured by a photodiode and served as reference value for the laser stabilization.[2] After the beam sampler, the reflected light passed either a half-wave plate ($\lambda/2$) to change the polarization direction or a quarter-wave plate ($\lambda/4$) to obtain circular polarization. Measurements on individual CNTs were conducted in linear polarization oriented along the CNT axis to maximize the photoluminescence (PL) signal. Two-dimensional raster scans were recorded with circular polarized excitation to be sensitive to all CNTs independent of their orientation.

The sample holder and the low-temperature apochromatic objective[3] were mounted inside a steel tube with a vacuum-sealed anti-reflection-coated window for optical access. A confocal spot size of ~1.1 µm was achieved with the objective for near-infrared wavelengths. After mounting the sample on the sample holder, the tube was evacuated to a pressure below $8 \cdot 10^{-5}$ mbar and subsequently filled with helium gas (~25 mbar) for an efficient thermal coupling of the sample to the liquid helium (4.2 K) bath for cryogenic measurements. Piezo-slip-stick steppers[4] and piezo-scanners[5] were used to position the sample in all three spatial directions.

The reflected laser light and the PL signal from the sample were collected by the objective and passed the microscope towards the vertical detection arm. A fraction of the light was deflected by a second beam sampler and focused onto a charged-coupled device (CCD) camera to image the confocal spot for alignment of the microscope or the sample surface for orientation on the sample. The scattered laser light was filtered from the transmitted beam by a long-pass filter. Depending on the experimental wavelength range, two different combinations of short- and -long-pass filters were used (858 nm/860 nm and 898 nm/900 nm). The filtered beam was coupled into a single-

[1] *Coherent* Mira 900 pumped by a Verdi-V10 laser diode

[2] The splitting ratio depends on the polarization of the incident light that was controlled by the three polarization paddles. Experiments were performed with an s-polarized beam that maximized the reflection (reflected to transmitted intensity 10/90 for an incident angle of 45 °).

[3] *attocube systems* LT-APO/NIR/075 with numerical aperture NA=0.75 and an apochromatic range of 700 – 980 nm

[4] *attocube systems* ANPx100 (2x) and ANPz101

[5] *attocube systems* ANSxy100

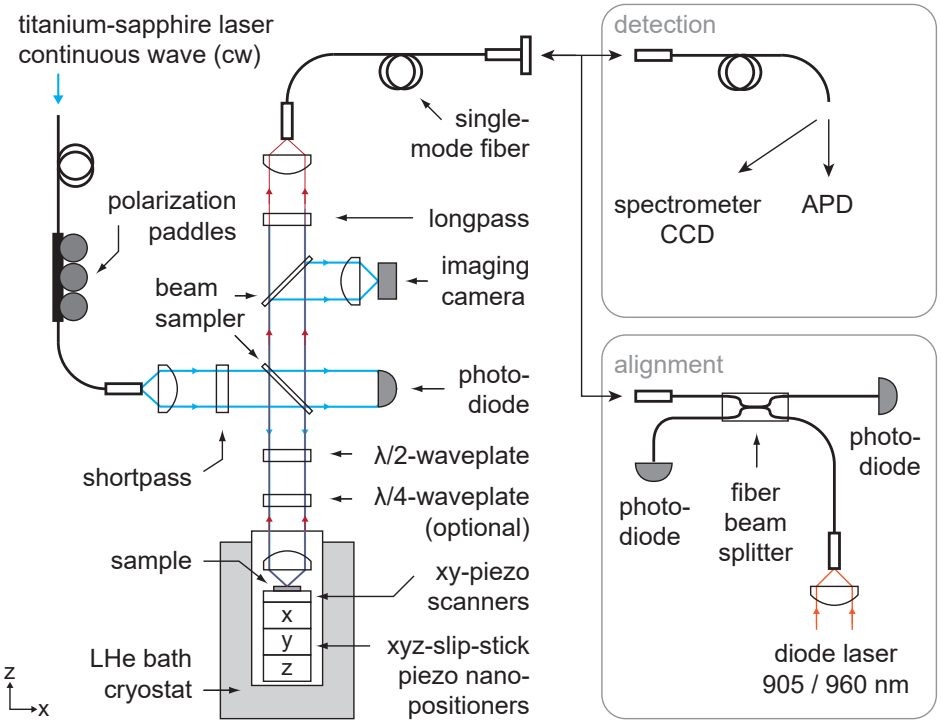

Figure 3.1: Schematic of the cryogenic confocal microscope setup. A single-mode fiber equipped with a 3-paddles fiber polarization controller guides the light of the titanium-sapphire laser, operated in continuous wave (cw) mode, to the excitation arm of the microscope that is equipped with a shortpass filter. A beam sampler with anti-reflective coating transmits 90 % of the laser beam to a photodiode as reference for the laser power stabilization. The remaining 10 % are directed to the sample. A rotatable half-wave plate ($\lambda/2$) and an optional quarter-wave plate ($\lambda/4$) allow polarization control of the laser light. The sample is mounted beneath the apochromatic objective on a piezo-based xyz-positioning unit inside a sealed steel tube filled with helium gas for thermal coupling to the surrounding liquid helium (LHe) bath. The objective focuses the excitation laser on the sample and recollects the light. A small fraction of the collected light is reflected by a second beam sampler with anti-reflective coating and used for imaging with a CCD camera. The transmitted fraction passes a longpass filter before it is coupled into a single-mode fiber. The fiber is either connected to an alignment setup consisting of a fiber beam splitter with two photodiodes and a diode laser, or to the measurement systems: A grating spectrometer with a liquid nitrogen-cooled CCD camera or an avalanche photodiode (APD).

mode optical fiber and guided to the detection devices. The PL was either focused onto a single-photon counting avalanche photodiode (APD)[6] or dispersed by a grating monochromator[7] and imaged by a liquid nitrogen-cooled CCD.[8] The silicon-based photodetectors offered the advantage of low-noise characteristics. However, they are limited in spectral sensitivity due to a vanishing quantum efficiency in the near-infrared with a low-energy detection cut-off at ~1.18 eV (corresponding to an upper wavelength limit of 1050 nm). Using a grating with 300 grooves/mm in the monochromator, a spectral

[6] *Perkin Elmer* SPCM-AQRH-15
[7] *Princeton Instruments* Acton SP750i
[8] *Princeton Instruments* PyLoN:100BR, 1340x100 imaging array

resolution of ~220 µeV was achieved.

To maximize the collected signal, the microscope was aligned by plugging the optical fiber of the detection arm into the port of a fiber beam splitter, whose other ends were connected to a diode laser with a wavelength of 905 nm or 960 nm and two photodiodes. The diode laser was coupled into the microscope with a constant power that was monitored by the first photodiode. The laser beam passed the detection arm of the microscope, was reflected at the sample and was coupled back into the fiber beam splitter. The microscope was aligned by maximizing the power of the reflected beam that was measured by the second photodiode. This was achieved by adjusting the beam path along the detection arm towards the sample and by aligning the sample surface with the focal plane of the objective using the piezo-stepper in the z-direction.

3.2 Sample preparation and characterization

Photoluminescence spectroscopy was performed on two classes of CNT materials. Small-diameter nanotubes were grown directly on substrates by chemical vapor deposition (CVD), while chirality-sorted CNTs dispersed in solution were applied to a fused silica solid immersion lens (SIL) by drop-casting. Optical excitation of as-grown CNTs was usually performed in an energy range of 1.49 – 1.55 eV, where the energy difference between the laser excitation and the expected PL emission matched the energy of a G-band phonon. Due to a strong contribution of Raman photons to the PL signal at this energy for solution-processed CNTs (see Chapter 5), these CNTs were excited via the second exciton band denoted as E_{22}. For most CNTs the spatial extent of the cryogenic PL emission was smaller than the confocal spot size. As-grown CNTs were characterized by a resolution-limited spectral linewidth, whereas chirality-sorted CNTs from solution exhibited full-width at half-maximum (FWHM) spectral linewidths above 1 meV. All studied CNT materials and their key characteristics are listed in Table 3.1

Abbrevation	material	chirality	substrate	surfactant	filling
CVD_{susp}	as-grown	$[d]_m \leq 1$ nm	suspended	/	empty
CVD_{SiO_2}	as-grown	$[d]_m \leq 1$ nm	SiO_2	/	empty
CVD_{hBN}	as-grown	$[d]_m \leq 1$ nm	hBN	/	empty
DOC_{H_2O}	solution	(9,1)	SIL	DOC	H_2O
DOC_{org}	solution	(9,1)	SIL	DOC	$C_{20}H_{42}$
DNA_{org}	solution	(9,1)	SIL	DNA	$C_{24}H_{50}$
DOC*	solution	doped (6,5)	SIL	DOC	empty/H_2O

Table 3.1: Summary of all studied CNT materials. Row 2-4: The abbreviation CVD labels as-grown CNTs with the median of the diameter distribution $[d]_m \leq 1$ nm. The index denotes CNTs suspended over trenches, grown on silicon oxide (SiO_2), or hexagonal boron nitride (hBN). Row 5-8: CNTs applied to a solid immersion lens (SIL) by drop-casting are labeled according to the surfactants sodium deoxycholate (DOC) or DNA. The index refers to the filling with water or organic molecules. Alkyl-doped (6,5) CNTs are marked by an asterisk.

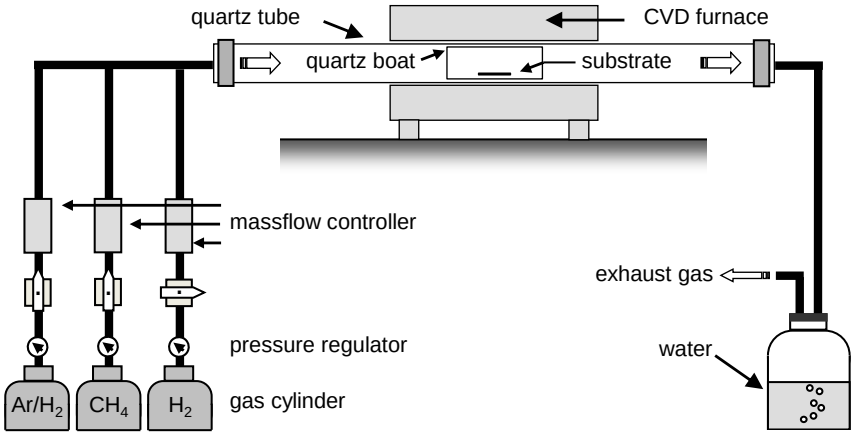

Figure 3.2: Chemical vapor deposition (CVD) setup. The growth substrate is positioned inside the furnace using the quartz boat. The quartz tube is purged with argon (Ar) mixed with hydrogen (5%) during the heating process. Methane (CH_4) acts as carbon source, while pure hydrogen (H_2) is used to remove amorphous carbon. All gas flows are regulated via massflow controllers. Exhaust gases pass a water bubbler to prevent ambient air from entering the quartz tube.

together with the corresponding abbreviations that will be used in the following.

3.2.1 As-grown carbon nanotubes

A major challenge in the fabrication of as-grown CNT samples is the lack of chirality control in the CVD process. In most experiments, nanotube PL is detected by silicon-based photodetectors that have a low-energy detection cut-off at 1.18 eV as mentioned in the previous section. Only few small-diameter CNT chiralities emit PL above this energy. Despite recent progress in chirality-deterministic CVD growth [73, 74], the most efficient way to obtain CNTs suitable for spectroscopy with silicon-based detectors is the optimization of the CVD-parameters to favor small-diameter CNTs.

Synthesis of CNTs by CVD is based on the decomposition of a carbon source (i.e. carbon monoxide or methane) by a metallic nanoparticle catalyst that absorbs the released carbon. When the carbon level in a catalyst particle saturates, excess carbon is precipitated in the form of a fullerene-like cap that grows to form a CNT. The CVD method used in this work to obtain CNTs with a diameter distribution with median $[d]_m \leq 1$ nm was based on methane and hydrogen in the presence of an iron-ruthenium (FeRu) catalyst. A detailed description of the growth process and of the CVD-parameters that control CNT density, diameter and length are given in Ref. [75] and [76], respectively.

The FeRu catalyst was prepared from three stock solutions consisting of iron(III) nitrate nonahydrate[9] ($Fe(NO_3)_3 \cdot 9H_2O$), ruthenium(III) chloride hydrate[10] ($RuCl_3 \cdot xH_2O$), and alumina (Al_2O_3) nanopowder[11] each dissolved in isopropyl alcohol with concen-

[9] *Sigma-Aldrich* 254223-10G
[10] *Sigma-Aldrich* 463779-10G
[11] *Sigma-Aldrich* 551643-10G

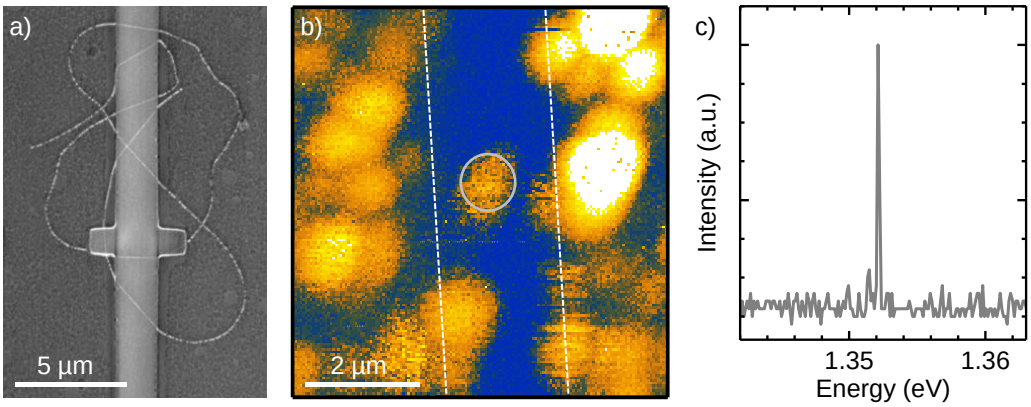

Figure 3.3: a) Scanning electron micrograph of CNTs grown by chemical vapor deposition on a SiO_2 substrate with etched trenches (light gray). b) Raster-scan of the cryogenic PL maxima acquired with circular polarized excitation with 12 W/mm^2. The trench edges are indicated by white dashed lines. The gray circle marks the PL emission from a suspended CNT. c) PL spectrum of the suspended CNT marked in (b) exhibiting a resolution-limited spectral linewidth of 177 µeV (full-width at half-maximum) for an integration time of 2 s.

trations of 4.65 g/l, 1.40 g/l, and 1.50 g/l, respectively. The solutions were stirred over night before small amounts were mixed together and diluted with isopropyl alcohol. The dilution controlled the concentration of catalyst particles in the solution and therefore the density of CNTs after CVD-growth. A catalyst solution containing 54 µl of each stock solution and 2 ml of isopropyl alcohol is defined to have a concentration of 1 : 1. To obtain a concentration of 1 : n, the volume of isopropyl alcohol is increased by the factor n.

Prior to CVD growth, the catalyst solution was bath-sonicated[12] for 2 hours before the FeRu catalyst particles were deposited by either spin-coating or drop-casting a droplet of the catalyst solution on the growth substrate. The substrate was then transferred to the home-built CVD reactor schematically depicted in Figure 3.2 and positioned at the center of the quartz tube in a quartz boat. The gases used during the growth process were methane (CH_4) as carbon source and hydrogen (H_2). An Ar/H_2 mixture (95% argon and 5% hydrogen) was used as inert gas to purge the quartz tube during heating and cooling of the CVD furnace[13] that supplied the thermal energy for the catalytic reaction. The pressure regulators of the gas cylinders were all set to a value of 3 bar and the gas flow rates were controlled by mass flow controllers.[14] The exhaust gases passed through a water bubbler to prevent ambient air from diffusing into the quartz tube.

To start the catalytic reaction the furnace was heated to the growth temperature of 850 °C under an Ar/H_2 flow rate of 1.5 standard liters per minute (slm). When this temperature was reached, the quartz tube was flushed with H_2 for five minutes at a flow rate of 1.0 slm to reduce the catalyst. Subsequently the CNT growth was started by feeding CH_4 and H_2 with flow rates of 1 slm and 0.75 slm, respectively, into the reactor.

[12] *Bandelin* Sonorex Digital DK 102 P
[13] *Nabertherm* R40/500/12-B170
[14] *Sevenstar* D07-19B and D08-2F

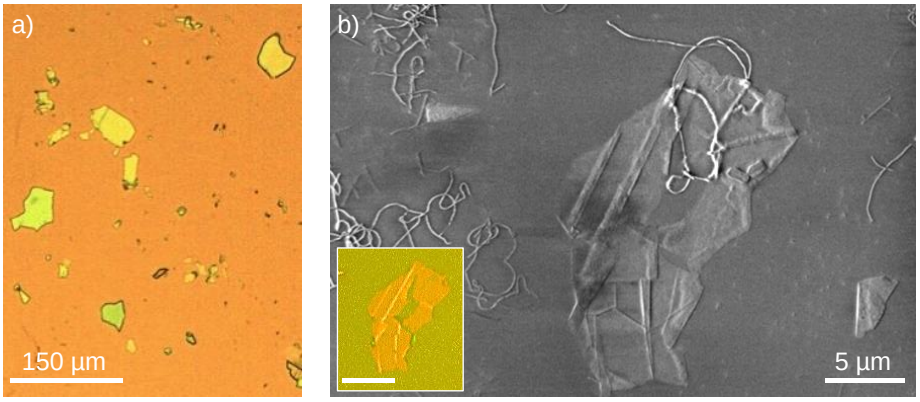

Figure 3.4: a) Optical image of exfoliated hBN flakes on a SiO_2. b) Scanning electron micrograph (SEM) of an hBN flake on SiO_2 with CNTs grown by chemical vapor deposition. As discussed in Ref. [77], carbon nanotubes appear to have a larger diameter on hBN as compared to SiO_2 in the SEM. The inset shows the optical image of the hBN flake, the scale bar is 10 µm.

These growth conditions were maintained for 10 minutes. Afterwards the CH_4 flow was stopped and the samples were cooled in a 0.5 slm hydrogen flow. At a temperature below 500 °C, hydrogen was replaced by the Ar/H_2 mixture at the same flow rate. When the furnace temperature had dropped below ~300 °C, the samples were unloaded from the furnace.

Suspended CNTs were grown on in-house fabricated structures made from p-doped silicon substrates (7 mm x 7 mm) with a 100 nm silicon oxide (SiO_2) layer on top. Trenches with a width of 0.8, 1.0, 1.5, and 2.0 µm were defined by electron beam lithography and etched to a depth of ~1 µm. The length and spacing of the trenches were 130 µm and 2 µm, respectively. Periodic markers with a width of 4 µm as shown in Figure 3.3a were used for orientation on the sample. To grow suspended CNTs by CVD, 10 µl of a 1:5 FeRu catalyst solution were applied to structured substrates by drop-casting and dried under a constant flow of nitrogen gas.

In the scanning electron micrograph (SEM) in Figure 3.3, a CNT crosses a 2 µm wide trench near a marker. The PL raster scan at 4.2 K in Figure 3.3b shows PL emission (gray circle) from a CNT suspended over a similar trench marked by white dashed lines. The spatial extension of the CNT PL was below the resolution of the confocal microscope (1.1 µm). The corresponding PL spectrum in Figure 3.3 had a FWHM spectral linewidth below 220 µeV which was the spectral resolution limit of the experiment. Narrow spectral linewidths were characteristic of suspended as-grown CNTs. The strong PL from the substrate in Figure 3.3b most likely stems from a network of CNTs.

Photoluminescence measurements of CNTs on hexagonal boron nitride (hBN) and SiO_2 were carried out on a sample that consisted of p-doped silicon with a 285 nm capping layer of thermal SiO_2 and exfoliated hBN flakes on top. Figure 3.4a shows an optical micrograph of the SiO_2 substrate (orange) with exfoliated hBN flakes (yellow). By coating the entire sample with FeRu catalyst particles, CNTs were grown on both

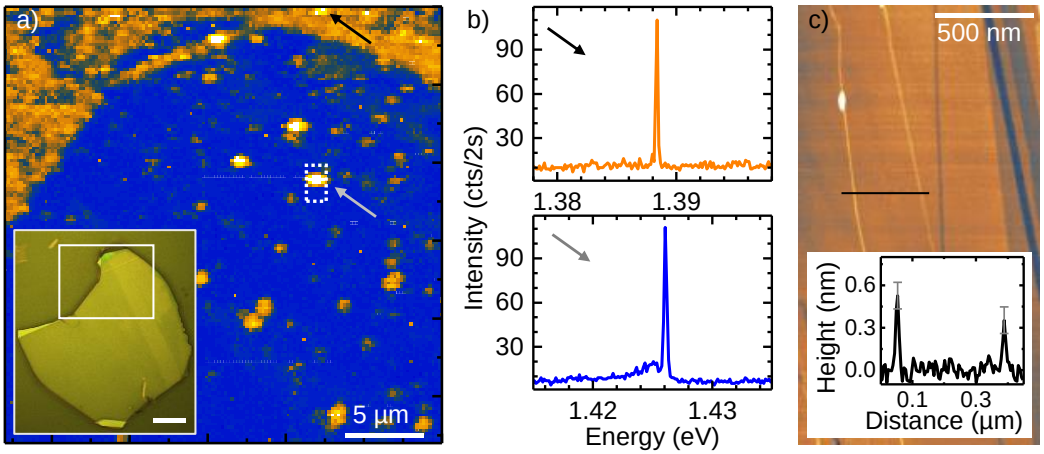

Figure 3.5: a) Cryogenic raster-scan PL map of a region with a ~ 300 nm thick hBN flake on SiO_2 indicated by the white rectangle in the optical image inset (different aspect ratios are due to non-linearities in low-temperature scanning). The contrast between the regions of SiO_2 (orange) and hBN (blue) stems from a much weaker PL background on hBN. b) PL spectra of the emitters marked by the arrows in (a). Orange and blue data corresponds to CNTs on SiO_2 and hBN, respectively. c) The atomic force micrograph of the area marked by the dashed white rectangle in (a) identifies two CNTs and hBN crystal terraces. Inset: Height profile of the nanotubes along the black line.

dielectric substrates as shown in the SEM image of a hBN flake in Figure 3.4b. The sample was prepared by the group of Prof. A. Bachtold,[15] using a similar procedure for CVD as described above. The details of the sample preparation are discussed in Ref. [42].

Figure 3.5a shows a map of PL peak intensities recorded with 26 W/mm^2 excitation power and circular polarization in the region of an hBN flake on SiO_2 indicated in the optical micrograph inset. The edge of the hBN flake in Figure 3.5a is identified by a cross-over from a dark-count limited background on hBN to a finite PL background on SiO_2. The logarithmic false-color scale of the PL map exaggerates the weak PL background on SiO_2 with respect to the one order of magnitude higher PL peak intensities of individual CNTs (15 – 130 cts/s). According to atomic force microscopy (AFM), the flake had a thickness of 300 nm. The PL hot spots in Figure 3.5a correspond to individual CNTs with spectrally narrow PL peaks characterized by resolution-limited FWHM linewidths at integration times of a few seconds for CNTs on SiO_2 and hBN as shown by the representative spectra in the upper and lower panel of Figure 3.5b, respectively. Consistent with PL emission in the spectral range of 1.24 – 1.46 eV, *a posteriori* AFM studies found CNTs with sub-nanometer diameters at the location of all PL hot spots. The representative AFM raster scan in Figure 3.5c (area marked by the white dashed lines in Figure 3.5a) shows two CNTs with diameters below 1 nm. The small white oval is attributed to a catalyst particle and the blue lines are ridges in the hBN crystal.

[15] *ICFO-Institute de Ciencies Fotoniques, The Barcelona Institute of Science and Technology*

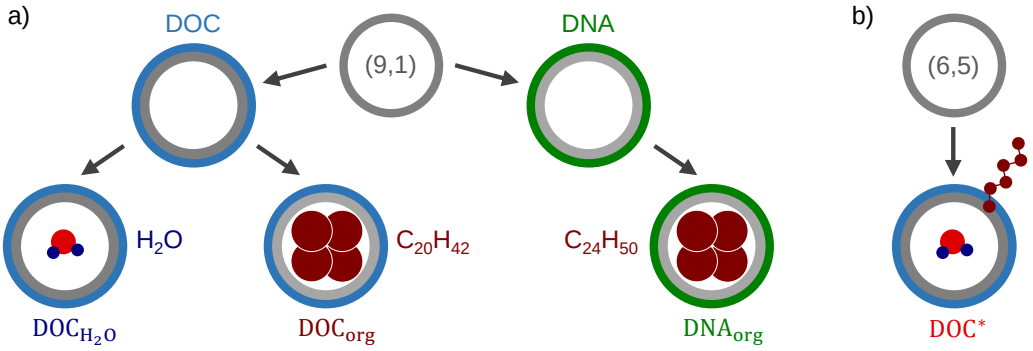

Figure 3.6: a) Illustration of the different combinations of CNT filling and surfactant of the studied (9,1) CNTs. Nanotubes (gray circles) coated with sodium deoxycholate (DOC, blue) were either filled with a single-file chain of H_2O molecules or by the alkane $C_{20}H_{42}$ that barely fits inside the CNT. The abbreviations of these CNT materials are DOC_{H_2O} and DOC_{org}, respectively. The CNTs abbreviated by DNA_{org} are DNA-wrapped (green) and filled with the alkane $C_{24}H_{50}$. b) (6,5) CNTs doped with the alkyl C_6H_{13} and DOC as surfactant.

3.2.2 Solution-processed and chirality-sorted carbon nanotubes

An alternative to as-grown CNTs are nanotubes in solution that can be deposited by drop- or spin-casting onto various substrates, be sorted by chirality [44], and offer the possibility to modify the optical properties by chemical functionalization [34, 35, 37, 39, 40, 45, 46]. To prevent the formation of CNT bundles in solution, nanotubes are coated with a surfactant material followed by ultrasonification.

Four different CNT materials dispersed in solution were studied in this work to analyze the effects of surfactant, CNT filling, and defects incorporated into the CNT lattice on the photophysical properties of a CNT. The schematic drawing in Figure 3.6 gives an overview of the different materials that are also listed in Table 3.1 (row 5-8). The (9,1) chirality-purified CNTs in Figure 3.6a were supplied by Dr. J. Fagan,[16] with the following combinations of surfactant materials and CNT fillings: DOC surfactant and and water-filling (DOC_{H_2O}), DOC surfactant and filling with alkane $C_{20}H_{42}$ molecules (DOC_{org}), and DNA surfactant with $C_{24}H_{50}$-filling (DNA_{org}).[17] DNA-wrapped CNTs were dispersed in pure water, whereas 1 wt%/V of DOC was added to solutions containing DOC-coated CNTs. More details regarding the preparation of the samples with DOC and DNA surfactant can be found in Ref. [78, 79] and [80], respectively. The (6,5) CNTs (DOC*) in Figure 3.6b were provided by the group of Prof. YuHuang Wang.[18] In addition to the different chirality, DOC* CNTs were not pristine but had C_6H_{13} molecules covalently bound to the CNT lattice as described in Ref. [38].

For cryogenic PL spectroscopy, all CNT materials were applied to a hemispheric fused silica solid immersion lens (SIL) with a diameter of 2 mm by drop-casting to increase the photon collection angle [81, 82]. Figure 3.7a shows a sketch of the sample

[16] *Materials Science and Engineering Division, National Institute of Standards and Technology*
[17] In this work the two alkanes $C_{20}H_{42}$ and $C_{24}H_{50}$ are assumed to have the same influence on the cryogenic PL of CNTs.
[18] *Department of Chemistry and Biochemistry and Maryland NanoCenter, University of Maryland*

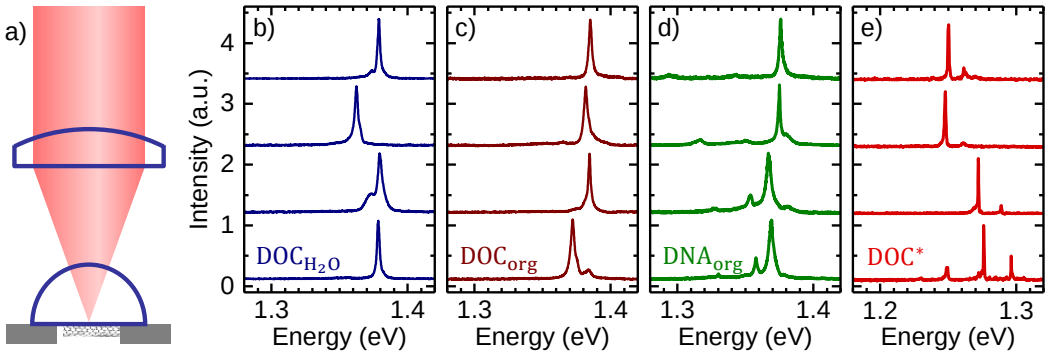

Figure 3.7: a) Schematics of the sample geometry used for confocal microscopy of solution-processed CNTs. Nanotubes were applied to the planar side of a hemispherical solid immersion lens (SIL). Optical excitation and detection were performed through the suspended SIL. b-e) Representative spectra of DOC_{H_2O}, DOC_{org}, DNA_{org}, and DOC* CNTs, respectively.

geometry used for PL spectroscopy of CNTs on a SIL. Following the studies in Ref. [83], a quartz glass (LASF35) with high refractive index $n = 2$ was chosen to maximize the number of photons emitted towards the objective for the sample geometry sketched in Figure 3.7a. The apex of the SIL faced the objective (blue), the planar side with the CNTs was suspended in the helium atmosphere to exploit the directive emission of a dipole into the medium with higher refractive index. The geometry of the SIL ensured that, independent of the excitation energy, the laser was focused onto the planar side of the SIL without refraction losses, as long as the beam passed the SIL near the apex resulting in a studied sample area of 100 µm times 100 µm.

Samples were prepared by diluting the CNT stock solutions with H_2O to tune the CNT density on the SIL to 1 CNT/µm^2. A droplet of the diluted solution was cast onto the flat side of the SIL. After drying, CNTs remained on the SIL together with DOC residuals in the case of DOC_{H_2O}, DOC_{org}, and DOC* CNTs. Table 3.2 summarizes the drop-casting procedure containing the amount of carbon per µl in the stock solution, the dilution factor and the volume cast onto the SIL for DOC_{H_2O}, DOC_{org}, DNA_{org}, and DOC* CNTs. To obtain the same CNT density, the dilution factor of DOC* CNTs had to be lower by a factor of 100 compared to DNA_{org} CNTs, even though the respective

Material	carbon content in solution [µg/ml]	dilution factor CNT solution/H_2O	droplet volume on SIL [µl]
DOC_{H_2O}	16	1/1000	1
DOC_{org}	10	1/1000	1
DNA_{org}	5-7	1/500	1
DOC*	0.55	1/5	1

Table 3.2: Summary of the drop-casting parameters of all solution-processed CNTs: carbon content of the stock solution, factor for the dilution with H_2O to modify the CNT density, and volume drop-cast onto the SIL (second, third and fourth column, respectively).

carbon concentrations only differ by a factor of 10. This may be due to CNTs with a larger average length in the DOC* solution resulting in a decreased density of CNTs for the same concentration of carbon atoms.

Figure 3.7b-e shows representative spectra of DOC_{H_2O}, DOC_{org}, DNA_{org}, and DOC^* CNTs at 4.2 K, respectively. The cryogenic PL spectra of pristine (9,1) CNTs are discussed in detail in Chapter 4. The (6,5) CNT PL was emitted at energies roughly 100 meV below the (9,1) CNTs as expected for this chirality. The PL peaks exhibited significantly smaller spectral linewidths compared to the undoped (9,1) CNTs with FWHM around and below 1 meV. The omnipresent side peaks are most likely related to defect states that were induced by the functionalization with the C_6H_{13} molecules.

Chapter 4

Influence of surfactant and filling on carbon nanotube photoluminescence

The effect of filling pristine carbon nanotubes with water or alkane molecules and the influence of nanotube encapsulation by sodium deoxycholate or DNA surfactants on the photoluminescence spectral line shape and energy were studied on chirality-sorted nanotubes that were applied to a solid immersion lens by drop-casting from aqueous solution. The spread in the cryogenic photoluminescence energies was related to surfactant-induced strain and to the occurrence of low-energy defect states for nanotubes with sodium deoxycholate and DNA surfactants, respectively. Neither the photoluminescence spectral lineshape nor the spectral dynamics were found to be strongly influenced by the surfactant agents or by encapsulation of water or alkane molecules inside the nanotube. The results are complemented by a comparison to room temperature absorption measurements of nanotubes dispersed in solution that are connect to the cryogenic data by taking into account modifications of the dielectric environment, strain, and a phase transitions of water molecules confined inside a nanotube upon cool-down.

4.1 Introduction

A pivotal requirement for future applications of carbon nanotubes (CNT), is the ability to control and tailor their photophysical properties. Substantial progress has been achieved towards this goal by establishing processes to sort CNTs by chirality with fidelities exceeding 99% [44] and to modify their optical properties via the incorporation of specific defects into the CNT lattice by covalent side-wall chemistry either with oxygen [34, 35, 39, 45] or diazonium [37, 38, 40, 46]. However, both techniques require CNTs dispersed in aqueous solutions, that are prepared by coating CNTs with a surfactant followed by ultrasonification to prevent bundling. Due to the large aspect ratio of nanotubes, excitons are not shielded from the CNT environment other than e.g. nitrogen-vacancy centers in diamond. This renders excitons, and consequently the CNT photoluminescence (PL), especially sensitive to the dielectric environment [42], which is altered by the surfactant and by molecules that can enter CNTs where the carbon endcaps were opened by ultrasonification [84]. So far, studies on the PL characteristics of CNT filled with H_2O and organic molecules exist only at room temperature [79, 84], whereas at cryogenic temperatures only empty and water-filled CNTs were compared [85]. However, in particular at low temperatures where unintentional exciton localization dominates the CNT PL [33], the effects of surfactants and fillings have to be understood in order to interpret cryogenic PL emission.

This chapter presents a systematic comparison of the low-temperature PL characteristics of CNTs with different fillings and surfactants. Water and the organic molecules $C_{20}H_{42}$ and $C_{24}H_{50}$ were chosen as filling materials and combined with two common CNT surfactants sodium deoxycholate (DOC) and DNA.

4.2 Experimental methods

Samples were prepared by drop casting a chirality-purified solution of (9,1) CNTs onto a solid immersion lens (SIL). Each solution contained CNTs with a specific combination of surfactant and filling material, as listed in Table 4.1 (see Section 3.2.2 for more details). All PL data shown in this chapter was obtained at 4.2 K by continuous wave (cw) excitation with a titanium-sapphire laser ($1-30\,\mathrm{W/mm^2}$) resonant with the second exciton band denoted as E_{22} in the following.

Abbrevation	chirality	substrate	surfactant	filling
DOC_{H_2O}	(9,1)	SIL	DOC	H_2O
DOC_{org}	(9,1)	SIL	DOC	$C_{20}H_{42}$
DNA_{org}	(9,1)	SIL	DNA	$C_{24}H_{50}$

Table 4.1: List of the CNT materials studied in this chapter. All CNTs were dispersed in solution and drop-cast onto a solid immersion lens (SIL). They are labeled according to their surfactant (DOC is the abbreviation for sodium deoxycholate). The index refers to the filling with water or organic molecules.

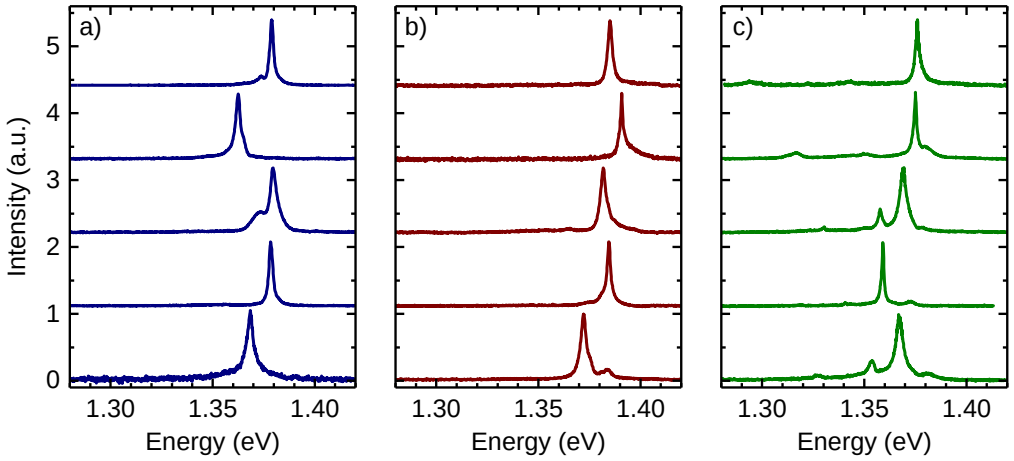

Figure 4.1: Representative spectra of individual DOC_{H_2O}, DOC_{org}, and DNA_{org} CNTs at 4.2 K with 10 s integration time (a, b, and c, respectively). Note that the PL was not corrected for spectral diffusion.

Figure 4.1 shows representative PL spectra of individual CNTs from each sample with 10 s integration time. All spectra are characterized by one dominant PL peak which is often accompanied by weaker PL emission at lower and higher energies. Blue, brown, and olive data correspond to DOC_{H_2O}, DOC_{org}, and DNA_{org} CNTs, respectively.

PL spectra with a signal-to-noise ratio S/N> 1000 without the detrimental effects caused by spectral diffusion, such as PL spectral line broadening or line shape deformation at long integration times in the presence of spectral wandering (see Section 6.3), were obtained by post-processing time series of PL spectra. Each time series consisted of multiple PL spectra with 1 s integration time per spectrum[1] Subsequently a spectrum with high S/N and minimum spectral diffusion was constructed by shifting each spectrum of the time series to have a maximum overlap with the previous and finally summing up all shifted spectra. If not stated otherwise, all data presented in the following was obtained by this process.

4.3 Photoluminescence spectral line shape

Figure 4.2a-c compare the PL full-width at half-maximum (FWHM) spectral linewidth as a function of the laser excitation power for DOC_{H_2O}, DOC_{org}, and DNA_{org} CNTs, respectively. The data points connected by solid lines belong to the same CNT. Due to PL bleaching, only a few DNA_{org} CNTs were measured at more than one excitation power. The PL FWHM linewidth had the same order of magnitude for all CNTs and DOC_{H_2O} and DNA_{org} CNTs showed a slight increase of the FWHM linewidth with higher excitation powers.

Figure 4.3a-c show the summed spectra of a time series of the main PL peak from a

[1] This was the minimum integration time required for a signal-to-noise ratio S/N> 1 at low excitation powers of about 0.8 W/mm^2.

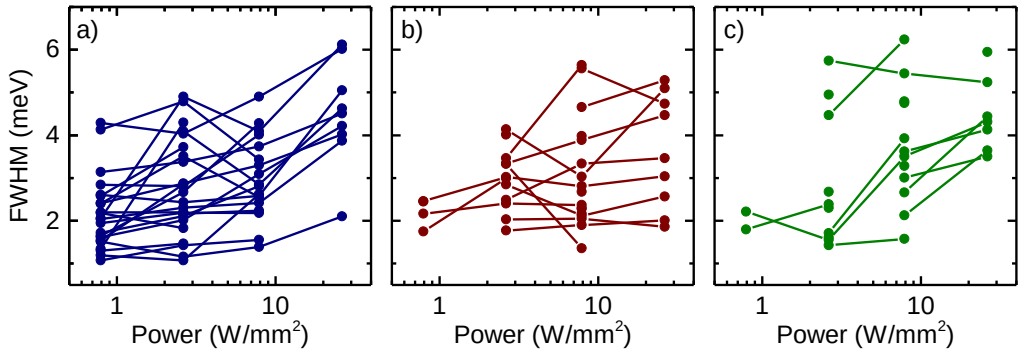

Figure 4.2: Full-width at half-maximum spectral linewidth of DOC_{H_2O}, DOC_{org}, and DNA_{org} CNT PL as a function of the excitation power (a, b, and c, respectively). Data points connected by solid lines belong to the same CNT.

DOC_{H_2O}, a DOC_{org}, and a DNA_{org} CNT, respectively. The number of spectra per time series ranged from 300 to 1000 with 1 s integration time per spectrum and an excitation power of 3 W/mm^2 to obtain a signal to noise ratio S/N> 1000 for all CNTs. The spectra that were corrected for spectral diffusion as described in Section 4.2 are shown in blue, brown, and olive, whereas the unprocessed spectra are depicted in magenta, orange and turquoise. For CNTs wrapped in DOC, the spectral diffusion, i.e. the difference between the original and the post-processed data, is small compared to the FWHM (Figure 4.3a-b). In contrast, the elimination of spectral diffusion from the PL of the CNT wrapped in DNA led to a decrease of the FWHM linewidth of about 40 %. This suggests an increased susceptibility of DNA-coated CNTs to environmental influences which is also discussed in Section 5.3.2. Independent of filling or surfactant material, all CNTs exhibited rather symmetric PL spectral line shapes in contrast to previous cryogenic PL studies, where an asymmetric spectral line shape was found for CNT PL governed by unintentional exciton localization [25, 26, 28] and for defect-functionalized nanotubes [35, 39, 46]. This asymmetry was reproduced with high accuracy using a

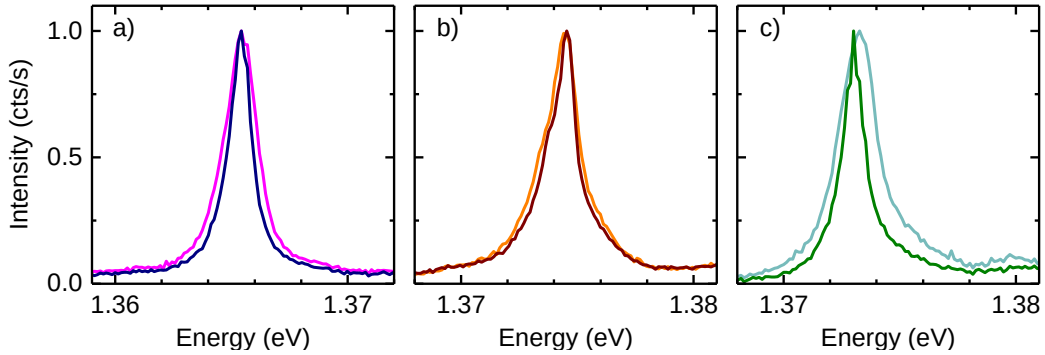

Figure 4.3: Spectra of CNTs from DOC_{H_2O} (a), DOC_{org} (b) and DNA_{org} (c) CNTs. The spectra were obtained as the sum of a series with 300, 300, and 1000 s spectra (magenta, orange, and turquoise data, respectively). Blue, brown, and olive data are spectra corrected for spectral diffusion.

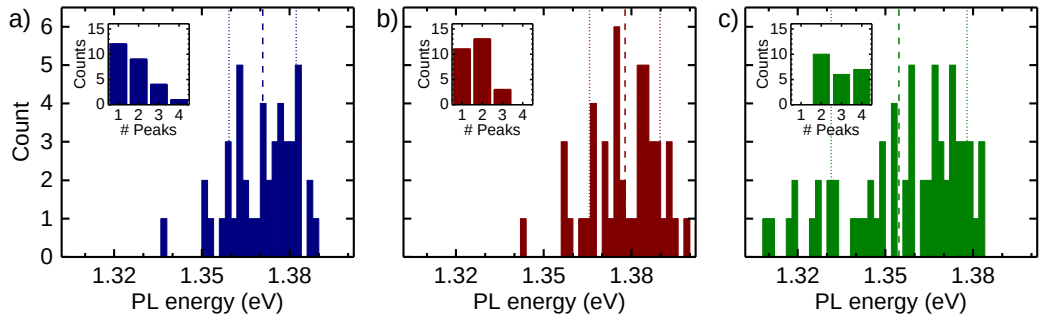

Figure 4.4: Histogram of emission energies of all PL peaks observed for DOC_{H_2O}, DOC_{org}, and DNA_{org} CNTs (a, b, and c, respectively). Dashed and dotted lines indicate the mean PL energy and the corresponding standard deviation, respectively. Insets show histograms of the number of PL emission peaks per CNT.

model which is based on the coupling of a localized exciton [28] to a continuous or gapped 1D acoustic phonon bath as discussed in Ref. [86] and [87], respectively. The data obtained by PL excitation spectroscopy in Section 5.3, however, suggests that the low-temperature PL of DOC_{H_2O}, DOC_{org}, and DNA_{org} CNTs stems from delocalized excitons, which would also explain the absence of asymmetric PL spectral lineshapes.

4.4 Photoluminescence energies

The cryogenic PL of DOC_{H_2O}, DOC_{org}, and DNA_{org} CNTs is characterized by one dominant PL peak that is often accompanied by red- and/or blue-shifted satellite peaks as shown in Figure 4.1. Energy histograms of all resolved PL peaks are depicted in Figure 4.4a, b, and c for DOC_{H_2O}, DOC_{org}, and DNA_{org} CNTs, respectively. Carbon nanotubes coated with DOC in Figure 4.4a and b both show symmetric distributions of PL energies over a range of ~50 meV. The mean of the distribution as well as its high-energy onset is shifted to higher energies by about 10 meV for DOC_{org} CNTs. This value is still within the standard deviation indicated by the dotted lines. Over 80 % of DOC_{H_2O} and DOC_{org} CNTs show single or double peak PL emission (insets in Figure 4.4a and b). In contrast, single-peak emission is absent for DNA-coated CNTs and the corresponding PL energy histogram in Figure 4.4c is characterized by an asymmetric energy distribution with a low-energy tail covering an energy range of over 70 meV. The corresponding standard deviation is more than twice as large as that of CNTs coated with DOC.

The data shown in Figure 4.4 suggests that both, filling and surfactant, have an influence on the low-temperature PL emission energies of CNTs. A further analysis is hindered by the broad distribution of PL peak energies that results in a standard deviation one order of magnitude larger than the PL FWHM. This spread in emission energies is typical for cryogenic CNTs and can be related to various phenomena such as an inhomogeneous dielectric environment, strain, the presence of nearby charges and defects in the CNT. These effects vary from tube to tube. In consequence, a distribution of PL energies and multipeak spectra are observed even for chirality-purified CNTs. To

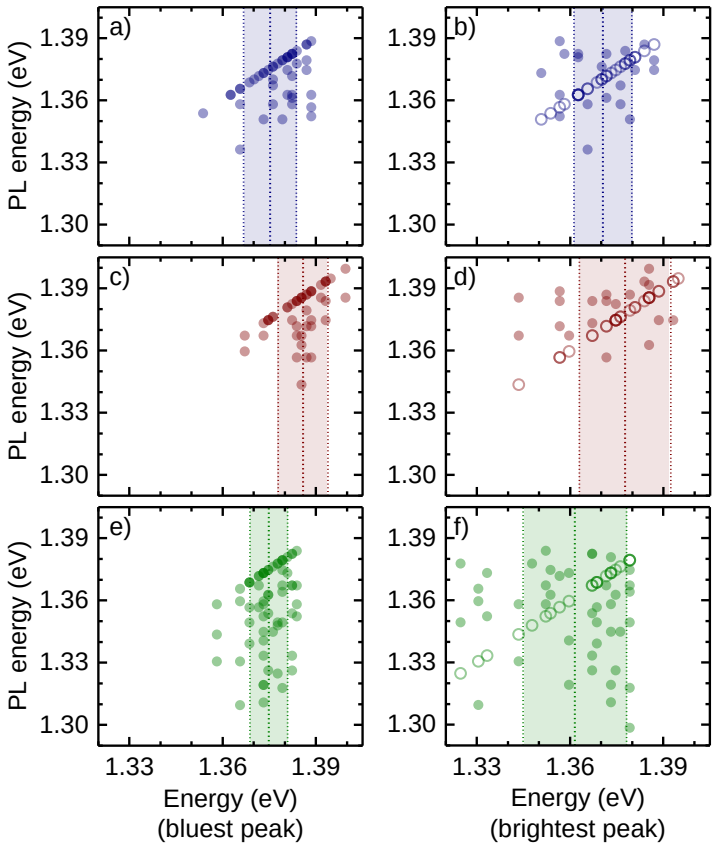

Figure 4.5: PL peak energies of all PL spectra as a function of the bluest and brightest PL peak in the respective spectrum (left and right panels, respectively). Empty circles indicate the brightest PL peaks for better distinguishability in the right panels. Blue, brown and olive data correspond to DOC_{H_2O}, DOC_{org} and DNA_{org} CNTs, respectively. The colored dotted lines mark the average energy of the bluest (a,c,e) and the brightest PL peaks (b,d,f), the standard deviations are indicated by the colored areas. The data points are semi-transparent to better identify overlapping data.

reduce the complexity of mulitpeak PL spectra, the following analysis concentrates on two classes of PL peaks. For each CNT the peak with the highest intensity and the peak with the highest energy were selected. They are denoted as P_i and P_e in the following.

Figure 4.5 shows the energy of every PL peak of the studied CNTs as a function of the CNT-specific energies for P_e and P_i (left and right panels, respectively). The vertical dotted lines and the colored areas mark the average energy and standard deviation of P_e and P_i , respectively.

For DOC_{H_2O} CNTs, the energies of P_e and P_i are both distributed over a range of Δ_E = 40 meV and have similar average values and standard deviations. There is no tendency for red or blue peaks to be brighter, i.e. a similar number of side peaks is found below and above the diagonal line that identifies the brightest peaks in Figure 4.5b. As shown by comparing Figure 4.5a and c, DOC_{org} CNTs are similar to their water-filled counterparts with respect to the distribution of PL energies as a function of the P_e energies except for the global shift in the PL average energy that was already observed in Figure 4.4.

The comparison of Figure 4.5b and d, on the other hand, shows a discrepancy between DOC_{H_2O} and DOC_{org} CNTs. In contrast to DOC_{H_2O} CNTs, the highest-intensity PL of DOC_{org} CNTs in Figure 4.5d is predominantly found at the lowest energy. In addition, all PL data outside the energy range marked by the standard deviation lies below the mean value and the standard deviation itself is significantly larger compared to Figure 4.5a-c. These phenomena are even more pronounced for the corresponding data from the DNA_{org} CNTs shown in Figure 4.5f, whereas the P_e data of the DNA-wrapped CNTs shown in Figure 4.5e exhibit a small standard deviation comparable to Figure 4.5a and c. The satellite peaks of DNA_{org} nanotubes were red-shifted by up to 70 meV exceeding the energy range expected for unintentional exciton localization [33].

4.4.1 Variations in the energy of characteristic photoluminescence peaks

Since all CNT samples were prepared in the same way, the observed differences among DOC_{H_2O}, DOC_{org}, and DNA_{org} CNTs have to arise from the different filling and surfactant materials. However, the disorder-induced spread in the PL data in Figure 4.5 and the resulting large statistical deviations from the average values makes a comparison of the PL energies very challenging. Furthermore, the individual effects of the dielectric environment, strain, charges or unintentional defect-localization are difficult to discriminate, since they all shift the PL energy on the same energy scale of several tens of meV. To better understand the PL data, the P_e and P_i energies were complemented by the respective energy of the second exciton band E_{22} that was extracted for every CNT from PLE measurements.

The presence of defect states, strain or changes in dielectric environment all shift the PL energy and E_{22} in specific ways that are listed in Table 4.2 and can be summarized as follows:

- Defect states emit PL red-shifted compared to E_{11}, but inherit the excitation resonance, i.e. E_{22}, of the pristine CNT
- Strain shifts E_{11} and E_{22} in opposite directions
- A decreasing dielectric constant shifts both E_{11} and E_{22} to higher energies

The characteristics of defect states are discussed in more detail in Section 5.4. Most of the previous work on the effect of strain and dielectric environment on CNT PL energies is not directly applicable to the experimental settings of this study regarding chirality, CNT diameter, temperature and environmental dielectric constant. However, by a combination of experimental data and theoretical models from previous studies it is possible to extract scaling behaviors and energy scales that are often sufficient to connect the observed data to specific environmental effects. To this end, theoretical and experimental results regarding the influence of strain and dielectric environment on CNT energy levels are discussed in the following.

Excitonic transition	E_{11}	E_{22}
Uniaxial extension [88–90]	53 meV/ % strain	53 meV/ % strain
Uniaxial compression [88–90]	53 meV/ % strain	53 meV/ % strain
Radial expansion [79, 88–90]	53 meV/ % strain	53 meV/ % strain
Radial compression [79, 88–90]	53 meV/ % strain	53 meV/ % strain
decreasing ε_r	$\lvert\Delta E_{11}\rvert < 50$ meV	$\lvert\Delta E_{22}\rvert \leq \lvert\Delta E_{11}\rvert$
increasing ε_r	$\lvert\Delta E_{11}\rvert < 50$ meV	$\lvert\Delta E_{22}\rvert \leq \lvert\Delta E_{11}\rvert$
Unintentional exciton localization [33]	< 60 meV	

Table 4.2: Summary of the energy shifts caused by strain, dielectric environment and exciton localization. Shifts to higher and lower energies are indicated by blue and red, respectively. The upper limit for energy shifts due to changes in the dielectric environment ε_r was set to the energy shifts between CNTs in air and aqueous solution [91].

A theoretical model that was developed in Ref. [88] and later refined in Ref. [89], calculates the effect of strain ϵ_s on the k-th energy level E_{kk} of a CNT as

$$\frac{\Delta E_{kk}}{\epsilon_s} = \frac{12\alpha}{2(1+6\alpha)} \mathrm{sgn}(2p+1)(-1)^{k+1}(1+\nu)3t_0\cos(3\theta) \ , \tag{4.1}$$

with $p = -1$ for the $(n-m)\mathrm{mod}3 = 2$ CNT family such as the studied (9,1) chirality. The factor $(-1)^{k+1}$ in Equation 4.1 shows that E_{11} and E_{22} transitions are shifted in opposite directions for uniaxial strain, i.e. E_{11} as a function of E_{22} shifts along a line with slope -1 as indicated by the dashed lines in Figure 4.6a and b. Due to their small chiral angle θ, (9,1) CNTs are very suscetpible to strain. Using $t_0 = 2.7$ eV for the carbon-carbon hopping integral, $\nu = 0.2$ for the Poisson ratio and $\alpha = 0.066$ [89], Equation 4.1 yields an energy shift of $|\Delta E_{kk}|/\epsilon_s = 53$ meV/%.

The dielectric environment effects the exciton energy via a modified screening of the Coulomb interaction between electrons and holes. According to Ref. [60], the binding energy of a CNT exciton surrounded by a medium with dielectric constant ε_r scales with $\varepsilon_r^{-1.4}$. Following this approach for the E_{11} transition of a (9,1) CNT in water (E_{11} = 1.354 eV and ϵ_r~2), a decrease of ε_r by 1% would lead to a blue-shift of E_{11} by almost 20 meV. Performing the same calculations using a model proposed in Ref. [92], predicts an energy shift that is more than 2 orders of magnitude smaller. This discrepancy may be due to the fact that both models focus on relative dielectric constants $\varepsilon_r > 3$, whereas studies in this chapter were performed in a regime $\varepsilon_r < 2.5$. In addition, the model proposed in Ref. [92] does not consider CNTs with diameters as small as 0.7 nm for (9,1) CNTs. Also none of the models includes the E_{22} transition. However, experiments on various CNT chiralities down to diameters of 0.8 nm comparing energy levels in

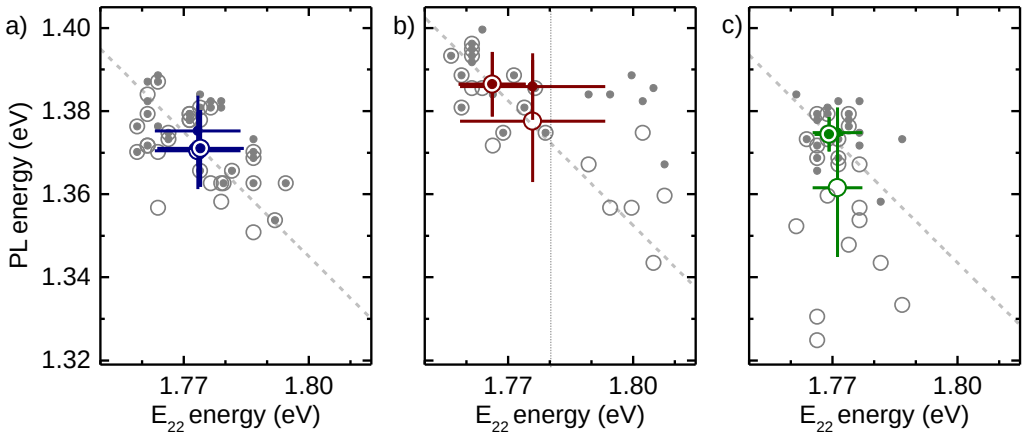

Figure 4.6: Energy of cryogenic PL peaks as a function of the corresponding E_{22} energy of DOC_{H_2O}, DOC_{org}, and DNA_{org} CNTs (a, b, and c, respectively). Gray empty circles indicate the brightest PL peaks and gray full circles the bluest PL peaks. CNTs for which the bluest PL peak was also the brightest are shown as an overlap of these symbols. The colored symbols represent the corresponding averages including the respective standard deviations. Diagonal gray dashed lines have the slope of −1 as expected for variations in strain and were shifted to pass through the average of the PL peaks that simultaneously had the highest energy and intensity.

solution (ε_r~2) to CNTs in air ($\varepsilon_r = 1$) found energy blue-shifts of ~25 meV and ~50 meV for E_{22} and E_{11}, respectively, for small-diameter CNTs. The energy shifts of E_{11} were consistently larger compared to E_{22}, especially for sub-nanometer diameter CNTs [91]. Similar energy scales were reported in Ref. [93]. These values will be considered as an upper limit for the energy shifts observed in the experiments presented in this chapter.

Figure 4.6 shows the energies of P_e and P_i from Figure 4.5 as a function of the respective E_{22} energy as full and empty gray circles, respectively.[2] Carbon nanotubes for which the bluest PL peak was also the brightest are marked by an overlap of those symbols and will be denoted simply as P in the following. The average values are indicated by the specific enlarged and colored symbols including the corresponding standard deviations.

All PL peaks in Figure 4.6a are scattered along a line with a slope of −1, suggesting that a difference in the strain of individual nanotubes is the major cause for the spread in the cryogenic PL energies of DOC_{H_2O} CNTs. According to Table 4.2, the observed energy spread of ~40 meV corresponds to variations in strain of about 0.75%. This can not solely be attributed to thermal expansions of the CNT and the substrate which both have a very small thermal expansion coefficient in this temperature range [94, 95]. The same scaling is observed for DOC_{org} CNTs in Figure 4.6b (at least for E_{22} energies below 1.78 eV), but it is absent for DNA-wrapped CNTs in Figure 4.6c, which implies that the observed strain effect is related to the DOC surfactant. Previous ensemble measurements of

[2] For all PLE measurements that included multiple PL peaks, all peaks exhibited the same E_{22} resonance (see Figure 5.7). However, this was not validated for all CNTs. For all other CNTs, the same value of E_{22} was assumed for the P_e and the P_i peak, even if it was only measured for P_i .

CNTs applied to a quartz substrate from an aqueous dispersion with 1 wt%/V DOC by drop-casting reported energy shifts associated with a net strain of 1.32 % during cool-down from room temperature to 4.2 K [85] showing that such strain levels can occur for cryogenic DOC-coated CNTs. The nanotubes in that study were surrounded by the surfactant attached to the CNT and embedded in a matrix of dried DOC residues. Deformations of the surfactant matrix during cool-down may have caused the observed CNT strain. Similar effects have also been reported for polymer-wrapped CNTs [96]. The DOC concentration in the aqueous (9,1) CNT solutions studied in this chapter was three orders of magnitude lower as compared to Ref. [85]. However, small DOC residues in addition to the DOC on the CNTs are still likely to remain. The tube-to-tube variations in strain that lead to the energy spread observed in Figure 4.6a may therefore be caused by a varying coverage with DOC that strains CNTs upon cool-down.

The spread of the PL data orthogonal to the gray dashed line in Figure 4.6a is most likely caused by small variations in the dielectric environment. In contrast to DOC-coated CNTs, the PL peak distribution of the DNA-wrapped nanotubes in Figure 4.6c does not follow the dashed line with the slope of -1. This is consistent with the hypothesis that a matrix of dried surfactant strains the cryogenic CNTs, since DNA_{org} CNTs are dispersed in pure water and only small amounts of excess DNA remain on the substrate after drop-casting. Of course cryogenic DNA_{org} CNTs may also be strained, but if they are, it affects all CNTs equally.

The P_i and P_e PL peaks of DOC_{H_2O} CNTs both show a relation between PL and E_{22} energy that is typical for E_{11} and E_{22} under strain and their average values are identical within the statistical error. This is a strong indicator that both PL peak types are closely related to the E_{11} transition and no other exciton states are involved. A similar behavior was observed for the PL peaks of DOC_{org} CNTs in Figure 4.6b for E_{22} energies below 1.78 eV (indicated by the vertical dotted line). All P PL peaks fall within this energy range. In contrast to DOC_{H_2O} CNTs, however, the average energies of P_i and P_e exhibit large standard deviations and are significantly shifted from each other. This shift is caused by the class of CNTs with E_{22} energies above 1.79 eV. For most of these CNTs, the energy of P_i follows the scaling expected for increasing uniaxial strain. The associated P_e energies, however, do not scale with E_{22} which leads to an increasing energy gap between P_e and P_i . A possible explanation of this phenomenon is “slipping” of CNT segments due to the significant strain that is associated with the large E_{22} values. Studies on CNTs in strained polymer films observed a similar behavior for CNTs that were strained above a threshold value [90]. If a part of the CNT smaller than the confocal spot size slips free from the straining matrix while the rest stays strained, the PL signature would be that observed in Figure 4.6b. Of course the PL stemming from these CNT segments will also different E_{22} energies. This could not be verified, since only the E_{22} resonances of the brightest PL peaks were determined. On the other hand, according to the brightness of the PL peaks that follow the dashed line in Figure 4.6b, the CNT segment that is not strained is small compared to the strained part and therefore the E_{22} resonance related to the relaxed CNT would probably be to weak to observe.

In contrast to DOC-coated CNTs, the DNA_{org} nanotubes in Figure 4.6c do not show a scaling of the PL energy consistent with strain. All P_e data are evenly distributed around their average value, where especially the class of P peaks shows remarkably small scatter. The P_i data, on the other hand, is spread over a wide range of emission energies indicative of PL emission from defect states that was not observed for DOC-coated CNTs. This result is also consistent with the data shown in Figure 4.5. The occurrence of defect states in DNA_{org} CNTs can either be caused by interaction with the DNA or be a consequence of a less effective screening from environmental influences.

4.4.2 Comparison of cryogenic and room temperature optical transition energies

Figure 4.7 compares the cryogenic PL (circles) and room temperature E_{11} (diamonds) energies of the studied (9,1) CNT materials as a function of E_{22} . The cryogenic PL does not necessarily stem from the unperturbed E_{11} transition of a CNT but may be modified due to exciton localization by disorder as for example the P_i PL peaks in Figure 4.6c. For the latter, the PL energy does not scale with E_{22} as expected for the E_{11} transition. The only subset of PL peaks that does not deviate from the behavior expected for E_{11} for all CNT materials is the P data which was therefore chosen as low-temperature reference value for a comparison with E_{11} at room temperature. The cryogenic E_{22} resonances were measured by PLE and the room temperature values for E_{11} and E_{22} were taken from absorption measurements on CNTs dispersed in aqueous solution. In the following, the values for E_{11} and E_{22} at room temperature will be connected to cryogenic measurements in the framework of energy shifts caused by strain and by changes in the dielectric environment as discussed in the previous section and as summarized in Table 4.2.

The room temperature values indicated in Figure 4.7a by blue, brown, and olive diamonds for DOC_{H_2O}, DOC_{org}, and DNA_{org} CNTs, respectively, are shifted significantly from each other. The shifts of E_{11} and E_{22} between DOC_{H_2O} and DOC_{org} CNTs are caused by radial strain indicated by the dotted green arrow with a slope of -1. The strain is induced by the $C_{20}H_{42}$ molecules that barely fit into the small-diameter (9,1) nanotubes [79]. The energy shift between DOC_{org} and DNA_{org} CNTs at 300 K can only be explained by a combination of strain and a different dielectric environment (green and yellow dashed arrows, respectively).

Even though E_{11} and E_{22} of all CNT materials are blue-shifted at 4.2 K (filled circles including the standard deviation as error bars), the magnitude and direction of these shifts depends strongly on the CNT material. Band gap changes upon cool-down predict a blue-shift of the optical transitions of a (9,1) CNT by 6.2 meV [97] that is indicated by the diagonal red-to-blue solid arrows in Figure 4.7b and c. The remaining energy differences of E_{11} and E_{22} between room temperature and 4.2 K are in accord with energy shifts expected for a decreasing dielectric constant of the CNT environment, most likely caused by the drop-casting and the drying of the aqueous CNT solution. The

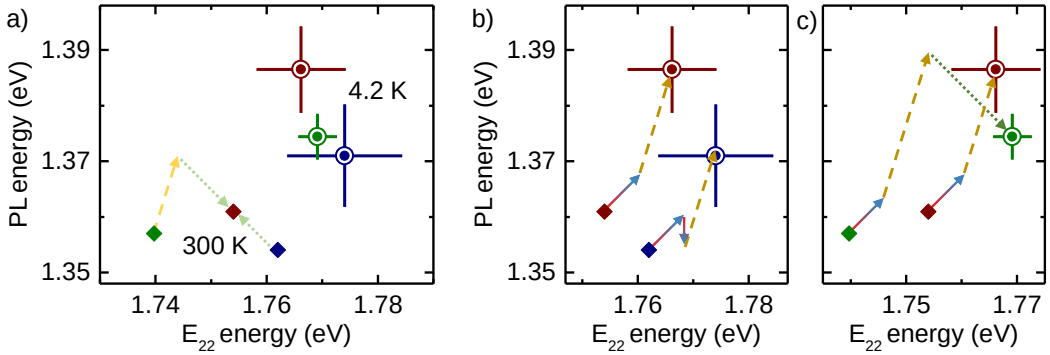

Figure 4.7: a) Average values of cryogenic PL data as a function of E_{22} from Figure 4.6 (concentric circles) compared to the corresponding room temperature values of E_{11} and E_{22} of CNTs dispersed in solution (diamonds). Blue, brown, and olive data correspond to DOC_{H_2O}, DOC_{org}, and DNA_{org} CNTs, respectively. b) and c) Zoom in for CNTs with the same surfactant and the same filling, respectively. Energy shifts among DOC_{H_2O}, DOC_{org}, and DNA_{org} CNT materials at 300 K (a) and among the same materials upon cool-down (b and c) are decomposed into contributions related to changes in the dielectric environment, strain, and cool-down (dashed yellow, dotted green, and solid red-to-blue arrows, respectively).

dielectric constant-induced shift required to connect room temperature and cryogenic data of DOC_{org} CNTs is indicated by the dashed orange arrow in Figure 4.7b and c and is still below the upper bound set in Table 4.2.

In the case of cryogenic DOC_{H_2O} CNTs, an additional red-shift of E_{11} during cool-down is expected, caused by a realignment of the H_2O dipoles inside the CNT. This transition was observed in water-filled (6,5) CNTs [85]. The dipoles of the single-file water molecules in these small-diameter CNTs aligned during cool-down and caused a red-shift of E_{11} by about 5 meV (note that the low-temperature phase does still not occupy enough volume to strain the CNT). The same shift is assumed for the small-diameter (9,1) DOC_{H_2O} CNTs as indicated by the vertical red-to-blue arrow in Figure 4.7b. The remaining energy difference between room temperature and low-temperature values is equal to the dielectric shift found for DOC_{org} CNTs (dashed orange arrow) as expected, since CNTs with the same surfactant should exhibit the same changes in their dielectric environment upon drop-casting.

A comparison of the cryogenic and room temperature data of DOC_{org} and DNA_{org} CNTs is more complex. In the framework used so far, the differences between these CNT materials at room temperature (Figure 4.7a) and the connection to low-temperature measurements (Figure 4.7c) can only be explained by a changed dielectric environment combined with a uniform strain acting on all DNA-wrapped CNTs (dashed orange and dotted green arrows in Figure 4.7a and c, respectively). Since the relative scaling of E_{11} and E_{22} with the dielectric constant should only depend on the CNT chirality, the slope of the orange dashed arrows in Figure 4.7c was set to the value obtained for DOC_{org} and DOC_{H_2O} CNTs in Figure 4.7b. With this assumption, a blue-shift of E_{11} by ~28 meV due to a decreased dielectric constant combined with a strain-induced red-shift of E_{11} by about 15 meV (green dotted arrow) reproduces the energy shifts of E_{11} and

E_{22} for DNA_{org} CNTs upon cool-down. The dielectric shift is a couple of meV larger than for DOC-coated CNTs, which can be attributed to the different dielectric properties of DNA compared to DOC. Since the DNA is wrapped around the CNTs in a periodic and well-defined way, it has the potential to uniformly strain all DNA_{org} CNTs. However, not enough experimental data or theoretical models exist regarding the behavior of DNA upon drying and cool-down to validate this hypothesis.

4.5 Conclusion

In this chapter the influence of surfactant-coating and filling of CNTs on their cryogenic PL characteristics was studied on the chirality-sorted (9,1) CNTs listed in Table 4.1. The PL of most CNTs was characterized by one dominant peak with FWHM between 1 – 4 meV and symmetric spectral line shapes for all CNT materials. The PL maximum was often accompanied by red- or blue-shifted satellite peaks, with an increased occurrence of multipeak emission for DNA_{org} CNTs. The distribution of the low-temperature PL emission energies showed differences depending on the CNT filling and surfactant. Whereas the PL energies of DOC-coated CNTs were symmetrically distributed over a range of ~40 meV, the distribution of PL energies of DNA-wrapped CNTs exhibited a tail at the low energy side and extended over more than 70 meV. An analysis of the PL peaks with highest intensity and highest energy in every PL spectrum revealed further discrepancies among DOC_{H_2O}, DOC_{org}, and DNA_{org} CNTs that were studied in more detail using the data of the respective E_{22} energies. Hereby, changes in strain, dielectric environment and defect-induced exciton localization could be discriminated. It was shown that the spread in the cryogenic PL energies of DOC-coated CNTs was mainly strain-induced, whereas defect-localized excitons dominated the PL of DNA-wrapped CNTs. One explanation for the surfactant-related strain is the thermal expansion or contraction of dried-off DOC residues covering the CNTs. In this framework, a class of DOC_{org} CNTs that did not follow the scaling observed for DOC_{H_2O} CNTs, was attributed to highly strained CNTs that partly slipped free from the surrounding matrix.

The class of PL peaks that simultaneously had the highest energy and intensity in a cryogenic PL spectrum was used to study the effect of drop-casting and cool-down on the CNT PL. The averaged cryogenic values of the PL and E_{22} energies of these peaks were compared to E_{11} and E_{22} values measured at room temperature in absorption of CNTs dispersed in aqueous solution. For all CNT materials the averaged cryogenic optical transition energies were blue-shifted by more than 20 meV and 10 meV for E_{11} and E_{22} , respectively, but the ordering of E_{11} and E_{22} between the CNT materials was not preserved at 4.2 K. The relative shift of DOC_{H_2O} and DOC_{org} CNTs was attributed to radial strain of DOC_{org} CNTs due the encapsulation of $C_{20}H_{42}$ molecules, at room temperature and to a combination of radial strain and a quasi-phase transition of water molecules in the DOC_{H_2O} CNTs at 4.2 K. The shift between E_{11} and E_{22} at 300 K in solution and at 4.2 K on a substrate was consistent with a decrease in the environmental dielectric constant. The relative energy shifts of E_{11} and E_{22} between DOC_{org} and DNA_{org} CNTs at

300 K and 4.2 K were related to a combination of environmental strain and dielectric effects.

Chapter 5

Photoluminescence excitation spectroscopy of carbon nanotubes

This chapter presents the analysis of various cryogenic carbon nanotube samples by photoluminescence excitation spectroscopy and describes a model to relate the obtained results to varying degrees of exciton localization. The photoluminescence excitation resonances of delocalized nanotube excitons were governed by nanotube-intrinsic phonons and accompanied by strong resonant Raman scattering. The phonon energies did depend on the nanotube chirality, but were not sensitive to environmental factors. Defect states in carbon nanotubes inherited excitation resonances from states with higher energy and did not exhibit Raman scattering which was attributed to the reduced number of carbon atoms that coupled to the defect-localized excitons. Most signatures typical for the photoluminescence excitation of carbon nanotubes were absent in the spectrally narrow photoluminescence emission from localized excitons in as-grown nanotubes. The photoluminescence excitation characteristics of these quantum dot-like excitons included resonances that were attributed to substrate phonons.

5.1 Introduction

The photoluminescence (PL) of cryogenic carbon nanotubes (CNT) is characterized by a large diversity of spectral signatures, such as symmetric, asymmetric [25, 26], and ultra-narrow [30] spectral lineshapes, multipeak PL emission [26, 33], and photon anti-bunching [28]. The analysis of the resonances in the PL emission as a function of the laser excitation energy, referred to as photoluminescence excitation (PLE) spectroscopy, offers a versatile method to further characterize and understand the broad range of cryogenic CNT PL characteristics.

In the past, PLE spectroscopy was employed to determine the optical transitions in CNTs [7, 19, 98] as well as several CNT phonon modes via the enhanced Raman signal when the laser excitation fulfills the resonance condition for Raman scattering [99]. Therefore, PLE spectroscopy is a suitable tool to simultaneously study the energy states and the complex phonon spectrum of CNTs. Most studies regarding the vibrational properties of CNTs used Raman spectroscopy [4, 100–103] with a focus on the G-band known from graphite and the radial breathing mode (RBM) unique to CNTs (see Section 2.5). First studies of phonon modes in the energy range between the RBM and the G-band, referred to as intermediate frequency modes (IFM), by Raman spectroscopy on chirality-mixed samples [99, 104–107] were not able to find a straight-forward explanation for their origin. More recent ensemble studies on chirality-purified CNT samples were able to assign IFM modes to specific phonon processes by coherent phonon spectroscopy [108], however, only at room temperature and not on a single-tube level. In this chapter, quantitative PLE studies of individual cryogenic CNTs in various dielectric environments and with different spectral PL signatures were performed using a low-temperature apochromatic objective.

5.2 Experimental methods

Carbon nanotube samples were prepared by drop-casting CNTs dispersed in solution onto a fused silica solid immersion lens (SIL) or by growing CNTs directly on a substrate using chemical vapor deposition (CVD). The class of solution-processed CNTs included pristine (9,1) CNTs with various combinations of CNT fillings and surfactants and alkyl-doped (6,5) CNTs. As-grown CNTs with a median diameter smaller than 1 nm were grown over trenches, on silicon oxide (SiO_2) and on hexagonal boron nitride (hBN). The CNT materials are summarized in Table 5.1 and described in more detail in Section 3.2. In the following the abbrevations from Table 5.1 will be used to refer to specific CNT samples.

In PLE spectroscopy, the PL intensity was recorded using a low-temperature apochromat while scanning the continuous wave excitation laser over the energy range that was determined by the color filters and limited by the tuning range of the laser and the chromaticity of the experimental setup. Spectroscopy on as-grown nanotubes and chirality-sorted (9,1) CNTs was performed using a microscope optimized for optical

Abbrevation	material	chirality	substrate	surfactant	filling
DOC_{H_2O}	solution	(9,1)	SIL	DOC	H_2O
DOC_{org}	solution	(9,1)	SIL	DOC	$C_{20}H_{42}$
DNA_{org}	solution	(9,1)	SIL	DNA	$C_{24}H_{50}$
DOC*	solution	(6,5)	SIL	DOC	empty/H_2O
CVD_{SiO_2}	as-grown	$[d]_m \leq 1$ nm	SiO_2	/	empty
CVD_{hBN}	as-grown	$[d]_m \leq 1$ nm	hBN	/	empty
CVD_{susp}	as-grown	$[d]_m \leq 1$ nm	suspended	/	empty

Table 5.1: Summary of the studied CNT materials. Row 2-5: CNTs applied to a solid immersion lens (SIL) by drop-casting from aqueous solution are labeled according to the surfactants sodium deoxycholate (DOC) and DNA. The index refers to the filling with water or organic molecules. Alkyl-doped (6,5) CNTs are marked by an asterisk. Row 6-8: The abbreviation CVD labels as-grown CNTs with the median of the diameter distribution $[d]_m \leq 1$ nm. The index distinguishes nanotubes suspended over trenches, grown on silicon oxide (SiO_2), or on hexagonal boron nitride (hBN).

studies in the energy range 1.3 – 1.8 eV. Alkyl-doped (6,5) CNTs were studied with a setup designed for excitation energies below 1.51 eV, which limited the detection of Raman resonances to phonon modes with energies below 220 meV as shown in Figure 5.4b. The PLE data is presented either as PL intensity color maps with the detected spectral range and the excitation energy as horizontal and vertical axis, respectively (e.g. Figure 5.2a) or as a plot of the PL intensity within a selected spectral band (indicated by an arrow in the respective color map) as a function of the laser detuning from the PL energy (e.g. Figure 5.2b). In all PL intensity plots the highest peak was normalized to unity. Unless otherwise stated, all measurements were performed at 4.2 K and the polarization of the excitation laser was parallel to the CNT axis.

5.3 Pristine carbon nanotubes

To establish a well-defined starting point for studying the role of intrinsic and extrinsic factors on the PLE characteristics of cryogenic CNTs, first measurements were performed on as-grown CNTs that were suspended over a trench in an inert helium atmosphere, thereby minimizing environmental influences. Such a CNT is marked by the gray circle in the PL raster scans in Figure 5.1a and b, recorded with an avalanche photodiode (APD) at room temperature and with a spectrometer and a charge-coupled device (CCD) at 4.2 K, respectively. The spatial extent of the PL emission and the symmetric single-peak PL spectrum (Figure 5.1c) suggest that, despite the cryogenic temperatures, the PL stemmed from diffusive excitons and was not modified by unintentional exciton localization [33]. The peak emission energy was in very good agreement with that of chirality purified (6,5) solution-processed CNTs at 4.2 K (see Section 5.3.1).

The corresponding PLE map in Figure 5.2a shows two distinct features: The PL signal (along the black arrow) with an emission energy independent of the excitation energy

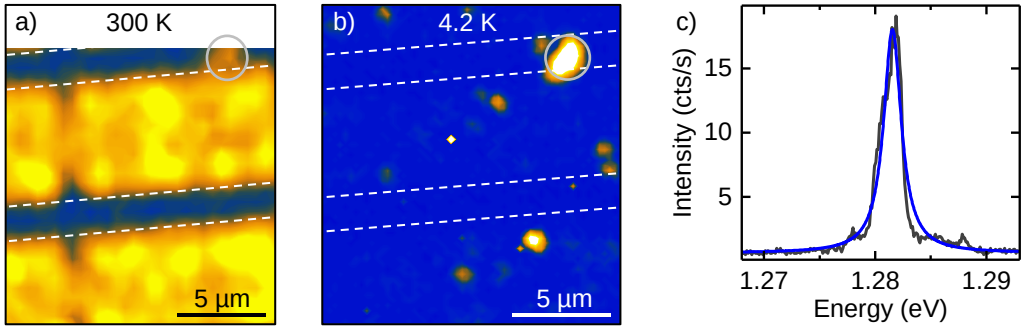

Figure 5.1: a) PL map of a SiO_2 substrate (yellow) with etched trenches (blue) marked by the white dashed lines and CNTs grown by chemical vapor deposition, recorded by an avalanche photodiode at room temperature. The PL form a suspended CNT is marked by the gray circle. b) The spectrally resolved PL map (shown is the intensity of the PL maxima) of the sample region in (a) at 4.2 K also shows the spatially extended CNT PL from (a). c) PL spectrum of the emitter marked in (b). The blue solid line is a Lorentzian fit to the data with a full-width at half-maximum spectral linewidth of 2 meV.

and a Raman signal that stems from inelastically scattered laser photons (diagonal stripes). The energy difference between the Raman photons and the excitation laser corresponds to the energy of the specific CNT phonon that is created in the Raman process. The Raman signal gradually increases in intensity as it approaches the PL energy. When the scattered resonance condition is fulfilled, i.e. when the Raman photons have the same energy as the PL, a strong signal enhancement is observed (see Section 2.5). Figure 5.2b shows the PL intensity along the black arrow in Figure 5.2a as a function of the energy difference between the excitation laser and the PL. Apart from the strong G^+ peak, nine additional resonances were identified and assigned to higher-order phonon processes with the help of the findings from coherent phonon spectroscopy on a macroscopic sample of highly enriched (6,5) CNTs at room temperature [108]. The results are summarized in Table 5.2. A more detailed analysis of chirality-specific phonon modes is given in the next section.

Peak #	G^+	1	2	3	4
Energy (meV)	195	205	211	218	222
Assignment		G^+ +iTA	G^- +LA	G^+ +LA	G^- +iTA+LA

Peak #	5	6	7	8	9
Energy (meV)	224	229	232	259	266
Assignment	G^- +RBM	G^+ +iTA+LA	G^+ +RBM	G^- +2 RBM	G^+ +2 RBM

Table 5.2: Energies of PLE resonances for the suspended (6,5) carbon nanotube in Figure 5.2b. All resonances are assigned to combinations of the radial breathing mode (RBM), the G-band (G^+ and G^-), and the in-plane transverse acoustic (iTA) and the longitudinal acoustic (LA) phonons.

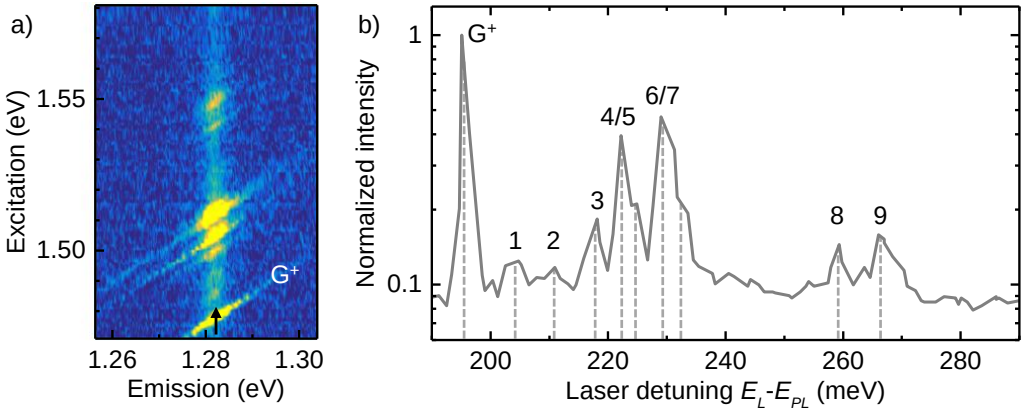

Figure 5.2: a) PLE map of the suspended (6,5) CNT from Figure 5.1 at 4.2 K. A strong signal enhancement was observed when the Raman scattered laser photons (diagonal stripes) and the PL emission (along the black arrow) were resonant. b) PL intensity along the black arrow in (a) as a function of the energy difference to the excitation laser. Apart from the pronounced G^+-band peak, several multi-phonon resonances were observed (gray dashed lines at energies listed in Table 5.2).

To interpret the PL spectra, it is important to know whether the resonances in Figure 5.2b were caused by an enhancement of the Raman scattering, of the PL emission, of both, or just by the overlap of the two individual signals. A procedure to extract the Raman and PL contribution to the detected intensity is depicted in Figure 5.3 for the CNT from Figure 5.2 on the example of the G^+-band. The spectral linewidths of the PL and the Raman signal were determined by a double-Lorentzian fit to an off-resonant spectrum (Figure 5.3b) yielding 2.7 meV (red) and 1.1 meV (green) spectral linewidth at full-width at half-maximum (FWHM), respectively. This difference was sufficient to deconvolve Raman and PL contributions and obtain their respective intensities even when they emitted at the same energy. Figure 5.3c shows the integrated intensity of the

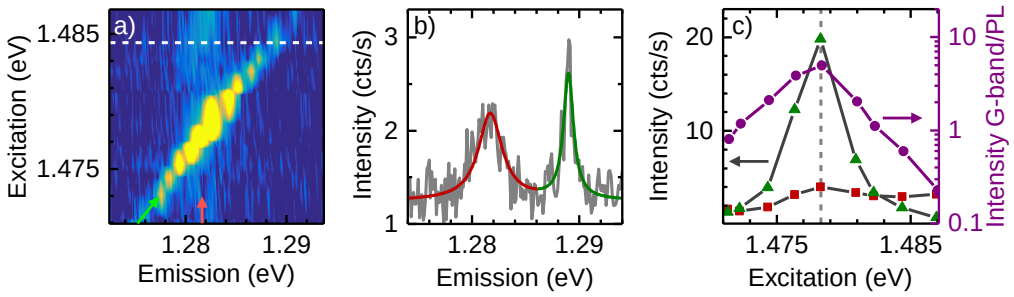

Figure 5.3: a) PL and Raman G^+-band signal of the freely suspended as-grown (6,5) CNT from Figure 5.1. b) PL spectrum along the white dashed line in (a). The solid line is a double-Lorentzian fit to the data (red and green mark the PL and the Raman peak, respectively). c) Integrated intensity of the Raman and the PL signal (green triangles and red rectangles, respectively) as a function of the excitation energy (the gray dashed line marks the resonance condition). The ratio of the two intensities (purple data) is shown on a logarithmic scale.

Raman and the PL emission as a function of the excitation energy (green triangles and red rectangles, respectively). Both signals were enhanced on resonance, where the effect was much stronger for the Raman signal. The ratio of the Raman and the PL intensity (purple data) starting below unity for off-resonant excitation increased by more than one order of magnitude on resonance. This dominance of Raman-scattered laser photons at all PL resonances, together with the very weak off-resonant PL intensity renders observations of PL characteristics very difficult. On the other hand, the strong Raman signal allows to determine the energies of a variety of phonon modes and consequently the energy of all Raman-active CNT phonons. Pristine CNTs were therefore an ideal system to study the CNT phonon structure and its dependence on various parameters, such as chirality and dielectric environment, on a single nanotube level.

5.3.1 Chiral-angle dependence of carbon nanotube phonon modes

The diameter-dependence of various CNT phonon modes, especially the RBM and the G-band, has been studied extensively [4, 100–103]. The (6,5) and (9,1) chiralities studied in this section are predestined for a diameter-independent analysis of the CNT phonon energies because, despite their different chiral angles[1] and $(n-m)$mod3 values, they have the same diameter.

The representative PLE scan of a (6,5) DOC* CNT in the spectral band of the bright exciton shown in Figure 5.4a exhibits several Raman modes marked by white dashed lines. The bright, spectrally broad emission in the lower left corner was the autofluorescence of the substrate. The PL intensity of the bright exciton is very weak and its spectral position is identified mainly by the enhancement of the Raman modes. In accord with the pronounced Raman defect mode, this is attributed to defect-induced low-energy states that cause the bleaching of the bright exciton [37] as discussed in Section 5.4. Figure 5.4b shows the PL intensity along the white arrow in Figure 5.4a as a function of the energy difference between excitation laser and PL emission. The gray dashed lines correspond to the Raman modes marked in Figure 5.4a. Every number represents a specific combination of CNT phonons, namely the in-plane transverse acoustic (iTA), the longitudinal acoustic (LA), the radial breathing mode (RBM), the out-of-plane optical (oTO), the in-plane transverse optical (iTO or G^-), and the longitudinal optical (LO or G^+) phonon as summarized Table 5.3. The different colors distinguish between phonon combinations involving no acoustic phonon, an iTA, an LA, or both acoustic phonons (dark gray, yellow, blue, and green, respectively). The defect mode D is labeled in light gray. All values were in good agreement with results obtained from coherent phonon spectroscopy on a macroscopic sample of (6,5) CNTs at room temperature [108], within a measurement error of ±1.5 meV. This error was determined by the tube-to-tube variations in the G^+-band energy among all studied CNTs.

In a next step, the PLE data of the (6,5) CNT was compared to that of the (9,1) DOC_{H_2O} CNT shown in Figure 5.4c and d. As expected, the energies of the G^+-band and the RBM,

[1] 27.00 ° and 5.82 ° for (6,5) and (9,1) CNTs, respectively

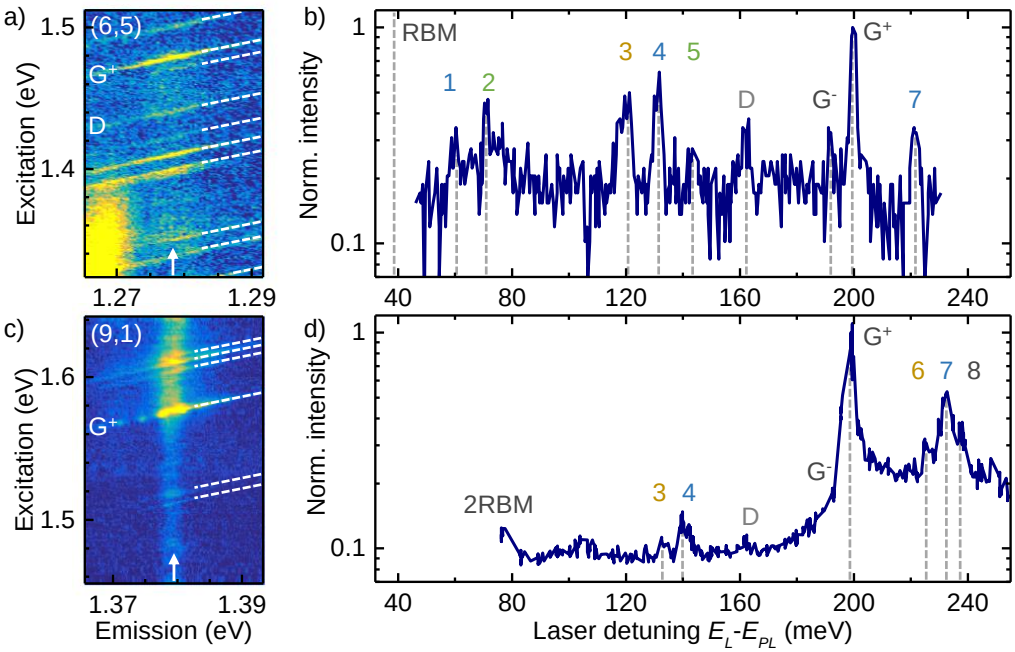

Figure 5.4: a) and c) PLE map in the spectral band of the bright exciton of (6,5) DOC* and a (9,1) DOC_{H_2O} CNT, respectively. Raman modes are indicated by white dashed lines. The bright emission in the lower left corner in (a) stems from the autofluorescence of the substrate. b) and d) Corresponding PL intensities along the white arrows as a function of the energy difference between the excitation laser and the PL. The Raman modes identified in (a) and (c) are indicated by gray dashed lines in (b) and (d), respectively. Processes involving only optical phonons are labeled in gray. All other Raman modes are labeled according to the creation of a transverse acoustic, a longitudinal acoustic or both acoustic phonons (yellow, blue, and green, respectively). The resonance due to the RBM overtone (2 RBM), the D-mode, and the G^--band of the (9,1) CNT are barely visible in c). The labeling does not correspond to that of the PLE resonances of the suspended CNT in Figure 5.2.

calculated from the RBM overtone (2 RBM) in the case of the (9,1) CNT, were identical for both chiralities. The remaining PLE resonances, however, did not coincide with those measured for the (6,5) chirality. Therefore at least some of the (9,1) CNT phonons have to differ in energy compared to the (6,5) CNT. The collected data was sufficient to assign all (9,1) resonances to specific phonon combinations. The labeling follows the same scheme as in Figure 5.4b. By comparing the energies of the PLE resonances that were attributed to the same phonon combinations, the chirality-specific phonon energies for (6,5) and (9,1) CNTs were obtained as listed in Table 5.4. While the energy of the optical CNT phonons was independent of the chirality within the accuracy of the measurement, the acoustic phonons of the (9,1) CNT were shifted to higher energies by more than 10 meV compared to the (6,5) CNT. This discrepancy was either related to the different chiral angle, or to the fact that (6,5) and (9,1) belong to different CNT families with $(n-m)\text{mod}3 = 1$ and 2, respectively. In the case of the (9,1) CNT, the G^- and G^+ resonances were merged into one peak dominated by the latter. Due to the high sample quality of the (9,1) CNTs, consistent with the strong PL emission from the

Peak #		1	2	3	4	5
Assignment	RBM	RBM +LA	RBM +iTA+LA	oTO +iTA	oTO +LA	oTO +iTA+LA
Energy (6,5) (meV)	39	60	70	121	132	143
Energy (9,1) (meV)	39	/	/	133	141	/

Peak #				6	7	8
Assignment	D	G^- (iTO)	G^+ (LO)	G^+ +iTA	G^+ +LA	G^+ RBM
Energy (6,5) (meV)	161	191	200	/	221	/
Energy (9,1) (meV)	161	/	199	225	232	238

Table 5.3: Assignment of the PLE resonances to phonon modes for the (6,5) and (9,1) CNT from Figure 5.4. Processes involving only optical phonons are labeled in gray. All other Raman modes are labeled according to the creation of an iTA, a LA or both acoustic phonons (yellow, blue, and green, respectively). The labeling does not correspond to the labeling in Figure 5.2.

bright exciton and the absence of PL side peaks, the ratio of the D and G^+-band was much smaller as compared to the (6,5) CNT. The resonance due to the creation of a G^+ and an iTA phonon (peak number 6), the third-order Raman modes (peak numbers 2 and 5) and the RBM overtone were each observed for only one chirlality, probably due to chirality-dependent differences in the photon-exciton or exciton-phonon coupling matrix elements.

Despite different dielectric environments, all PLE resonances of the (6,5) CNT were consistent with the data obtained from the as-grown suspended (6,5) CNT in Figure 5.2. The next section will focus on the effect of environmental changes on the PLE resonances and the phonon energies by comparing the PLE resonances DOC_{org}, DOC_{H_2O}, and DNA_{org} CNTs.

Phonon mode (symmetry)	Energy (meV) (6,5)	Energy (meV) (9,1)
iTA (1st E_2)	10	26
LA (2nd E_1)	21	33
RBM (3rd A)	39	39
oTO (4th A)	110	108
D	161	/
iTO or G^- (5th A)	191	/
LO or G^+ (6th A)	200	199

Table 5.4: Phonon energies calculated from Table 5.3. Colors differentiate between transverse acoustic (iTA), longitudinal acoustic (LA) and optical phonons (yellow, blue and gray, respectively). The corresponding phonon symmetries are discussed in Ref. [108] and Section 2.5.

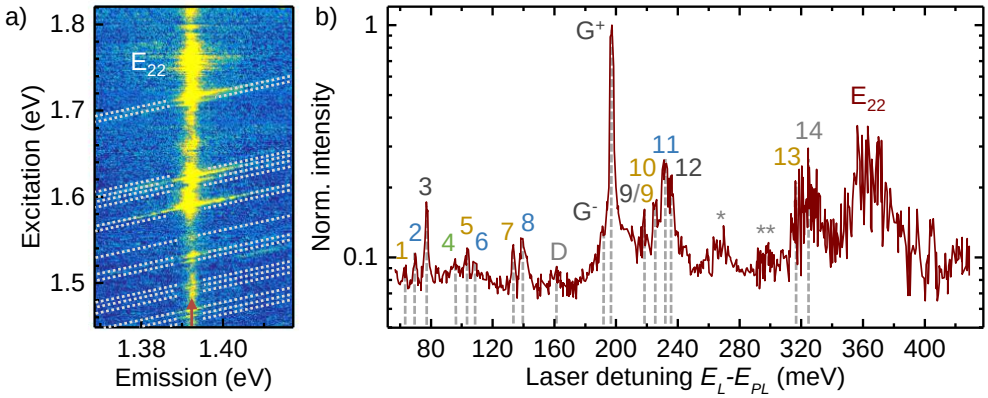

Figure 5.5: a) PLE map of a DOC_{org} CNT. Raman modes are indicated by diagonal white dashed lines as guides to the eye. b) PL intensity along the brown arrow in (a) as a function of the energy difference between laser excitation and PL. The Raman modes identified in (a) are indicated by gray dashed lines and numbered by ascending energy. Processes involving only optical phonons are labeled in dark gray. All other Raman modes are labeled according to the creation of a transverse acoustic, a longitudinal acoustic or both acoustic phonons (yellow, blue, and green, respectively). The defect mode (D) and its overtone are labeled in light gray. The broad peaks marked by one and two asterisks are superpositions of resonances involving three or more phonons with at least two optical phonons. The graph also includes the E_{22} resonance.

5.3.2 Influence of carbon nanotube surfactant and filling on Raman scattering

Figure 5.5 shows the PLE data of a DOC_{org} CNT for which more Raman modes could be resolved compared to Figure 5.4c, possibly due to a larger phonon-exciton coupling matrix element for this specific CNT. Analogous to the previous section, the Raman modes in Figure 5.5a are marked by white dashed lines. The broad resonance at high excitation energies is not related to a Raman process, but to the excitation via the next higher energy band E_{22}. The PL intensity along the brown arrow is shown in Figure 5.5b as a function of the energy difference between the excitation laser and the PL. The Raman modes that were identified in Figure 5.5a are indicated by gray dashed lines and are numbered by ascending energy. Using Table 5.4, they were assigned to specific phonon combinations as summarized in Table 5.5. The label colors correspond to the involved acoustic phonons analogous to the previous section.

It is noteworthy that, even though the energy interval scanned by the excitation laser covers almost the whole spectral range between the CNT E_{11} and E_{22} transition, no signatures of excited exciton states were observed. A possible explanation for the absence of these states is the small diameter of the (9,1) CNTs combined with an unusually low E_{22} energy. Expanding the empirical models in Ref. [109] and [110] to CNTs with diameters of 0.7 nm predicts an energy spacing between the exciton ground state and the first excited state that is larger than 450 meV and therefore lies above the E_{22} transition and outside the energy interval accessible by the titanium-sapphire laser.

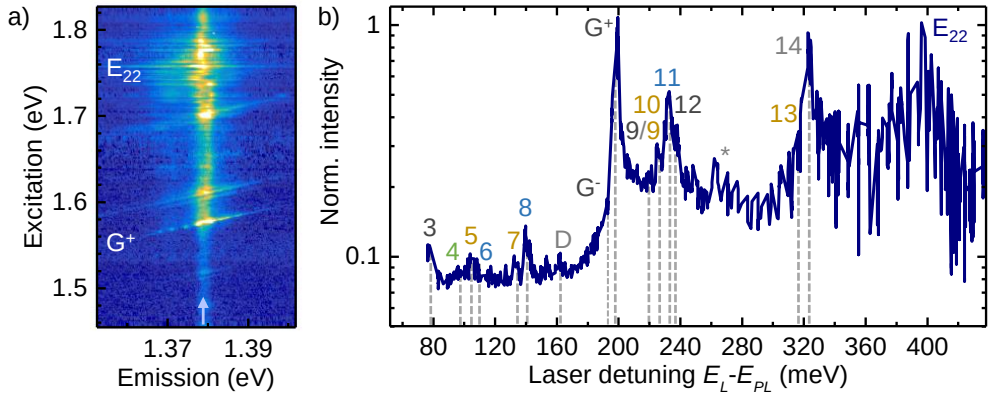

Figure 5.6: a) PLE map of a DOC_{H_2O} (9,1) CNT. b) Intensity along the blue arrow in (a) as a function of the laser detuning. Dashed gray lines mark the phonon resonances from Figure 5.5. The peak labeling is analogous to Figure 5.5.

To study the influence of the CNT filling on the PLE characteristics, the Raman resonances of the DOC_{org} CNTs were compared to the PLE data of the DOC_{H_2O} CNT shown in Figure 5.6. To facilitate the comparison, the resonances identified for the DOC_{org} CNT in Figure 5.5b are included as gray dashed lines in Figure 5.6b. Within the accuracy of the measurement, no differences in the PLE characteristics were observed. The different energy separations of the E_{22} resonance from the PL (370 meV and 400 meV for Figure 5.5b and Figure 5.6b, respectively) arise from the fact that these resonances are not connected to a Raman process. The relationship between the energy of the PL and the E_{22} resonance is discussed in more detail in Section 4.4.1.

Surfactant-dependent effects were studied by comparing CNTs coated with DOC to DNA-wrapped CNTs (DOC_{org} and DNA_{org} samples, respectively). The most obvious difference in the PLE map of the DNA_{org} CNT shown in Figure 5.7 as compared to Figure 5.5 and Figure 5.6, was the occurrence of a red-shifted PL satellite peak. Such peaks

Peak #	1	2	3	4	5	6	7
Energy (meV)	64	69	77	96	103	110	134
Assignment	RBM +iTA	RBM +LA	2 RBM	RBM +iTA+LA	2 RBM +iTA	2 RBM +LA	oTO +iTA

Peak #	8	9/9	10	11	12	13	14
Energy (meV)	138	218	224	230	236	316	323
Assignment	oTO +LA	2 oTO /G^- +iTA	G^+ +iTA	G^+ +LA	G^+ +RBM	G^+ +oTO +iTA	G' (2 D)

Table 5.5: Assignment of the PLE resonances from the (9,1) CNT in Figure 5.5b to phonon modes. Processes involving only optical phonons are labeled in gray. All other Raman modes are labeled according to the creation of an iTA, a LA or both acoustic phonons (yellow, blue, and green, respectively). The numbers do not correspond to the labeling in Figure 5.4.

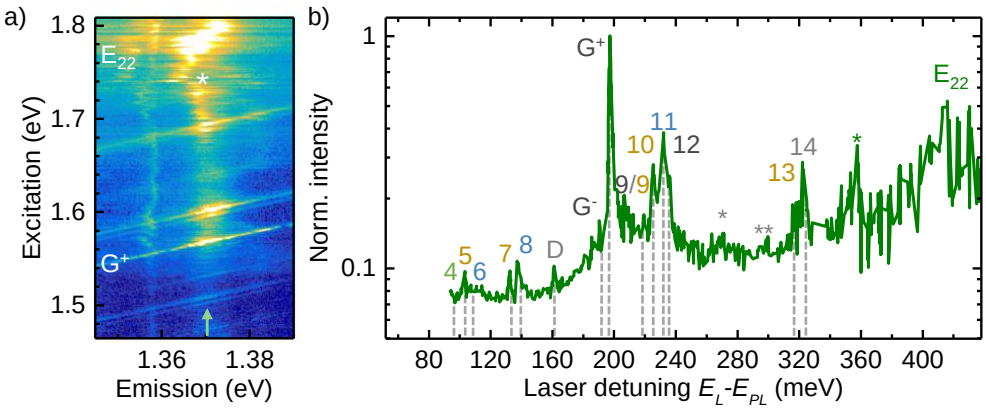

Figure 5.7: a) PLE map of a DNA_{org} (9,1) CNT. b) PL intensity along the green arrow in (a) as a function of the laser detuning. Dashed lines mark the phonon resonances of Figure 5.5. The peak labeling is analogous to Figure 5.5. The peak marked by the green asterisk belongs is part of the broad E_{22} resonance, the drop in PL intensity between this peak and E_{22} is caused by the large spectral shift marked by the white asterisk in (a).

were omnipresent in DNA-wrapped CNTs and are a hallmark of exciton localization at defects [33]. Consistently, a pronounced defect Raman mode is observed in Figure 5.7 in contrast to CNTs with a DOC surfactant. The defects in DNA-wrapped CNTs are either introduced by the DNA itself or are a consequence of a less effective isolation from the environment. The energy of the PLE resonances, however, remained unchanged as compared to the resonances of the DOC_{org} CNT indicated as gray dashed lines in Figure 5.7b. In summary, the PLE characteristics of the bright exciton (not the defect state) did not depend on the filling nor the surfactant of the studied CNTs. The characteristic PLE signatures of defect states will be discussed in the next section.

5.4 Defects in carbon nanotubes

Figure 5.8a shows a magnification of the PLE scan of the DNA_{org} CNT from Figure 5.7a centered around the G^+ Raman mode. Performing the same deconvolution of the PL and Raman intensities as in Figure 5.3 revealed a fundamental difference between the PL emission of the bright exciton and the red-shifted emission from the presumably defect-localized state. On resonance with the unperturbed PL emission, Raman scattering is enhanced by an order of magnitude (Figure 5.8c) compared to the PL, similar to the suspended CNT in Figure 5.3. This is contrasted by the data shown in Figure 5.8b. When the Raman scattering is resonant with the defect PL, the ratio of their respective intensities remained unchanged and the overall signal intensity is simply the sum of the off-resonant components (not shown here).

Further studies of the CNT PLE characteristics in the presence of defects were performed on alkyl-doped (6,5) DOC* CNTs. The doping in this material causes the emergence of PL peaks at 1.13 eV and 1.01 eV, which is below the detection limit of silicon-based photodetectors. However, several additional PL satellite peaks with energies near

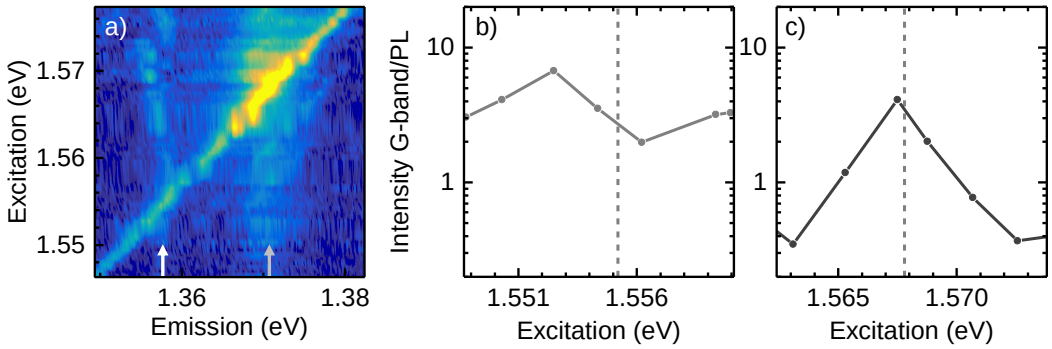

Figure 5.8: a) PLE map of the CNT from Figure 5.7 in the energy range where the Raman G^+-band coincides with the PL from the bright exciton and the red-shifted satellite peak. b) and c) Ratio of Raman and PL intensities along the white and the gray arrows in (a), respectively, as a function of the excitation energy. The gray dashed lines mark the respective resonances. The variations in the G-band/PL intensity ratio in (b) are caused by intensity fluctuations of the PL satellite peak.

the E_{11} transition were observed, which will be the focus of the following studies.

In the PLE map of the DOC* CNT shown in Figure 5.9a, the PL intensity of the bright exciton (blue arrow) is very weak and only identified by the enhancement of the Raman modes, similar to the DOC* CNT in Figure 5.4a. Several bright PL features occur at energies red-shifted by 20 – 70 meV compared to the bright exciton. In accord with the pronounced Raman defect mode, this is attributed to defect-induced or defect-brightened low-energy states that cause the bleaching of the bright exciton [37]. In fact, assuming an effective dielectric constant of 2.3,[2] the energy difference of about 20 meV between the PL peaks marked by the blue and the purple arrow agrees with the energy splitting expected between the bright and the parity-forbidden dark exciton [111]. Both peaks exhibit a symmetric spectral lineshape and enhanced Raman scattering.

These results are contrasted by the PL and PLE characteristics of the two low-energy peaks indicated by the pink and red arrow in Figure 5.9a, for which no enhanced Raman scattering was observed. Their energy shifts of 30 meV and 50 meV relative to the bright exciton, the increased spectral wandering, and the asymmetric spectral lineshape, especially of the PL peak at 1.23 eV, are consistent with PL from localized excitons.

Figure 5.9b compares the PL intensity of the four peaks marked in Figure 5.9a as a function of the energy difference between the excitation laser and the respective PL emission (note that the PL intensity is plotted on a linear and not a logarithmic scale). The blue-most peak (blue data) exhibits pronounced resonances related to Raman modes, similar to the CNT in Figure 5.4b. The emission associated with the dark exciton (purple data) has a similar intensity profile, with slightly broadened resonances and an overall increase of the PL intensity between the D-band and the G^++iTA+LA multi-phonon resonance. The PLE resonances of the PL peak at 1.25 eV (pink) are much less pronounced and the energy range with an increased PL intensity is shifted to higher

[2] This value was aproximated by an equal conribution of the dielectric constants of the substrate(~4.0), the CNT (1.8 [111]) and the helium atmosphere (~1.0)

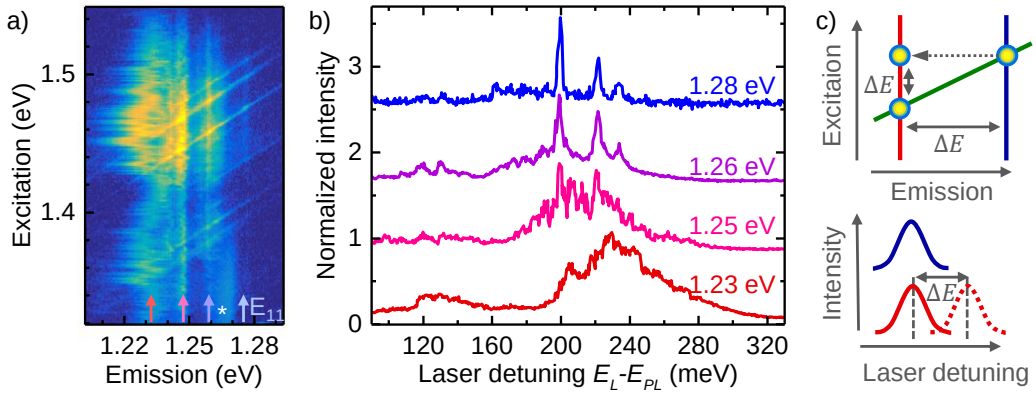

Figure 5.9: a) PLE map of an alkyl-doped (6,5) DOC* CNT with four PL peaks marked by colored arrows. The diagonal stripes are Raman scattered photons and the broad emission marked by the white asterisk is the fluorescence of the substrate. b) PL intensity along the colored arrows in (a). c) Illustration of the mechanism responsible for the PLE resonances in multi-peak PL spectra. The upper panel shows a simplified version of the PLE map in (a): The PL intensity of both peaks exhibits a maximum (colored circles) at the crossing of the Raman line (green solid line). In addition, the red-shifted PL signal, indicated by the red solid line, inherits the resonances of the high-energy state (blue solid line) separated by the energy ΔE via non-radiative exciton relaxation (indicated by the dashed arrow). Lower panel: The non-radiative exciton decay causes a second PLE resonance for the low-energy PL peak that is shifted to larger laser detunings by ΔE (dashed red line).

laser detunings and is not centered around the G^+-band. In the case of the PL peak at 1.23 eV (red), the increased loss of contrast and the shifting of the PLE resonances with decreasing emission energy results in one broad structured resonance up-shifted by 30 meV as compared to the blue data.

This phenomenon was related to the relaxation of excitons to low-energy states as illustrated in Figure 5.9c. PL peaks exhibit an increase in intensity whenever the sum of PL energy and a Raman-active phonon equals the laser energy as illustrated by the crossing of the green line with the blue and the red line in the schematic PLE map in the upper panel of Figure 5.9c. In addition, the PL from the defect state (red line) is enhanced by the non-radiative relaxation of excitons from the high-energy state (dashed arrow). By this mechanism, the defect PL inherits the PLE resonance of the high-energy states, which leads to the additional resonance peak in the lower panel of Figure 5.9c (red dashed curve). The energy difference ΔE is given by the energy separation of the two states. For multiple phonon resonances this results in a broadening of the PLE resonances of defect states accompanied by a global shift to higher laser detunings. This effect becomes more pronounced with every additional low-energy state that potentially inherits the resonances of all higher states, as observed in Figure 5.9b.

An attempt to understand the absence of Raman scattering for some emission peaks and the bleaching of the E_{11} transition in the framework of defects and exciton localization is presented in Figure 5.10. The schematic energy diagrams in Figure 5.10d-f include exciton energy levels and the related phonon-dressed states as solid and dashed hori-

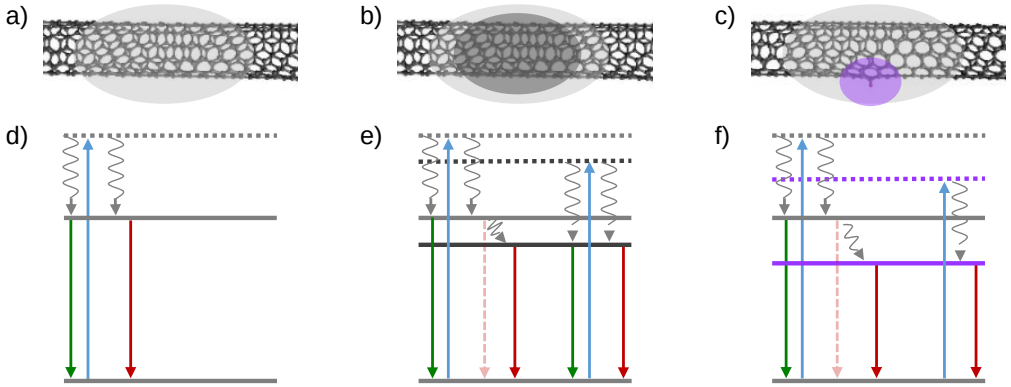

Figure 5.10: a-c) Illustration of a CNT with the delocalized bright exciton (gray), combined with a low-energy delocalized defect-brightened (dark grey) or defect-localized state (purple) (a, b, and c, respectively). d-f) Corresponding schematic energy diagrams including excitons and the related phonon-dressed states (solid and dashed horizontal lines, respectively) for laser excitation (blue arrow) via a phonon-dressed exciton state. Raman scattered and PL photons are depicted by green and red arrows, respectively. The delay between non-radiative exciton relaxation and PL emission is indicated by the horizontal offset between the wiggled and the red arrows. d) PL emission combined with Raman scattering at excitation via a phonon resonance (gray dashed line). e) Same as (d), but with an additional low-energy delocalized exciton state (black), that is populated by the same process as in (a) (right side) or by relaxation from the high-energy state (left side, diagonal gray wiggled arrow), which reduces the PL intensity of the high-energy state (red dashed arrow). Both states resonantly enhance Raman scattering (green arrows). f) Same as (a), but with an additional low-energy defect-localized state (purple) that does not resonantly enhance Raman scattering.

zontal lines, respectively. Transitions between these states involve either a photon or a phonon indicated by colored straight and gray wiggled arrows, respectively. Optical transitions are categorized into laser excitation, Raman scattering, and PL emission (blue, green, and red, respectively). The case of a pristine CNT with excitation via a phonon replica is illustrated in Figure 5.10a and d. PL is emitted from the delocalized bright exciton (light gray oval and gray solid horizontal line in a and b, respectively) accompanied by Raman scattering. The data shown in Figure 5.2, Figure 5.5, and Figure 5.6 are examples of this scenario showing enhanced Raman scattering and single-peak PL emission. Defects in the CNT can brighten transitions below E_{11} like the parity-forbidden dark exciton that are, however, still considered as delocalized in this model as indicated by the dark gray oval in Figure 5.10b. These states exhibit PL spectral lineshapes and PLE characteristics similar to the PL of bright excitons and show enhanced resonant Raman scattering at PLE resonances. In addition, relaxation of excitons to the low-energy state as depicted in Figure 5.10e can result in a bleaching of the E_{11} exciton PL (dashed red arrow) and in new PLE resonances of the defect-brightened state as illustrated in Figure 5.9c. The PLE characteristics of the two high-energy PL peaks in Figure 5.9a are an example of such a scenario where the PL with lower energy was associated with the defect-brightened parity-forbidden singlet exciton.

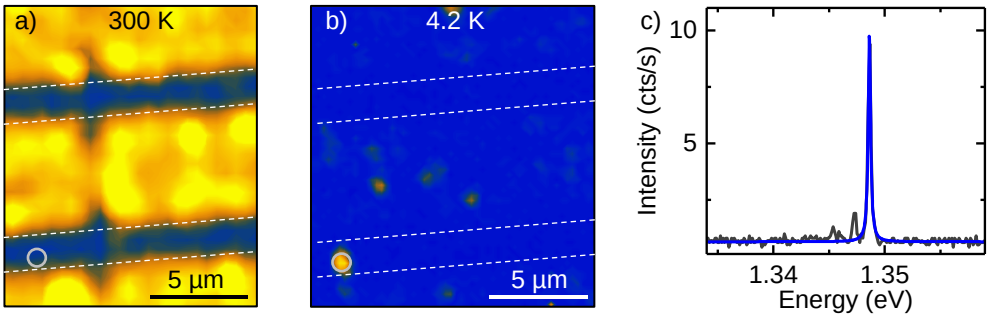

Figure 5.11: a) PL map of a SiO_2 substrate with etched trenches (blue, edges are marked by white dashed lines) and CNTs grown by chemical vapor deposition, recorded by an avalanche photodiode at room temperature. b) Hyperspectral PL map (shown is the intensity of the PL maxima) of the region in (a) at 4.2 K. The spot size-limited PL emission above the trench in the lower left corner was absent at room temperature (gray circles). c) PL spectrum of the suspended emitter in (b). The blue solid line is a Lorentzian fit to the data with a full-width at half-maximum linewidth of 0.27 meV.

Following the model presented in Figure 5.10, the absence of enhanced Raman scattering for the low-energy PL emission in Figure 5.7a and Figure 5.9a can be explained in the framework of defect-localized excitons. Individual defects in the CNT lattice, for example created by a covalently bound oxygen atom, create trap potentials that localize excitons as indicated by the purple oval surrounding the lattice defect in Figure 5.10c. The corresponding energy diagram depicted in Figure 5.10f is very similar to that in Figure 5.10e, but the defect-brightened state has been replaced by the low energy state of a defect-localized exciton and the corresponding phonon replica (purple solid and dashed line, respectively). Since the phonon-exciton coupling matrix element in a Raman process is proportional to the number of involved carbon atoms, the confinement of the exciton wavefunction to only a few lattice sites may be responsible for the suppressed resonant Raman enhancement at these states (absence of the green arrow). This assumption was supported by the increased spectral jitter and the changes in the PL spectral lineshape observed for the low-energy PL peaks in Figure 5.9a, that were consistent with a permanent electric dipole moment [41, 42] and the modified interaction with the CNT phonon bath [112–114] of localized CNT excitons, respectively. A class of as-grown nanotubes in which exciton localization suppresses most CNT characteristics is discussed in the next section.

5.5 Carbon nanotube quantum dots

A PL map of a CVD_{susp} sample at room temperature and the corresponding hyperspectral PL map at 4.2 K are shown in Figure 5.11a and b, respectively. The PL from the suspended CNT, marked by the gray circle in Figure 5.11b was only observable at cryogenic temperatures from an area smaller than the confocal spot size and exhibited a FWHM spectral linewidth near the resolution limit of the spectrometer in contrast

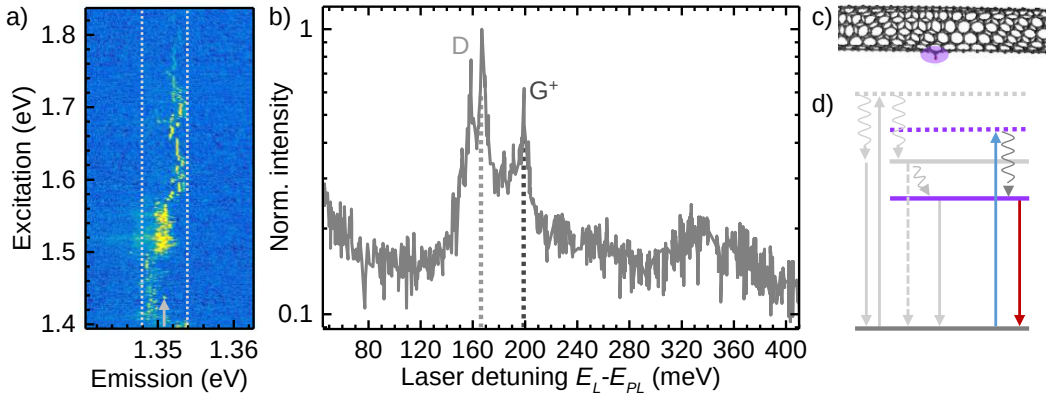

Figure 5.12: a) PLE map of the suspended CNT from Figure 5.11. b) PL intensity along the gray arrow in (a) integrated over the spectral band indicated by the white dotted lines. The resonances related to the defect mode (D) and the G^+-band are marked by light grey and dark gray dotted lines, respectively. c) and d) Corresponding modification of the model in Figure 5.10c and f. All delocalized exciton states and the corresponding transitions are removed (light gray) and substituted by a strongly localized defect-state (purple oval). d) Radiative decay (red arrow) and excitation (blue arrow) of excitons are only possible via the localized state indicated by the purple solid line and the corresponding phonon replica (purple dashed line), respectively.

to the spatially extended and spectrally broad PL emission of the suspended CNT in Figure 5.1. These localized and spectrally narrow PL emitters were predominantly found in CVD-grown CNTs and will be denoted as CNT quantum dots (QD) in the following.

Figure 5.12 shows the PLE data of the emitter in Figure 5.11c which differs substantially from the results obtained for the pristine and the alkyl-doped solution-processed CNTs in Section 5.3 and Section 5.4, respectively. Apart from the pronounced spectral diffusion, the most obvious discrepancies are the absence of Raman scattered photons in Figure 5.12a and the pronounced PL resonance related to the defect mode in Figure 5.12b. These observations are consistent with disorder-induced exciton localization [30] and can be described by the model presented in Figure 5.10f.

However, defect states as depicted in Figure 5.10f, should show PLE resonances related to exciton-relaxation from high-energy states (e.g. Figure 5.9b, pink data) which were not observed for the suspended CNT in Figure 5.12b in accord with the absence of a high-energy state showing Raman enhancement like in Figure 5.4 and Figure 5.9. In addition, Figure 5.12b does not show resonances related to CNT-specific phonons such as the RBM or acoustic phonons, but only the defect mode and the G-band that are present in all carbon-based systems. To resolve these contradictions, the model from Figure 5.10f was modified by removing all CNT-intrinsic energy levels as depicted in Figure 5.12c and d. In this framework, the CNT QD does not inherit the photophysical properties of the CNT and behaves like a carbon-based QD.

In contrast to delocalized excitons, the PLE resonances of CNT QDs are modified by the dielectric environment as evidenced by the comparison of the PLE data from suspended CNTs to CNTs on hBN shown in Figure 5.13. Similar to suspended nanotubes,

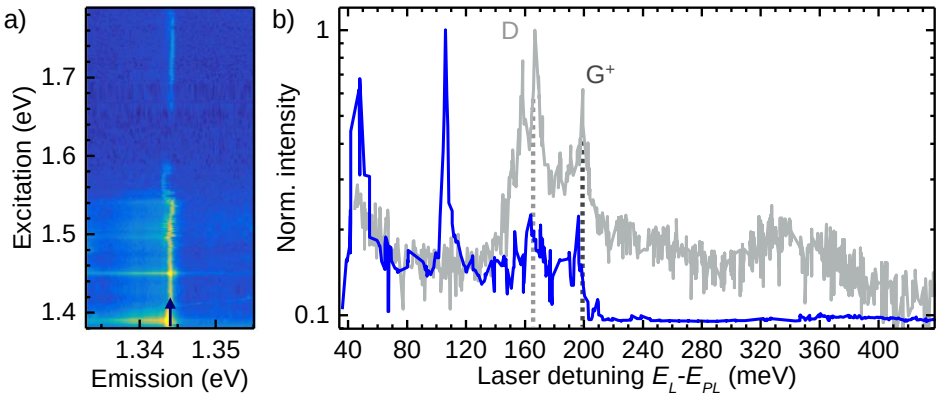

Figure 5.13: a) PLE map of a CVD_{hBN} CNT. b) PL intensity along the blue arrow in (a) (blue data). The position of the D and G^+ band are marked by light and dark gray dotted lines, respectively. The PLE resonances of the suspended CNT from Figure 5.12b are shown in gray for comparison.

the PL from the CVD_{hBN} CNT in Figure 5.13a exhibits a FWHM spectral linewidth below 0.3 meV, a low-energy wing in the PL spectrum at the PLE resonances (Figure 5.13a) and shows no sign of Raman scattering. Both CNT materials are characterized by the broad PLE resonances associated with the D-mode and the G-band as shown in Figure 5.13b, where the PLE resonances from the suspended CNT in Figure 5.12b were added in light gray for a better comparison. In contrast to suspended CNTs, however, two strong additional resonances around 50 meV and 110 meV occur for as-grown CNTs on hBN.

To check the validity of this observation, the averaged PLE resonances of CVD_{susp} and CVD_{hBN} CNTs were compared in Figure 5.14 as a function of the energy difference between laser excitation and PL emission. The upper panel of Figure 5.14 shows the averaged normalized PLE resonances of five suspended CNTs as gray line. All CVD_{susp} CNTs exhibit the same PLE resonances characteristic for carbon-based systems with only minor tube-to-tube variations as evidenced by the small standard deviation (light gray area). In contrast, much larger variations are observed in the PLE resonances of CVD_{hBN} CNTs shown in the lower panel of Figure 5.14.[3] These variations are most likely caused by tube-to-tube variations in the dielectric environment, e.g. hBN crystal ridges and catalyst agglomerates as discussed in Chapter 6. The most pronounced deviations from the ensemble of suspended CNTs occurs in the energy range between 90 meV and 130 meV (shaded in blue). In this energy interval that coincides with the energy of the out-of-plane optical ZO phonon in hBN [115], all CVD_{hBN} CNTs exhibit a PLE resonance that is absent in the PLE of suspended CNTs. This is strong evidence for the coupling of CNT QDs to substrate phonons, enabling an observation of otherwise silent vibrational modes (as observed in 2D materials [116]). The strong PLE resonance at 50 meV laser detuning observed in Figure 5.13b was not within the measurement range of the other CNTs, however, it would fit the energy of an hBN ZA phonon at the M-point.

[3] The strong resonance around 230 meV was only present in one CNT.

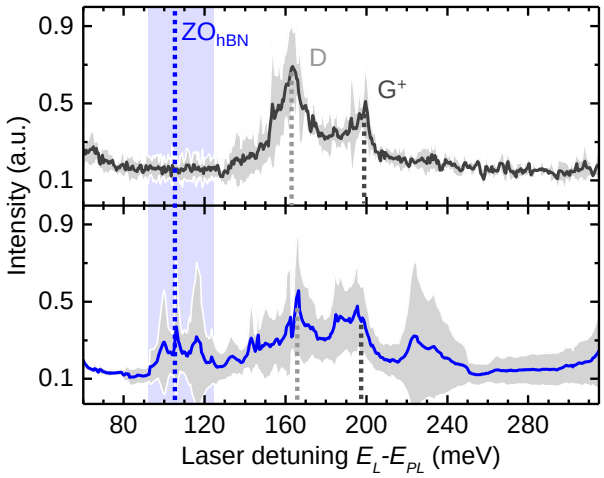

Figure 5.14: Averaged PLE resonances of five as-grown CNTs suspended over trenches (solid gray line, upper panel) and grown on hBN (solid blue line, lower panel). The light gray areas mark the respective standard deviations. The energies of the defect mode D and the G^+ band are indicated by light and dark gray dotted lines, respectively. Within the energy interval shaded in blue, a large discrepancy between CNTs suspended over trenches and grown on hBN was found. It coincides with the energy of the hBN out-of-plane optical ZO_{hBN} phonon (blue dotted line).

5.6 Conclusion

At the beginning of this chapter, the PLE characteristics of PL from delocalized excitons in a (6,5) CNT were presented. The as-grown CNT was suspended over a trench in an inert helium atmosphere to minimize disorder and environmental influences. The corresponding PLE resonances were governed by CNT phonons and strong Raman scattering was observed on resonance accounting for 80 % of the detected signal. Pristine CNTs that were deposited on a fused silica SIL from aqueous suspension showed the same PLE characteristics which enabled the precise mapping of the CNT phonon modes over an energy range from 40 meV up to 400 meV with a resolution of ±1.5 meV. Whereas a strong dependence of the CNT acoustic phonons on the chiral angle was found by comparing (6,5) and (9,1) chiralities, there was no indication of an influence of the dielectric environment. A comparison of (9,1) CNTs filled with water or alkane molecules combined with DOC or DNA surfactant, did not show any significant differences in the PLE characteristics or phonon energies. However, CNTs wrapped in DNA exhibited an increased occurence of low-energy side peaks with different PLE signatures.

Detailed PLE spectroscopy of defect-related states was performed on solution-processed alkyl-doped (6,5) CNTs coated with DOC. Defect-brightened intrinsic CNT excitons showed the same PL and PLE characteristics as observed in undoped samples. Defect-localized excitons, on the other hand, were characterized by an absence of Raman scattering and an overlap of PLE resonances at the CNT phonon energies with resonances inherited from high-energy states by non-radiative relaxation of excitons.

This resulted in broadened PLE resonances of defect localized excitons that were shifted to higher laser-detunings as compared to pristine CNTs. All observed PLE features were related to a combination of delocalized exciton states and defect-induced localized trap states. For the latter, the absence of Raman scattering was attributed to the small number of carbon atoms that had an overlap with the localized exciton wavefunction.

The special case of PL with resolution-limited spectral linewidth, observed for most as-grown CNTs suspended over trenches and on hBN substrates, did not fit into the scheme discussed above. The PL of these CNTs was enhanced at the energy of the carbon-related D- and G-mode phonons but not at CNT-specific resonances. In contrast to all other CNTs studied in this chapter, the PLE characteristics of these CNT QDs were strongly influenced by the dielectric environment. As-grown CNTs on hBN exhibited strong PLE resonances at the energy of the hBN-specific ZO and ZA phonons at the Γ and the M point, respectively, that were absent for suspended CNT QDs.

Chapter 6

Spectral dynamics of carbon nanotube photoluminescence

This chapter presents studies of the spectral photoluminescence dynamics of cryogenic carbon nanotubes. A strongly suppressed spectral diffusion of the photoluminescence from as-grown carbon nanotubes on hexagonal boron nitride was observed as compared to silicon oxide substrates. Substrate-specific differences in the spectral noise characteristics were successfully modeled in the framework of dipole-dipole interactions of the permanent electric dipole moment of a localized nanotube exciton with nearby surface charges. The results allowed to relate spectral noise characteristics to substrate topography. Surfactant-coated nanotubes that were applied to a solid immersion lens by drop-casting from aqueous solution, exhibited spectral fluctuations of similar magnitude as nanotubes grown on silicon oxide, but the corresponding spectral noise characteristics could not be modeled in the framework of dipole interactions of a localized exciton with external electric fields.

PARTS OF THIS CHAPTER ARE BASED ON THE PUBLICATION
Jonathan C. Noé, Manuel Nutz, Jonathan Reschauer, Nicolas Morell, Ioannis Tsioutsios, Antoine Reserbat-Plantey, Kenji Watanabe, Takashi Taniguchi, Adrian Bachtold and Alexander Högele. Environmental electrometry with luminescent carbon nanotubes. *Nano Letters* **18**, 4136-4140 (2018).

6.1 Introduction

Individual carbon nanotubes (CNT) report changes in electric field via spectral shifts in their photoluminescence (PL) energy. A dynamically fluctuating charge environment results in spectral fluctuations in the course of time which are particularly pronounced for localized excitons exhibiting finite electric dipole moments [41, 117] as a consequence of localization at unintentional disorder [33] or at side-wall defects in chemically functionalized nanotubes [34, 36, 37, 45]. Consistently, spectral fluctuations are suppressed for excitons in suspended nanotubes [30, 31]. Electrostatically passive environments of polymers yield similar trends [29].

In this chapter, the sensitivity of CNT exciton PL to variations in local electric fields was used to study the dynamics of charge fluctuations in silicon oxide (SiO_2) and hexagonal boron nitride (hBN) supports. While SiO_2 is a standard material in industrial integrated circuitry and is commonly used as dielectric support for prototype devices based on novel materials, the practicability of silicon platforms is challenged by the limitations in device performance due to fluctuating charge impurities inherent to SiO_2. These are known to reduce the intrinsic charge carrier mobility in graphene [13, 118], to cause hysteretic effects in CNT transistors [119–121], and to limit the sensitivity of nanotube-based bio-molecular sensors [122, 123]. Recent transport studies of graphene [124–126] and CNTs [77] on hBN, on the other hand, indicate that such detrimental effects are reduced on atomically flat hBN supports. More recent optical studies of two-dimensional semiconductors have confirmed the beneficial impact of hBN environments by reporting spectral linewidths at the limit of homogeneous broadening in best samples with two-sided hBN encapsulation [127–130].

6.2 Experimental methods

To characterize the spectral fluctuations of CNT PL and their relation to the properties of the immediate environment, PL spectroscopy was performed on CNT samples obtained by chemical vapor deposition (CVD) growth on various substrates or by drop-casting solution-processed CNTs coated with surfactant and filled with various molecules onto a fused silica solid immersion lens (SIL). The studied samples are listed in Table 6.1 and described in more detail in Section 3.2. The measurements were performed at 4.2 K using the confocal microscope described in Section 3.1. A scanning probe microscope was used for simultaneous imaging by Kelvin-probe force microscopy (KPFM) and atomic force microscopy (AFM).[1]

[1] *Bruker* Dimension Edge

Abbrevation	material	chirality	substrate	surfactant	filling
CVD_{SiO_2}	as-grown	$[d]_m \leq 1$ nm	SiO_2	/	empty
CVD_{hBN}	as-grown	$[d]_m \leq 1$ nm	hBN	/	empty
CVD_{susp}	as-grown	$[d]_m \leq 1$ nm	suspended	/	empty
DOC_{H_2O}	solution	(9,1)	SIL	DOC	H_2O
DOC_{org}	solution	(9,1)	SIL	DOC	$C_{20}H_{42}$
DNA_{org}	solution	(9,1)	SIL	DNA	$C_{24}H_{50}$

Table 6.1: Summary of the studied CNT materials. Row 2-4: The abbreviation CVD labels as-grown CNTs with the median of the diameter distribution $[d]_m \leq 1$ nm. The index denotes the substrates silicon oxide (SiO_2), hexagonal boron nitride (hBN), and suspended CNTs. Row 5-7: CNTs applied to a solid immersion lens (SIL) by drop-casting from aqueous solution are labeled according to the surfactants sodium deoxycholate (DOC) and DNA. The index refers to the filling with water or organic molecules.

6.3 Spectral dynamics of as-grown carbon nanotubes on SiO_2 and hBN

Figure 6.1 compares the spectral linewidths of CNTs on hBN to CNTs on SiO_2 for different integration times. In contrast to the spectrally narrow PL observed at lowest integration times of 1 s both on hBN and SiO_2, a large fraction of nanotubes on SiO_2 developed highly asymmetric spectra with significant spectral broadening at increased integration times evidenced by a comparison of the spectra with 1 s and 10 s integration times in Figure 6.1a. This time-accumulated PL line broadening was also observed at the statistical level for different CNTs on hBN and SiO_2: the histogram of Figure 6.1b with a full-width at half-maximum (FWHM) binning of 0.5 meV shows that the PL linewidth of nanotubes on hBN (blue columns) was independent of the integration time, while the spectra of most nanotubes on SiO_2 exhibited a progressively increasing spectral broadening with prolonged integration times.

6.3.1 Spectral stability

To examine this pronounced difference in the temporal evolutions of the PL from CNTs on hBN and SiO_2 in more detail, the PL was sampled with 1 s integration time over the course of 1000 s yielding the color-coded PL evolutions shown in Figure 6.2a. The temporal characteristics of individual CNTs in the upper and lower panels of Figure 6.2a are representative for substrate-specific responses observed on SiO_2 and hBN, respectively, with frequent spectral fluctuations on a meV scale for tubes on SiO_2 contrasted by CNTs on hBN with stable PL emission. A quantitative analysis of this effect was performed using the Allan deviation s_e as a measure for the spectral stability of a resonance [131, 132]:

$$s_e = \sqrt{\frac{1}{2} \cdot \frac{1}{N-1} \cdot \sum_{n=1}^{N-1} (e_n - e_{n+1})^2}, \tag{6.1}$$

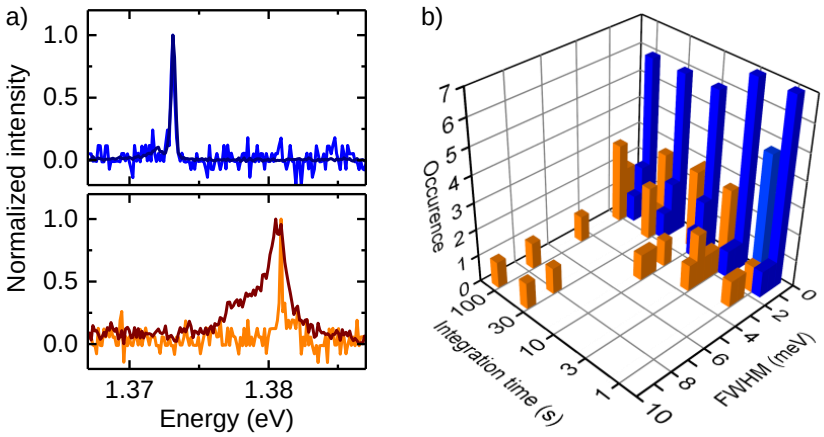

Figure 6.1: a) Low-temperature PL spectra of CNTs on hBN (top panel) and SiO_2 (bottom panel) at 5 W/mm^2 excitation power. Blue (orange) and dark blue (wine) spectra were recorded with 1 s and 10 s integration times, respectively. b) Histogram of the full-width at half-maximum spectral line widths of CNT PL spectra on SiO_2 (orange) and hBN (blue) as a function of the integration time.

where e_n is the PL peak energy of the n-th consecutive spectrum out of the total number of N spectra. Analogous to the standard deviation, the Allan deviation quantifies the magnitude of spectral fluctuations. In contrast to the standard deviation, however, its time evolution does not depend on the exponent α for spectral fluctuations characterized by a power law $1/f^{\alpha}$ [131] and was therefore used to analyze the PL fluctuations of the CNTs in this study exhibiting varying α in their noise spectral density.

For the two specific CNTs on SiO_2 and hBN of Figure 6.2a, the Allan deviation was calculated in steps of 50 s as displayed in Figure 6.2b (orange and blue data correspond to the CNT on SiO_2 and hBN, respectively) and was found to differ by more than one order of magnitude on all time scales of the experiment. Figure 6.2c shows the Allan deviation of 19 different CNTs on SiO_2 and hBN as a function of the excitation laser power as orange and blue data, respectively. The graph divides the tubes on hBN and SiO_2 into two disparate classes, with a few exceptions of CNTs on hBN exhibiting spectral fluctuations as large as most of the CNTs on SiO_2. The large spread in the data shows no obvious trend for the functional dependence of the PL stability on the excitation power for CNTs on hBN, while the spectral fluctuations seem to increase for tubes on SiO_2 with higher excitation powers in accord with power-induced spectral wandering [133]. These observations suggest that spectral fluctuations are sensitive to the specifics of the dielectric support, and that the charge noise in the PL of nanotubes on hBN is strongly inhibited.

In Figure 6.2d, the findings from Figure 6.2c are compared to as-grown CNTs suspended over trenches. Contrary to what one would expect, completely suspended CNTs exhibit higher Allan deviations than those located at the edge of a trench (gray and black data points, respectively). The latter show Allan deviations near or below the spectral resolution (CNTs with $s_e = 0$, were discarded from the analysis). Spectral fluctuations in the PL from completely suspended CNTs form two separate classes with Allan devia-

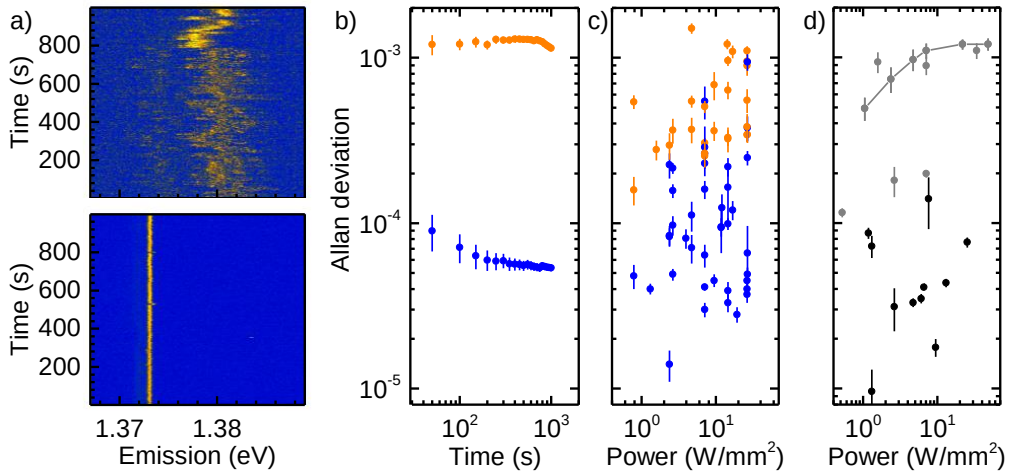

Figure 6.2: a) Temporal evolution of the PL of a representative CNT on SiO_2 (top) and on hBN (bottom) at 5 W/mm^2 excitation power. b) Corresponding temporal evolutions of the Allan deviation. c) Allan deviations for CNTs on SiO_2 (orange) and hBN (blue) calculated from sets of 100 consecutive spectra with 1 s integration time per spectrum. d) Allan deviations of CNTs suspended over and near the edge of a trench (gray and black data points, respectively). The data points connected by the gray line belong to the same CNT.

tions above and below $3 \cdot 10^{-4}$. The solid line connects data points from the same CNT. In both cases, the Allan deviation increased with the excitation power and especially for the CNTs with higher Allan deviations a saturation effect was observed. In the absence of external influences, the most likely cause for the observed spectral PL fluctuations are local electric fields created for example by the dissociation of photo-excited excitons [134, 135] that was reported to be very efficient for suspended CNTs [22, 136]. It should be noted, however, that the Allan deviation saturates at lower excitation powers than the PL intensity (not shown here). No saturation of the Allan deviation was found for CNTs in contact with a substrate. This could be due to more efficient thermalization and decay of photoexcited charges. A possible explanation for the different magnitudes of the spectral PL fluctuations among CVD_{susp} CNTs are different types of localizations sites with different permanent electric dipole moments rendering the CNT excitons more or less susceptible to charge fluctuations. However, PL emission from suspended CNTs with small and large spectral fluctuations did not differ with respect to the emission energies and showed the same signatures in photoluminescence excitation spectroscopy.

6.3.2 Noise spectral density

A detailed analysis of the noise characteristics that govern the PL fluctuation dynamics was performed to clarify the origin of large spectral wandering of the PL for those tubes on hBN that exhibited Allan deviation values comparable to CNTs on SiO_2 in Figure 6.2c. Within the framework of spectral noise analysis, the time evolution of the PL energy $\hbar\omega_0(t)$ was characterized by the noise spectral density $S(f)$. For a measurement series of

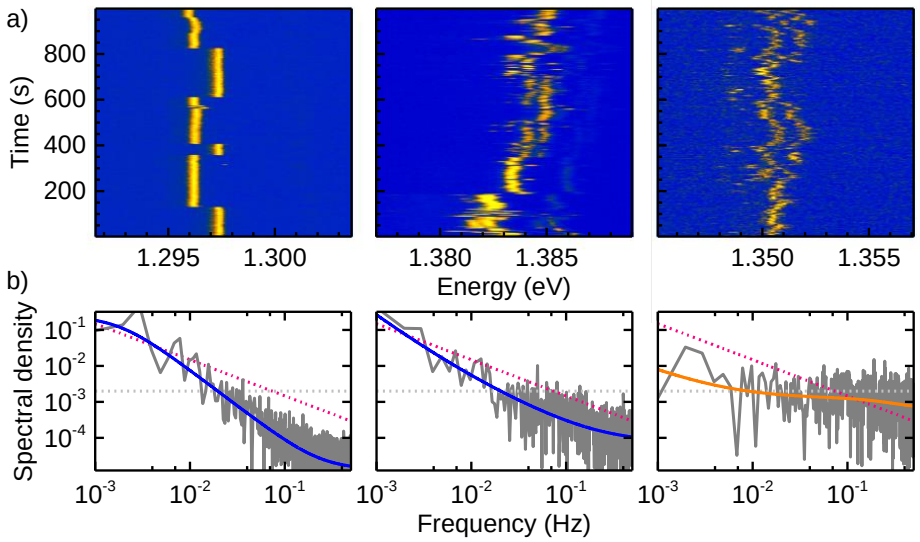

Figure 6.3: a) Temporal evolution of CNT PL representing the cases of a large random telegraph, $1/f$, and white noise component (from left to right) in their spectral fluctuations at 4.2 K. b) Respective normalized noise spectral densities and model decompositions (solid lines, orange and blue colors represent nanotubes on SiO_2 and hBN, respectively) into random telegraph, $1/f$, and white noise according to Eq. 1. The pink and gray dashed lines indicate the limits of pure $1/f$ and white noise, respectively.

time $T = 1000$ s with a time binning of $t_{\mathrm{bin}} = 1$ s, $S(f)$ was obtained within a bandwidth ranging from $1/T$ to $1/(2t_{\mathrm{bin}})$ for discrete frequencies $f = k/T$ (with integer number k and $k_{\mathrm{max}} = T/2t_{\mathrm{bin}}$) from the ratio of $\omega_0(t)$ and its time average $\langle\omega_0(t)\rangle$ by fast Fourier transform (FFT) [137]:

$$S(f) = |\mathrm{FFT}[\omega_0(t)/\langle\omega_0(t)\rangle]|^2 (t_{\mathrm{bin}})^2/T, \tag{6.2}$$

and normalized such that the total noise spectral density equaled unity:

$$\sum_{k=1}^{k_{\mathrm{max}}} S(k/T) = 1\ \mathrm{Hz}^{-1}. \tag{6.3}$$

In solid state systems, $S(f)$ is commonly modeled by a general power law $1/f^{\alpha}$ with a system-specific exponent α in the range $0.5-1.5$ [137–140], and $\alpha = 1$ being the limit of pure $1/f$-noise or pink noise [141]. For a more intuitive interpretation of the spectral fluctuations in the nanotube PL due to switching events of individual charge traps in the dielectric support, the noise spectral density was decomposed into contributions of random telegraph noise $S_t(f)$, pink noise $S_p(f)$ and frequency-independent white noise S_w as:

$$S(f) = a \cdot S_t(f) + b \cdot S_p(f) + c \cdot S_w, \tag{6.4}$$

with the respective relative weights a, b and c ranging between 0 and 1, and $a+b+c = 1$.

The first term quantifies the fraction of random telegraph noise (RTN) arising from a fluctuating charge trap in close CNT proximity. Its Lorentzian noise spectral density is

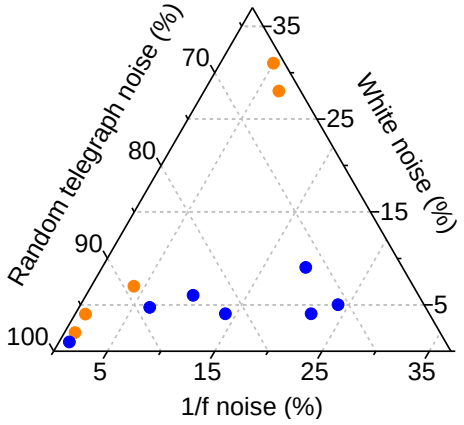

Figure 6.4: Relative weight of noise contributions in the spectral fluctuations in the PL of as-grown CNTs on SiO_2 and hBN (orange and blue data, respectively) calculated from 1000 consecutively measured 1 s spectra.

given by:

$$S_t(f) = n\frac{2(\Delta E)^2\bar{\tau}}{4+(2\pi f\bar{\tau})^2} \quad , \tag{6.5}$$

where ΔE is the energy difference between the two binary states of the CNT PL energy that correspond to a charged and a discharged trap state with a characteristic average switching time $\bar{\tau}$. The proportionality constant n follows from the normalization of $S_t(f)$ according to Eq. 6.3 with $a = 1$. The second term corresponds to the pink noise component $S_p(f) = p/f$ with a proportionality factor $p = 1.47 \cdot 10^{-4}$ obtained from normalization of $S_p(f)$ according to Eq. 6.3 with $b = 1$, and the third term represents the white noise component with $S_w = 2 \cdot 10^{-3}$ Hz^{-1} obtained from Eq. 6.3 with $c = 1$. The CNT on hBN with the PL evolution and noise spectral density in the left panels of Figure 6.3a and b, respectively, was representative for the case where one dominant charge fluctuator caused discrete jumps between two distinct PL energies resulting in nearly pure RTN (the solid line in the left panel of Figure 6.3b shows the decomposition into noise components according to Eq. 1 with $a = 0.99$, $b = 0.00$, and $c = 0.01$). The central panels of Figure 6.3a and b show a CNT on hBN with a large $1/f$-noise component ($a = 0.74$, $b = 0.21$, and $c = 0.05$), and the right panels of Figure 6.3a and b are representative for CNTs on SiO_2 with a large white noise contribution (with $a = 0.64$, $b = 0.05$, and $c = 0.31$ for this specific tube). While $1/f$-noise (pink dashed lines in Figure 6.3b) can be related to a superposition of multiple independent RTN sources [142], very rapid fluctuations with a broad distribution of random amplitudes result in frequency independent white noise (gray dashed lines in Figure 6.3b).

The decomposition of the noise spectral densities according to Equation 6.4 was performed for all CNTs of our study with PL time series recorded with a minimum of 1000 spectra at 1 s integration time. The resulting distribution of noise compositions are summarized in the ternary plot of Figure 6.4 (blue and orange data correspond to CNTs on hBN and SiO_2, respectively). Carbon nanotubes with vanishingly small spectral wandering were discarded from the analysis and are therefore not represented in the

graph. For all other nanotubes, $S(f)$ was found to be dominated by the RTN component (note the different scale of the ternary diagram in Figure 6.4) because of the dominant impact of the near-most charge fluctuator. Remarkably, the noise signatures of CNTs on hBN and SiO_2 again separated into two distinct classes: while nanotubes on hBN formed a class with a varying $1/f$ noise contribution and a low white noise weight (< 10 %), the case of nanotubes on SiO_2 was just the opposite. To further investigate the origin of this discrepancy, Monte Carlo simulations of CNTs on substrates with different dielectric properties were employed.

6.3.3 Monte Carlo simulations

Spectral fluctuations in the CNT PL were modeled by simulations based on the electrostatic interactions between the permanent electric dipole moment of a localized CNT exciton and fluctuating charge traps on the surface of the underlying substrate (Figure 6.5a). The localized exciton with a permanent dipole moment $\mathbf{p}$ (indicated by the light blue arrow) was placed at the origin of the coordinate system at the apex of the CNT with diameter d_{CNT} residing in vacuum on a substrate with the dielectric constant ϵ_r. The charge trap was modeled by an electron with the elementary charge $-e$ on the substrate surface and the corresponding mirror charge e within the substrate at distance vectors $\mathbf{r}$ and $\mathbf{r}_m$ (along the corresponding unit vectors $\hat{\mathbf{r}}$ and $\hat{\mathbf{r}}_m$) from the CNT exciton dipole, respectively. The dipolar field of the charge trap (gray lines) induces a shift in the PL energy of the localized exciton via the first-order Stark effect according to:

$$\Delta E_{\mathrm{PL}} = \frac{-e}{4\pi\epsilon_0}\mathbf{p}\cdot\left(\frac{\hat{\mathbf{r}}}{|\mathbf{r}|^2} - \frac{1-\epsilon_r}{1+\epsilon_r}\cdot\frac{\hat{\mathbf{r}}_m}{|\mathbf{r}_m|^2}\right) \tag{6.6}$$

with the vacuum permittivity ϵ_0. A diameter $d_{\mathrm{CNT}} = 0.7$ nm was used as a typical value for the CNTs in this study and $\mathbf{p} = (0.35, 0, 0.27)$ eÅ [41] as an estimate of the electric dipole moment of excitons localized by unintentional disorder in cryogenic CNTs. Different orientation, position and magnitude of the exciton dipole moment did not change the qualitative results of the simulations. With this geometry, Monte Carlo simulations were used to determine the characteristic spectral power density of CNTs with temporal PL fluctuations arising from charging and discharging events in the nearby traps. To this end, as shown schematically in Figure 6.5b, N trap states (gray crosses, 0.1 Å above the dielectric substrate) with a surface density σ and a characteristic trapping and release time τ were considered in a random distribution around the CNT within a circle of radius r_{max} which provided a cut-off to the simulations by defining a maximum sensitivity distance to a single trap. At r_{max} (with different values of 37 nm and 44 nm for charge traps on hBN and SiO_2, respectively, due to different dielectric constants), the field amplitude of a charge dipole decayed to $1/e^2$ of the value that would result in a PL energy shift equal to the spectral resolution limit of the spectrometer (~ 0.1 meV). Where required, an exclusion circle with a finite radius r_{min} was used to impose an area free of charge traps around the CNT.

For each simulation run, N trap states were distributed randomly within r_{max} with a

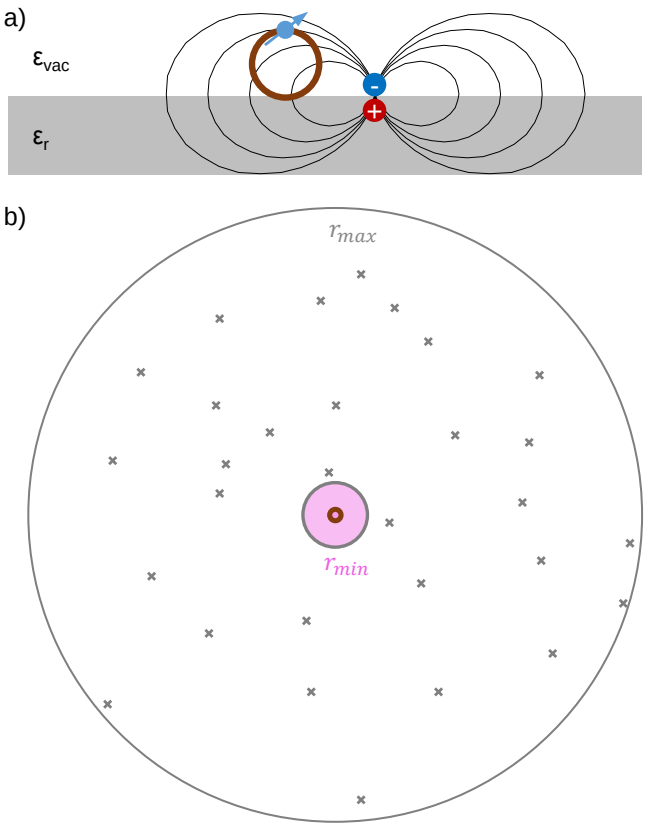

Figure 6.5: a) Model schematics: The localized exciton with a permanent dipole moment **p** (blue arrow) resides in vacuum at the apex of the CNT on a substrate with the dielectric constant ϵ_r. A nearby charge trap is modeled by an electron that creates along with its mirror charge a dipolar field at the location of the exciton thus giving rise to a spectral shift in the exciton PL. b) Model parameters: N trap states (gray crosses) with a surface density σ and an average lifetime τ are distributed randomly in a circle (gray) with radius r_{max} around the nanotube. A region free of charge traps around the CNT can be ensured by an exclusion circle (pink shaded area) with radius r_{min}.

subsequent removal of traps inside of r_{min}. The initial state of every trap (either occupied by an electron or empty) was chosen randomly. The capture and release of electrons on the characteristic time scale τ led to a time-dependent effective electric field at the position of the CNT which in turn gave rise to spectral shifts of the exciton PL peak frequency ω_0. The time evolution $\omega_0(t)$ with a frequency resolution determined by the spectrometer was sampled 1000 times with a time bin $t_{\mathrm{bin}} = 1$ s (corresponding to a rate $1/t_{\mathrm{bin}}$ of 1 Hz), resulting in a total temporal evolution time $T = 1000$ s.

The simulations were performed 100 times for each set of parameters and the resulting time evolutions of $\omega_0(t)$ were analyzed with respect to their noise spectral densities as described in the previous section. The $1/r^2$ dependence of the dipole field resulted in a strong RTN contribution for all parameter sets (note the different scales of the ternary diagrams in Figure 6.6 and Figure 6.7) because the nearest trap state has a dominant influence. The dependence of the simulation results on the parameters σ, τ, and r_{min} is shown in Figure 6.6. The parameter sets in Figure 6.6a resulted in RTN-dominated

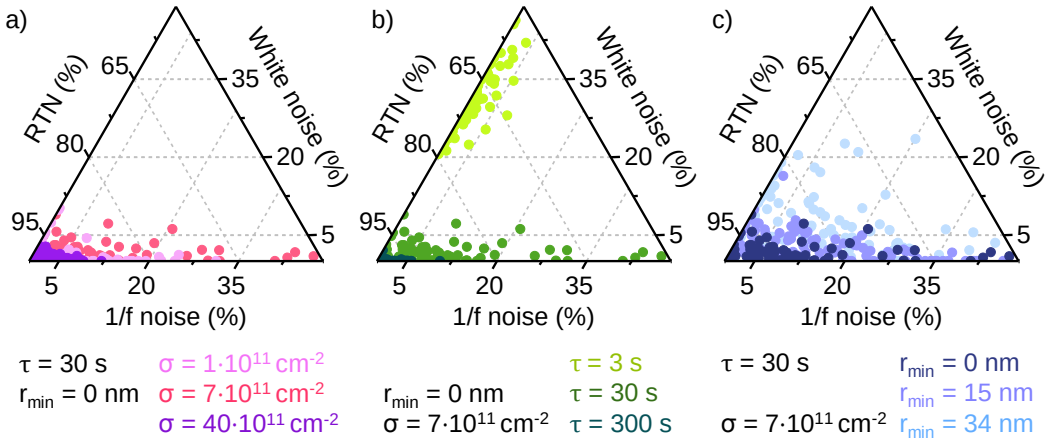

Figure 6.6: Simulation results depending on the three input parameters: density of surface trap states σ, their corresponding lifetime τ and minimum distance from the CNT r_{min} (a, b, and c, respectively). All parameter sets yield spectral fluctuations dominated by random telegraph noise (RTN) with a small 1/f noise contribution. a) Variations in σ change the spread in the data. b) White, 1/f, and RTN noise are related to short, intermediate, and long switching times, respectively. c) An increasing area without surface charge traps around the CNT leads to a decrease in the RTN component. The relative dielectric constant was set to the value of hBN $\epsilon_r = 6$.

spectral fluctuations with a significant pink noise component. An increased surface state density σ led to a larger spread in the simulation results and a overall decrease of the RTN component (pink data). This effect was reversed and overcompensated for even higher trap state densities (purple data). A very low density of trap states favors spectral fluctuation dominated by RTN. However, due to the $1/r^2$ dependence of the dipole-dipole interaction, this also holds for very large trap state densities, because the probability to find a dominant trap state close to the CNT increases with σ. This explains the scaling of the RTN component with σ observed in Figure 6.6a. The strong effect of the switching time τ on the spectral dynamics is shown in Figure 6.6b. Slow switching rates resulted in almost pure RTN (olive data). Intermediate (green) and short (light green) switching times, on the other hand, generated spectral fluctuations with a strong 1/f and white noise component, respectively. An area of radius r_{min} free of charge traps around the CNT yielded large 1/f noise components with a significant white noise contribution that both increased with r_{min} (dark blue to light blue data in Figure 6.6c).

The simulation results of the parameter sets that reproduced the experimental data best are shown in Figure 6.7. Simulations of a rather stable dielectric environment characterized by a surface state density of $\sigma = 1 \cdot 10^{11}$ cm^{-2} (an order of magnitude lower than in SiO_2) and long characteristic dwell times of charge states ($\tau > 100$ s) capture the limit of a single fluctuating charge by the black data points in Figure 6.7a. This limit was contrasted by using the parameters expected for SiO_2 (light gray data points in Figure 6.7 b) with $\sigma = 1 \cdot 10^{12}$ cm^{-2} [143] and typical fluctuation timescales of $\tau \leq 3$ s. The large white noise component was introduced by switching rates near and below the resolution limit of the FFT of 0.5 Hz given by $0.5/t_{\text{bin}}$. The occurrence of $1/f$

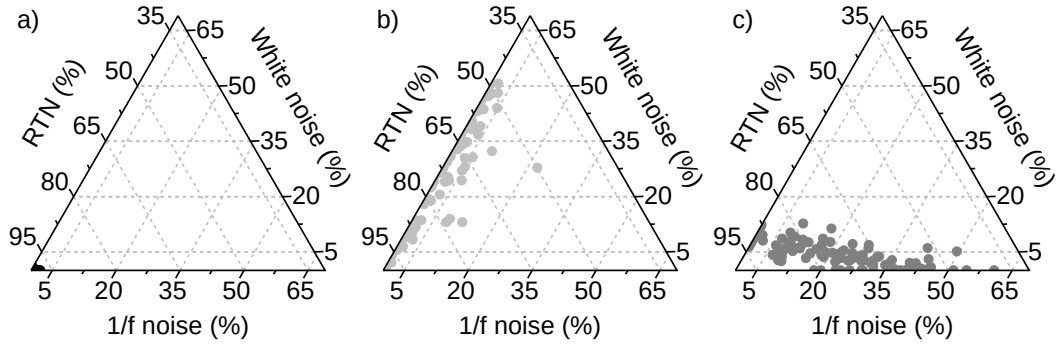

Figure 6.7: Simulation results based on the set of parameters that provided the best agreement with the experimental data (density of surface trap states σ, their corresponding lifetime τ and their minimum distance from the CNT r_{min}). a) Substrate with low spatial density of slowly fluctuating charge traps: $\sigma = 1 \cdot 10^{11}$ cm^{-2}, $\tau > 100$ s, $r_{\mathrm{min}} = 0$ nm; all data points are concentrated at the lower left corner of the ternary diagram and are therefore barely distinguishable. b) Parameters characteristic of SiO_2 representing the scenario of a high density of fast fluctuating surface states: $\sigma = 1 \cdot 10^{12}$ cm^{-2}, $\tau \leq 3$ s, $r_{\mathrm{min}} = 0$ nm. c) A distant accumulation of charge fluctuators with high areal density: $\sigma = 1 \cdot 10^{13}$ cm^{-2}, $20\ \mathrm{s} < \tau < 60$ s, $r_{\mathrm{min}} = 34$ nm. The simulations used $\epsilon_r = 6$ for hBN and $\epsilon_r = 3.9$ for SiO_2 (a, c and b, respectively).

noise was found to be related to distant accumulations of charge traps in an otherwise stable dielectric environment (dark gray data points in Figure 6.7 c) with r_{min} of at least 30 nm, intermediate fluctuation times $20\ \mathrm{s} < \tau < 60$ s, and a high surface state density $\sigma = 1 \cdot 10^{13}$ cm^{-2}.

6.3.4 Relation between 1/f noise and substrate topography

The simulation results from Figure 6.7 and the experimental data from Figure 6.4 are compared in Figure 6.8b. The stable dielectric environment simulated in Figure 6.7a with a low density of charge states and minute-long characteristic dwell times (black data points concentrated in the lower left corner of the ternary diagram in Figure 6.8b) reproduced the noise composition of the CNT in in the left panel of Figure 6.3a and b. Using the fluctuator areal density of $\sigma = 1 \cdot 10^{-12}$ cm^{-2} as characteristic for SiO_2 [143], the simulation results (light gray data) were in good agreement with the experimental data (orange) if typical fluctuation timescales in the range of $1 - 3$ s were assumed in accord with the actual observation of switching events as in the upper and right panels of Figure 6.2a and Figure 6.3a, respectively.

A region free of charge traps around the CNT exciton dipole produced the noise class of nanotubes on hBN with a sizable $1/f$-noise component. This limit (dark gray data in Figure 6.8b) was reproduced for distant ($r > 30$ nm) accumulations of charge traps with intermediate fluctuation times of ~ 30 s and a factor of 10 higher spatial densities than on SiO_2. It reflects the case of an electrostatically calm substrate with a low charge trap density paired with distant chains of surface states. One possible realization of such a scenario is a CNT located close to a ridge of an extended atomically flat hBN terrace.

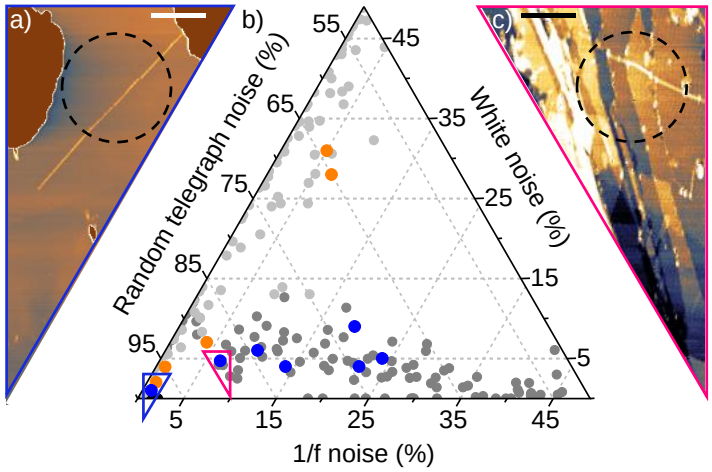

Figure 6.8: a) and c) Atomic force micrographs of CNTs on flat and rocky regions of an hBN flake (blue and pink triangles, respectively, also used to indicate the corresponding noise compositions in b). The dashed circles mark the optical spot with ~1 µm diameter, the scale bars are 500 nm. b) Noise composition of CNTs on hBN (blue data points) and on SiO_2 (orange data points) as in Figure 6.4. The gray data are the simulation results from Figure 6.7 connecting the measurements to physical substrate properties. They represent the expected distribution of fluctuating charge traps on SiO_2 (light gray) contrasted by the scenario of an electrostatically calm substrate with and without accumulation of distant surface states (black and gray, respectively; the black data points are concentrated at the lower left corner of the ternary diagram and are therefore barely distinguishable).

At terrace ridges, both dangling bonds and accumulation of CVD catalyst particles can give rise to a collection of charge-state fluctuators with a high spatial density. In fact, *a posteriori* inspection of luminescent CNTs with AFM has identified nanotubes in rocky regions of hBN flakes (Figure 6.8c) with the tendency to exhibit a higher $1/f$ noise component than tubes on extended terraces residing sufficiently far away form charge-fluctuating lines of disorder and thus exhibiting predominantly RTN in their spectral jitter (Figure 6.8a).

This assumption was supported by complementary AFM and KPFM studies of local environments of CNTs on an hBN flake. Both AFM and KPFM imaging of a representative hBN flake of the sample (Figure 6.9a, c, e, and f) revealed catalyst particles distributed randomly over hBN terraces as well as dense lines of particles agglomerated in chains along the crystal ridges. The ~0.4 nm steps in the height profile in Figure 6.9c correspond to a change in height of a single hBN layer. The height profile in Figure 6.9d shows sub-nanometer diameter CNTs on atomically flat hBN terraces. Their vicinity to chains of disorder visible as the lines of high contrast in Figure 6.9a, b, e, and f, visualize the scenario of CNTs with an increased 1/f noise component in the noise spectral density of the PL dynamics. The next section compares the data obtained on as-grown CNTs to the spectral fluctuations of the PL from surfactant-coated (9,1) CNTs listed in Table 6.1.

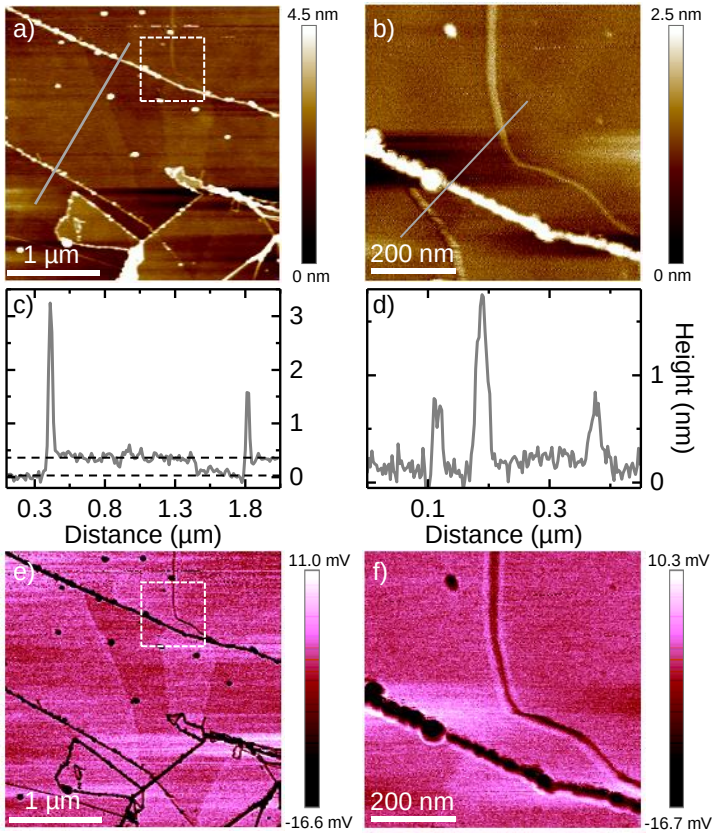

Figure 6.9: Atomic force micrographs (a, b) and corresponding Kelvin probe force profiles (e, f) of a representative sample region with nanotubes on an hBN flake. Zooms to the regions indicated by the white squares in (a) and (e) are shown in (b) and (f). c) and d) Height profiles along the gray lines in (a) and (b), respectively. Data in (a), (c) and (e) identify atomically flat crystal terraces with randomly distributed catalyst particles as well as particle agglomerates along terrace ridges. Data in (b), (d) and (f) show two CNTs with sub-nanometer diameters in the vicinity of a terrace ridge with a chain of disorder (the lower nanotube is missing in the corresponding Kelvin probe force measurement).

6.4 Effects of carbon nanotube surfactant and filling on the spectral dynamics

Figure 6.10a-c shows the Allan deviations of DOC_{H_2O}, DOC_{org}, and DNA_{org} CNT PL fluctuations as a function of the excitation power (dark blue, brown, and olive data points, respectively). Similar to Section 6.3.1, Allan deviations were calculated from 100 consecutive spectra with 1 s integration time per spectrum. The as-grown CNTs on SiO_2 in Figure 6.10 were chosen as reference material because of the similar dielectric properties of SiO_2 and the fused silica SIL. The Allan deviations of the DOC-coated CNTs in Figure 6.10a and b were slightly smaller compared CNTs wrapped in DNA, for which spectral fluctuations increased for higher excitation powers (Figure 6.10c). Surprisingly the value of the Allan deviation was comparable to the CVD_{SiO_2} CNTs for most solution-processed CNTs from Table 6.1, despite the differences in the environ-

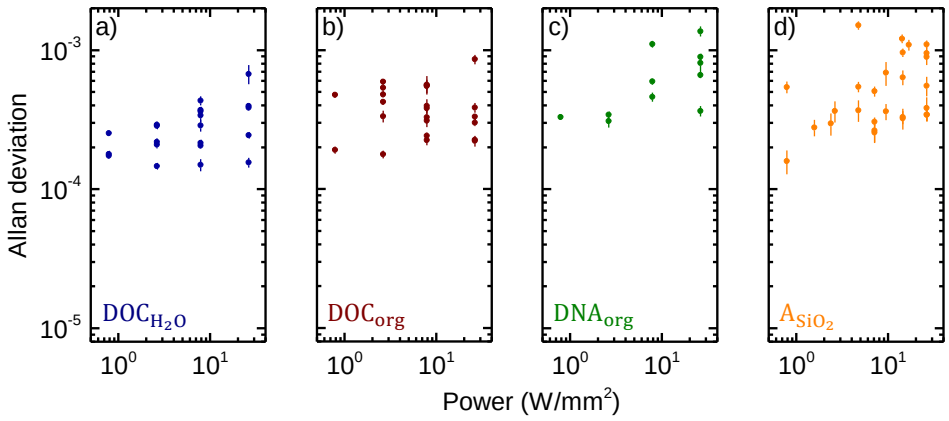

Figure 6.10: a)-c) Allan deviations of DOC_{H_2O}, DOC_{org}, and DNA_{org} CNTs, respectively, calculated from sets of 100 consecutive spectra with 1 s integration time per spectrum. d) The as-grown CNTs on SiO_2 shown in Figure 6.2c act as a reference.

mental conditions, the different PLE characteristics discussed in Chapter 5, and the fact that surfactant-coated CNTs were expected to show less spectral PL fluctuations due to a better screening from the substrate. A possible explanation is that the surfactant does not isolate the CNTs sufficiently from the substrate resulting in PL fluctuations that are not distinguishable from as-grown CNTs on SiO_2. Other possible scenarios are that spectral PL fluctuations were caused by the surfactant molecules or, in the case of delocalized excitons, by variations of the dielectric environment along the CNT.[2]

For a more detailed analysis, the noise spectral densities of all CNTs with time series of 1000 s were calculated and subsequently used to extract the corresponding noise contributions following the procedure presented in Section 6.3.2. The results are shown in Figure 6.11a-c and are compared to results obtained for as-grown CNTs on SiO_2 in d. The axes of all ternary diagrams cover the full range in contrast to Figure 6.4 and Figure 6.8. All surfactant-coated CNTs exhibited a much larger variety and smaller RTN contributions in their noise characteristics as compared to as-grown CNTs. Due to the large spread in the data and the small number of studied CNTs, it was not possible to assign noise characteristics to specific surfactants or CNT fillings. The large scatter in the noise contributions may be caused by the fact that Equation 6.4 did not capture all contributions that were present in the noise spectral density of DOC_{H_2O}, DOC_{org}, and DNA_{org} CNTs and therefore failed to extract the individual noise terms correctly. Furthermore, the noise weight distributions shown in Figure 6.11a-c, could not be modeled by the simulations presented in Section 6.3.3. Since the simulations were based on the scenario of localized excitons in as-grown CNTs, the spread in the data in Figure 6.11a-c may be related to the dominance of delocalized excitons in the surfactant-coated CNTs that was not considered in the model. To summarize, even though the magnitude of the spectral diffusion was comparable for as-grown and surfactant-coated CNTs, the microscopic processes responsible for the spectral wandering in solution-processed

[2] The results from PLE spectroscopy in Chapter 5 suggest that the PL of surfactant-coated (9,1) CNTs stems from delocalized excitons.

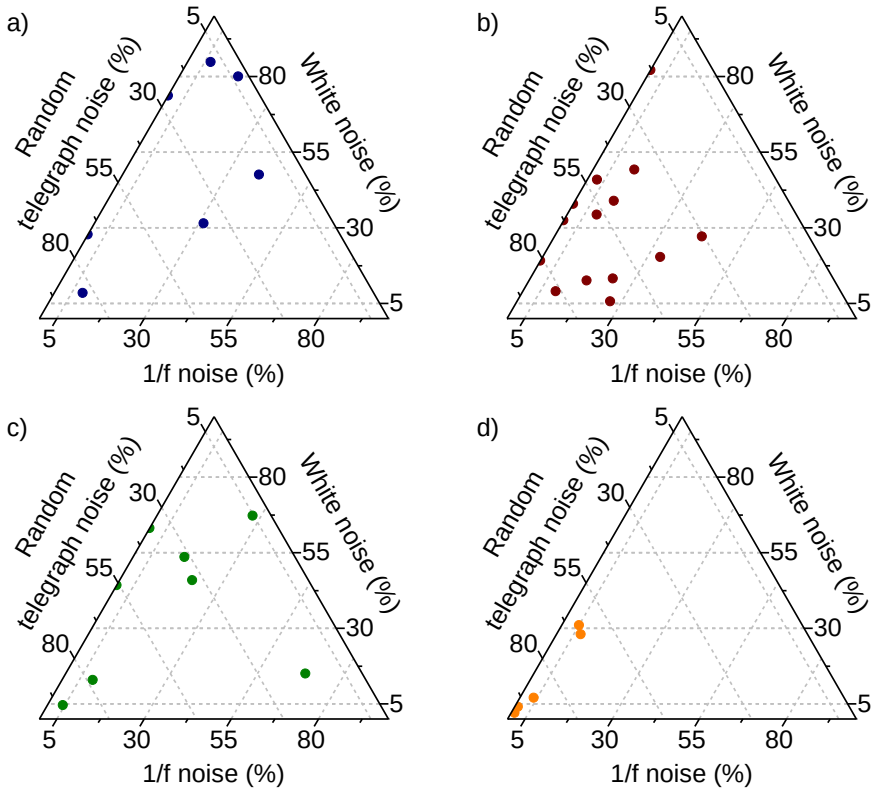

Figure 6.11: a)-c) Noise compositions of DOC_{H_2O}, DOC_{org}, and DNA_{org} CNT, respectively, calculated from sets of 1000 consecutive spectra with 1 s integration time per spectrum and $3-8\,W/mm^2$ excitation power. d) As-grown CNTs on SiO_2 from Figure 6.3c are shown as a reference.

nanotubes differ from those in as-grown CNTs on SiO_2.

6.5 Conclusion

In this chapter the influence of the dielectric environment on the spectral dynamics of as-grown and surfactant-wrapped cryogenic CNTs has been discussed. The effects of SiO_2 and hBN substrates on the spectral fluctuations of as-grown CNTs have been analyzed by using the Allan deviation as a measure for the magnitude of spectral diffusion. Most of the CNTs on hBN exhibited Allan deviation values comparable to CNTs suspended near the edge of a trench wich was an order of magnitude lower as compared to CNTs on SiO_2. A decomposition of the respective noise spectral density into RTN, $1/f$ noise and white noise revealed a significant white noise and $1/f$ noise component for as-grown CNTs on SiO_2 and hBN, respectively, with a dominating RTN contribution in all spectral noise densities. The experimental results were modeled by Monte Carlo simulations in the framework of dipole-dipole interactions of a localized CNT exciton with nearby randomly fluctuating surface charges. Via complementary PL and AFM measurements the spectral noise characteristics were related to substrate properties. Whereas RTN occurs on electrostatically passive substrates with low defect density,

which is the case for hBN plateaus, white noise was connected to the rapid charge fluctuations on SiO_2. The large 1/f noise component for some of the CNTs grown on hBN was attributed to a distant accumulation of fluctuating charges that was associated with crystal ridges of hBN, which was also confirmed by complementary AFM and KPFM measurements.

A comparison of as-grown CNTs on SiO_2 and surfactant-coated CNTs on a fused silica SIL showed a similar magnitude of the spectral PL fluctuations, but significant differences in the spectral noise composition. The results suggest a different microscopic mechanism behind the spectral fluctuations of solution-processed and as-grown CNTs, that is most likely related to an absence of exciton localization in surfactant-coated CNTs.

Chapter 7

Summary and outlook

Strongly bound electron-hole pairs (excitons) in semiconducting carbon nanotubes (CNT) have great potential in photonic and optoelectronic applications [8]. The discovery that cryogenic CNTs can act as single-photon source [28] together with major advances in the synthesis [73, 74, 144], sorting [44] and functionalization [34, 35, 37–40, 45, 46] of CNTs paved the way towards nanotube-based solid-state quantum photonics. However, especially at cryogenic temperatures, CNT photoluminescence (PL) is dominated by spectral wandering [25, 30, 42, 114, 145], blinking [43], and multipeak PL emission [35, 39, 46]. These disorder-induced perturbations are incompatible with the high demands on PL stability required for quantum photonic applications. To circumvent these limitations, a fundamental understanding of the interactions of excitons with the dielectric environment and their impact on the PL properties is required.

In the framework of this thesis, the energy distribution, the photoluminescence excitation (PLE) resonances, and the spectral dynamics of cryogenic CNTs were studied using a home-built confocal microscope. The focus of these studies was the impact that environmental factors, such as surfactant agents, substrates and the encapsulation of molecules inside the nanotube, have on the CNT PL characteristics. To this end, CNTs were grown on various substrates by chemical vapor deposition (CVD) and CNTs filled either with water or alkane molecules and coated with sodium deoxycholate (DOC) or DNA surfactants were applied to a solid immersion lens (SIL) by drop-casting from aqueous solution. All solution-processed CNT materials exhibited symmetric spectral lineshapes independent of their respective filling or surfactant as discussed in Chapter 4. Complementing the PL data of these CNTs with the corresponding E_{22} resonances, however, showed that the distribution of PL peak energies was influenced by the surfactant. Whereas tube-to-tube variations in strain of about 0.8 %, possibly mediated by dried-off DOC residuals, are most likely responsible for variations in the PL energy of DOC-coated CNTs, the PL energy distribution of DNA-wrapped nanotubes was broadened by the frequent occurrence of low-energy defect states. The optical transition energies at room temperature, measured by absorption spectroscopy on CNTs dispersed in solution, were related to the cryogenic PL data taking into account modifications of the dielectric environment, strain, and the phase transitions of water molecules confined inside a

nanotube during cool-down.

The PLE studies presented in Chapter 5, identified three different types of CNT PLE characteristics that were subsequently related to varying degrees of exciton localization. The PL associated with delocalized excitons exhibited PLE resonances at the characteristic CNT phonon energies. On resonance, the CNT PL signal was superimposed with resonant enhanced Raman scattered photons, that accounted for over 80 % of the detected signal. These PLE characteristics were observed for surfactant-coated and also for several suspended as-grown CNTs. The corresponding PL always exhibited a symmetric PL spectral lineshape with a full-width at half-maximum (FWHM) spectral linewidth of $2-5$ meV. The pronounced resonances allowed to determine the energy of all relevant acoustic and optical phonons of CNTs with (9,1) and (6,5) chirality that were, as expected, independent of substrate, surfactant, and CNT filling. Photoluminescence from defect-localized states was not accompanied by enhanced Raman scattering and exhibited several resonances in addition to the ones related to CNT phonons. The absence of Raman scattering was explained by the reduced number of carbon atoms that contribute to the scattering event due to the localization of the exciton in the CNT lattice. The additional PLE resonances were attributed to non-radiative exciton relaxation from states with higher energy. These PLE characteristics were observed for the PL from unintentionally created defects states in DNA-wrapped CNTs and from the intentionally induced defects in alkyl-doped CNTs. The third type of PLE signature was associated with CNT quantum dots (QD), characterized by FWHM spectral linewidth below 300 µeV, and was only observed for CNTs grown by CVD. These PL emitters did not exhibit the PLE resonances characteristic for CNT phonons but only those related to the defect mode and the G-band which all carbon-based crystals have in common. Furthermore no Raman scattering or resonances from high-energy states were observed. In contrast to QDs in suspended CNTs, CNT QDs on hexagonal boron nitride (hBN) acquired an additional resonance at an energy that matched that of the out-of-plane optical phonon in hBN.

The spectral dynamics of CNTs were studied in Chapter 6 on the example of CVD-grown CNTs on silicon oxide (SiO_2) and hBN, where spectral wandering was reduced by an order of magnitude for CNTs on hBN. Surprisingly, a comparison to suspended CNTs revealed spectral diffusion comparable to CNTs on SiO_2 for completely suspended CNTs, but ultra-stable PL emission from locations where CNTs were simultaneously suspended and in contact with a substrate (e.g. at the edge of a trench over which the CNT was suspended). The spectral noise densities for CNTs on SiO_2 and hBN were modeled by a superposition of random telegraph noise (RTN), $1/f$ noise, and white noise. While all PL fluctuations were dominated by RTN, CNTs on hBN exhibited significant $1/f$ noise and vanishing white noise contributions which was the opposite case for CNTs on SiO_2. The experimental results were modeled by simulations based on dipole-dipole interactions of the permanent electric dipole moment of a localized CNT exciton with randomly distributed fluctuating surface charges. The simulations related the white noise component for CNTs on SiO_2 and the $1/f$ noise contribution for CNTs on hBN to

fast charge fluctuations on SiO_2 and to distant accumulations of trap states on hBN, respectively. These accumulations were associated with crystal ridges of the hBN, which was confirmed by atomic force microscopy and Kelvin probe force microscopy. This result demonstrated that spectral noise characteristics can be used to study surface topography. An analysis of the spectral dynamics of solution-processed CNTs showed spectral stability comparable to as-grown CNTs on SiO_2, independent of CNT filling or surfactant. The corresponding noise spectral densities, however, deviated significantly from the results obtained for as-grown CNTs and it was impossible to model them by the simulations used for as-grown CNTs. This discrepancy between as-grown and solution-processed CNTs is most likely related to the fact that the PL of the surfactant-coated CNTs stemmed from delocalized excitons which would be in accord with the results obtained by PLE spectroscopy.

In conclusion, the studies in this work identified various cryogenic CNT PL signatures and the external factors influencing them. It has been shown that surfactant agents can have a significant impact on the PL emission energy of cryogenic CNTs, which so far has been neglected in most studies. An interesting direction of future research is the dependence of the spectral lineshape of the PL from localized excitons on the CNT surfactant and filling. The independence of the nanotube PL to CNT filling and surfactant found in this work may be related to the absence of exciton localization, since localized excitons are a key factor in the established models to explain the various PL lineshapes observed for cryogenic CNTs [87, 112, 113].

Fluctuations of surface charges that interact with the permanent electric dipole moment of localized CNT excitons were identified as the origin of detrimental spectral PL fluctuations. On the other hand, the susceptibility of localized CNT excitons to electric fields makes them a promising candidate for nanoscale electrometers with all-optical read-out that can be used for spatial imaging by attaching the CNT to the tip of an AFM cantilever. Experiments can be performed to inspect the electrostatic stability of various dielectric substrates and environments using the PL of chemically doped CNTs [34, 37, 39, 45] where defect-localized excitons exhibit dipole moments [117] of the order of 1 eÅ [41]. For such dipole moments, an elementary charge in a distance of 10 nm would result in a spectral PL shift of ~ 1 meV, a value easily detected with standard spectroscopy. In contrast to alternative all-optical solid-state electrometers in the form of semiconductor quantum dots [137, 146–148] and charged nitrogen vacancy centers in diamond [149, 150], defect-localized excitons in CNTs do not require a surrounding crystal matrix to maintain their photoactivity and thus can serve as sensing elements in scanning-probe electrometry with ultimate proximity to the object of interest.

Bibliography

[1] Feynman, R. P. There's plenty of room at the bottom. *California Institute of Technology Journal of Engineering and Science* **23 (5)**, 22–36 (1960).

[2] Iijima, S. Helical microtubules of graphitic carbon. *Nature* **354**, 56–58 (1991).

[3] Zhang, R. *et al.* Growth of half-meter long carbon nanotubes based on Schulz-Flory distribution. *ACS Nano* **7**, 6156–6161 (2013).

[4] Saito, R., Dresselhaus, G. & Dresselhaus, M. S. *Physical Properties of Carbon Nanotubes* (Imperial College Press, London, 1998).

[5] Dresselhaus, M. S., Dreselhaus, G. & Avouris, P. (eds.) *Carbon Nanotubes: Synthesis, Structure, Properties, and Applications* (Springer-Verlag Berlin Heidelberg New York, 2001).

[6] O'Connell, M. J. *et al.* Band gap fluorescence from individual single-walled carbon nanotubes. *Science* **297**, 593–596 (2002).

[7] Bachilo, S. M. *et al.* Structure-assigned optical spectra of single-walled carbon nanotubes. *Science* **298**, 2361–2366 (2002).

[8] Avouris, P., Freitag, M. & Perebeinos, V. Carbon-nanotube photonics and optoelectronics. *Nat. Photonics* **2**, 341–350 (2008).

[9] Freitag, M., Martin, Y., Misewich, J. A., Martel, R. & Avouris, P. Photoconductivity of single carbon nanotubes. *Nano Lett.* **3**, 1067–1071 (2003).

[10] Pradhan, B., Setyowati, K., Liu, H., Waldeck, D. H. & Chen, J. Carbon nanotube-polymer nanocomposite infrared sensor. *Nano Lett.* **8**, 1142–1146 (2008).

[11] Lu, R., Christianson, C., Kirkeminde, A., Ren, S. & Wu, J. Extraordinary photocurrent harvesting at type-II heterojunction interfaces: Toward high detectivity carbon nanotube infrared detectors. *Nano Lett.* **12**, 6244–6249 (2012).

[12] Lee, J. U. Photovoltaic effect in ideal carbon nanotube diodes. *Appl. Phys. Lett.* **87**, 073101 (2005).

[13] Chen, C., Lu, Y., Kong, E. S., Zhang, Y. & Lee, S.-T. Nanowelded carbon-nanotube-based solar microcells. *Small* **4**, 1313–1318 (2008).

[14] Wang, S. *et al.* Photovoltaic effects in asymmetrically contacted CNT barrier-free bipolar diode. *J. Phys. Chem. C* **113**, 6891–6893 (2009).

[15] Mueller, T. *et al.* Efficient narrow-band light emission from a single carbon nanotube p-n diode. *Nat. Nanotechnol.* **5**, 27–31 (2010).

[16] Wang, S. *et al.* High-performance carbon nanotube light-emitting diodes with asymmetric contacts. *Nano Lett.* **11**, 23–29 (2011).

[17] Ma, Y.-Z., Valkunas, L., Bachilo, S. M. & Fleming, G. R. Exciton binding energy in semiconducting single-walled carbon nanotubes. *The Journal of Physical Chemistry B* **109**, 15671–15674 (2005).

[18] Wang, F., Dukovic, G., Brus, L. E. & Heinz, T. F. The optical resonances in carbon nanotubes arise from excitons. *Science* **308**, 838–841 (2005).

[19] Maultzsch, J. *et al.* Exciton binding energies in carbon nanotubes from two-photon photoluminescence. *Phys. Rev. B* **72**, 241402 (2005).

[20] Lüer, L. *et al.* Size and mobility of excitons in (6, 5) carbon nanotubes. *Nat. Phys.* **5**, 54–58 (2009).

[21] Yoshikawa, K., Matsuda, K. & Kanemitsu, Y. Exciton transport in suspended single carbon nanotubes studied by photoluminescence imaging spectroscopy. *The Journal of Physical Chemistry C* **114**, 4353–4356 (2010).

[22] Moritsubo, S. *et al.* Exciton diffusion in air-suspended single-walled carbon nanotubes. *Phys. Rev. Lett.* **104**, 247402 (2010).

[23] Hertel, T., Himmelein, S., Ackermann, T., Stich, D. & Crochet, J. Diffusion limited photoluminescence quantum yields in 1-D semiconductors: Single-wall carbon nanotubes. *ACS Nano* **4**, 7161–7168 (2010).

[24] Xie, J., Inaba, T., Sugiyama, R. & Homma, Y. Intrinsic diffusion length of excitons in long single-walled carbon nanotubes from photoluminescence spectra. *Phys. Rev. B* **85**, 085434 (2012).

[25] Htoon, H., O'Connell, M. J., Cox, P. J., Doorn, S. K. & Klimov, V. I. Low temperature emission spectra of individual single-walled carbon nanotubes: Multiplicity of subspecies within single-species nanotube ensembles. *Phys. Rev. Lett.* **93**, 027401 (2004).

[26] Lefebvre, J., Finnie, P. & Homma, Y. Temperature-dependent photoluminescence from single-walled carbon nanotubes. *Phys. Rev. B* **70**, 045419 (2004).

[27] Hagen, A. *et al.* Exponential decay lifetimes of excitons in individual single-walled carbon nanotubes. *Phys. Rev. Lett.* **95**, 197401 (2005).

[28] Högele, A., Galland, C., Winger, M. & Imamoğlu, A. Photon antibunching in the photoluminescence spectra of a single carbon nanotube. *Phys. Rev. Lett.* **100**, 217401 (2008).

[29] Walden-Newman, W., Sarpkaya, I. & Strauf, S. Quantum light signatures and nanosecond spectral diffusion from cavity-embedded carbon nanotubes. *Nano Lett.* **12**, 1934–1941 (2012).

[30] Hofmann, M. S. *et al.* Bright, long-lived and coherent excitons in carbon nanotube quantum dots. *Nat. Nanotechnol.* **8**, 502–505 (2013).

[31] Sarpkaya, I. *et al.* Prolonged spontaneous emission and dephasing of localized excitons in air-bridged carbon nanotubes. *Nat. Commun.* **4** (2013).

[32] Jeantet, A. *et al.* Widely tunable single-photon source from a carbon nanotube in the purcell regime. *Phys. Rev. Lett.* **116**, 247402 (2016).

[33] Hofmann, M. S., Noé, J., Kneer, A., Crochet, J. J. & Högele, A. Ubiquity of exciton localization in cryogenic carbon nanotubes. *Nano Lett.* **16**, 2958–2962 (2016).

[34] Ghosh, S., Bachilo, S. M., Simonette, R. A., Beckingham, K. M. & Weisman, R. B. Oxygen doping modifies near-infrared band gaps in fluorescent single-walled carbon nanotubes. *Science* **330**, 1656–1659 (2010).

[35] Ma, X. *et al.* Electronic structure and chemical nature of oxygen dopant states in carbon nanotubes. *ACS Nano* **8**, 10782–10789 (2014).

[36] Ma, X., Baldwin, J. K. S., Hartmann, N. F., Doorn, S. K. & Htoon, H. Solid-state approach for fabrication of photostable, oxygen-doped carbon nanotubes. *Adv. Funct. Mater.* **25**, 6157–6164.

[37] Piao, Y. *et al.* Brightening of carbon nanotube photoluminescence through the incorporation of sp^3 defects. *Nat. Chem.* **5**, 840–845 (2013).

[38] Kwon, H. *et al.* Molecularly tunable fluorescent quantum defects. *J. Am. Chem. Soc.* **138**, 6878–6885 (2016).

[39] Ma, X., Hartmann, N. F., Baldwin, J. K. S., Doorn, S. K. & Htoon, H. Room-temperature single-photon generation from solitary dopants of carbon nanotubes. *Nat. Nanotechnol.* **10**, 671–675 (2015).

[40] He, X. *et al.* Tunable room-temperature single-photon emission at telecom wavelengths from sp3 defects in carbon nanotubes. *Nat. Photonics* **11**, 577 (2017).

[41] Glückert, J. T. *et al.* Dipolar and charged localized excitons in carbon nanotubes. *Phys. Rev. B* **98**, 195413 (2018).

[42] Noé, J. C. *et al.* Environmental electrometry with luminescent carbon nanotubes. *Nano Lett.* **18**, 4136–4140 (2018).

[43] Matsuda, K. *et al.* Photoluminescence intermittency in an individual single-walled carbon nanotube at room temperature. *Appl. Phys. Lett.* **86**, 123116 (2005).

[44] Lefebvre, J. *et al.* High-purity semiconducting single-walled carbon nanotubes: A key enabling material in emerging electronics. *Acc. Chem. Res.* **50**, 2479–2486 (2017).

[45] Miyauchi, Y. *et al.* Brightening of excitons in carbon nanotubes on dimensionality modification. *Nat. Photonics* **7**, 715–719 (2013).

[46] He, X. *et al.* Low-temperature single carbon nanotube spectroscopy of sp3 quantum defects. *ACS Nano* **11**, 10785–10796 (2017).

[47] Ajiki, H. & Ando, T. Aharonov-Bohm effect in carbon nanotubes. *Physica B* **201**, 349–352 (1994).

[48] Miyauchi, Y., Oba, M. & Maruyama, S. Cross-polarized optical absorption of single-walled nanotubes by polarized photoluminescence excitation spectroscopy. *Phys. Rev. B* **74**, 205440 (2006).

[49] Saito, R., Dresselhaus, G. & Dresselhaus, M. S. Trigonal warping effect of carbon nanotubes. *Phys. Rev. B* **61**, 2981–2990 (2000).

[50] Weisman, R. B. & Bachilo, S. M. Dependence of optical transition energies on structure for single-walled carbon nanotubes in aqueous suspension: An empirical Kataura plot. *Nano Lett.* **3**, 1235–1238 (2003).

[51] Kataura, H. *et al.* Optical properties of single-wall carbon nanotubes. *Synth. Met.* **103**, 2555–2558 (1999).

[52] Kane, C. L. & Mele, E. J. Ratio problem in single carbon nanotube fluorescence spectroscopy. *Phys. Rev. Lett.* **90**, 207401 (2003).

[53] Shaver, J. & Kono, J. Temperature-dependent magneto-photoluminescence spectroscopy of carbon nanotubes: evidence for dark excitons. *Laser & Photonics Reviews* **1**, 260–274 (2007).

[54] Ando, T. Excitons in carbon nanotubes. *J. Phys. Soc. Jpn.* **66**, 1066–1073 (1997).

[55] Dukovic, G. *et al.* Structural dependence of excitonic optical transitions and band-gap energies in carbon nanotubes. *Nano Lett.* **5**, 2314–2318 (2005).

[56] Walsh, A. G. *et al.* Scaling of exciton binding energy with external dielectric function in carbon nanotubes. *Physica E: Low-dimensional Systems and Nanostructures* **40**, 2375–2379 (2008).

[57] Kane, C. L. & Mele, E. J. Electron interactions and scaling relations for optical excitations in carbon nanotubes. *Phys. Rev. Lett.* **93**, 197402 (2004).

[58] Ando, T. Effects of valley mixing and exchange on excitons in carbon nanotubes with Aharonov-Bohm flux. *J. Phys. Soc. Jpn.* **75**, 024707 (2006).

[59] Spataru, C. D., Ismail-Beigi, S., Capaz, R. B. & Louie, S. G. Theory and *ab initio* calculation of radiative lifetime of excitons in semiconducting carbon nanotubes. *Phys. Rev. Lett.* **95**, 247402 (2005).

[60] Perebeinos, V., Tersoff, J. & Avouris, P. Scaling of excitons in carbon nanotubes. *Phys. Rev. Lett.* **92**, 257402 (2004).

[61] Zhao, H. & Mazumdar, S. Electron-electron interaction effects on the optical excitations of semiconducting single-walled carbon nanotubes. *Phys. Rev. Lett.* **93**, 157402 (2004).

[62] Dresselhaus, M., Dresselhaus, G., Saito, R. & Jorio, A. Raman spectroscopy of carbon nanotubes. *Phys. Rep.* **409**, 47–99 (2005).

[63] Thomsen, C. & Reich, S. *Raman Scattering in Carbon Nanotubes*, 115–234 (Springer Berlin Heidelberg, 2007).

[64] Saito, R., Fantini, C. & Jiang, J. *Excitonic States and Resonance Raman Spectroscopy of Single-Wall Carbon Nanotubes*, 251–286 (Springer, 2008).

[65] Jorio, A. *et al.* Resonance Raman spectroscopy (n, m)-dependent effects in small-diameter single-wall carbon nanotubes. *Phys. Rev. B* **71**, 075401 (2005).

[66] Araujo, P. T. *et al.* Nature of the constant factor in the relation between radial breathing mode frequency and tube diameter for single-wall carbon nanotubes. *Phys. Rev. B* **77**, 241403 (2008).

[67] Jorio, A. *et al.* G-band resonant Raman study of 62 isolated single-wall carbon nanotubes. *Phys. Rev. B* **65**, 155412 (2002).

[68] Kobayashi, Y., Takagi, D., Ueno, Y. & Homma, Y. Characterization of carbon nanotubes suspended between nanostructures using micro-Raman spectroscopy. *Physica E* **24**, 26–31 (2004).

[69] Lee, S., Peng, J.-W. & Liu, C.-H. Probing plasma-induced defect formation and oxidation in carbon nanotubes by Raman dispersion spectroscopy. *Carbon* **47**, 3488–3497 (2009).

[70] Georgi, C. & Hartschuh, A. Tip-enhanced raman spectroscopic imaging of localized defects in carbon nanotubes. *Appl. Phys. Lett.* **97**, 143117 (2010).

[71] Irurzun, V. M., Ruiz, M. P. & Resasco, D. E. Raman intensity measurements of single-walled carbon nanotube suspensions as a quantitative technique to assess purity. *Carbon* **48**, 2873–2881 (2010).

[72] Glückert, J. T. *Optical spectroscopy of individual single-walled carbon nanotubes in an electric gate structure: tuning the photoluminescence with electric fields*. Dissertation, Ludwig-Maximilians-Universität München (2014).

[73] Sanchez-Valencia, J. R. *et al.* Controlled synthesis of single-chirality carbon nanotubes. *Nature* **512**, 61–64 (2014).

[74] Yang, F. *et al.* Chirality-specific growth of single-walled carbon nanotubes on solid alloy catalysts. *Nature* **510**, 522–524 (2014).

[75] Hofmann, M. S. *Spectroscopy of localized excitons in carbon nanotubes*. Dissertation, Ludwig-Maximilians-Universität München (2016).

[76] Hofmann, M. S. *et al.* Synthesis and cryogenic spectroscopy of narrow-diameter single-wall carbon nanotubes. *Carbon* **105**, 622–627 (2016).

[77] Baumgartner, A. *et al.* Carbon nanotube quantum dots on hexagonal boron nitride. *Appl. Phys. Lett.* **105**, 023111 (2014).

[78] Campo, J. *et al.* Enhancing single-wall carbon nanotube properties through controlled endohedral filling. *Nanoscale Horiz.* **1**, 317–324 (2016).

[79] Streit, J. *et al.* Alkane encapsulation induces strain in small-diameter single-wall carbon nanotubes. *The Journal of Physical Chemistry C* **122**, 11577–11585 (2018).

[80] Ao, G., Streit, J. K., Fagan, J. A. & Zheng, M. Differentiating left- and right-handed carbon nanotubes by DNA. *J. Am. Chem. Soc.* **138**, 16677–16685 (2016).

[81] Koyama, K., Yoshita, M., Baba, M., Suemoto, T. & Akiyama, H. High collection efficiency in fluorescence microscopy with a solid immersion lens. *Appl. Phys. Lett.* **75**, 1667–1669 (1999).

[82] Karrai, K., Lorenz, X. & Novotny, L. Enhanced reflectivity contrast in confocal solid immersion lens microscopy. *Appl. Phys. Lett.* **77**, 3459–3461 (2000).

[83] Lee, K. G. *et al.* A planar dielectric antenna for directional single-photon emission and near-unity collection efficiency. *Nat. Photonics* **5**, 166 (2011).

[84] Wenseleers, W., Cambré, S., Čulin, J., Bouwen, A. & Goovaerts, E. Effect of water filling on the electronic and vibrational resonances of carbon nanotubes: Characterizing tube opening by Raman spectroscopy. *Adv. Mater.* **19**, 2274–2278 (2007).

[85] Ma, X., Cambré, S., Wenseleers, W., Doorn, S. K. & Htoon, H. Quasiphase transition in a single file of water molecules encapsulated in (6,5) carbon nanotubes observed by temperature-dependent photoluminescence spectroscopy. *Phys. Rev. Lett.* **118**, 027402 (2017).

[86] Krummheuer, B., Axt, V. M. & Kuhn, T. Theory of pure dephasing and the resulting absorption line shape in semiconductor quantum dots. *Phys. Rev. B* **65**, 195313 (2002).

[87] Galland, C., Högele, A., Türeci, H. E. & Imamoğlu, A. Non-Markovian decoherence of localized nanotube excitons by acoustic phonons. *Phys. Rev. Lett.* **101**, 067402 (2008).

[88] Yang, L. & Han, J. Electronic structure of deformed carbon nanotubes. *Phys. Rev. Lett.* **85**, 154–157 (2000).

[89] Huang, M. *et al.* Direct measurement of strain-induced changes in the band structure of carbon nanotubes. *Phys. Rev. Lett.* **100**, 136803 (2008).

[90] Leeuw, T. K. *et al.* Strain measurements on individual single-walled carbon nanotubes in a polymer host: Structure-dependent spectral shifts and load transfer. *Nano Lett.* **8**, 826–831 (2008).

[91] Kiowski, O. *et al.* Photoluminescence microscopy of carbon nanotubes grown by chemical vapor deposition: Influence of external dielectric screening on optical transition energies. *Phys. Rev. B* **75**, 075421 (2007).

[92] Miyauchi, Y. *et al.* Dependence of exciton transition energy of single-walled carbon nanotubes on surrounding dielectric materials. *Chem. Phys. Lett.* **442**, 394–399 (2007).

[93] Ohno, Y. *et al.* Excitonic transition energies in single-walled carbon nanotubes: Dependence on environmental dielectric constant. *Physica Status Solidi (b)* **244**, 4002–4005 (2007).

[94] White, G. K. Thermal expansion of reference materials: copper, silica and silicon. *J. Phys. D: Appl. Phys.* **6**, 2070 (1973).

[95] Kwon, Y.-K., Berber, S. & Tománek, D. Thermal contraction of carbon fullerenes and nanotubes. *Phys. Rev. Lett.* **92**, 015901 (2004).

[96] Karaiskaj, D., Engtrakul, C., McDonald, T., Heben, M. J. & Mascarenhas, A. Intrinsic and extrinsic effects in the temperature-dependent photoluminescence of semiconducting carbon nanotubes. *Phys. Rev. Lett.* **96**, 106805 (2006).

[97] Capaz, R. B., Spataru, C. D., Tangney, P., Cohen, M. L. & Louie, S. G. Temperature dependence of the band gap of semiconducting carbon nanotubes. *Phys. Rev. Lett.* **94**, 036801 (2005).

[98] Lefebvre, J. & Finnie, P. Polarized photoluminescence excitation spectroscopy of single-walled carbon nanotubes. *Phys. Rev. Lett.* **98**, 167406 (2007).

[99] Htoon, H., O'Connell, M. J., Doorn, S. K. & Klimov, V. I. Single carbon nanotubes probed by photoluminescence excitation spectroscopy: The role of phonon-assisted transitions. *Phys. Rev. Lett.* **94**, 127403 (2005).

[100] Stephanie Reich, J. M., Christian Thomsen. *Carbon Nanotubes: Basic Concepts and Physical Properties* (John Wiley and Sons, 2004).

[101] Dresselhaus, M. S., Jorio, A., Hofmann, M., Dresselhaus, G. & Saito, R. Perspectives on carbon nanotubes and graphene Raman spectroscopy. *Nano Lett.* **10**, 751–758 (2010).

[102] Saito, R., Hofmann, M., Dresselhaus, G., Jorio, A. & Dresselhaus, M. S. Raman spectroscopy of graphene and carbon nanotubes. *Adv. Phys.* **60**, 413–550 (2011).

[103] Jorio, A., Dresselhaus, M. S., Saito, R. & Dresselhaus, G. F. *Raman Spectroscopy in Graphene Related Systems* (John Wiley and Sons, 2011).

[104] Fantini, C. *et al.* Steplike dispersion of the intermediate-frequency Raman modes in semiconducting and metallic carbon nanotubes. *Phys. Rev. B* **72**, 085446 (2005).

[105] Chou, S. G. *et al.* Phonon-assisted excitonic recombination channels observed in DNA-wrapped carbon nanotubes using photoluminescence spectroscopy. *Phys. Rev. Lett.* **94**, 127402 (2005).

[106] Luo, Z., Papadimitrakopoulos, F. & Doorn, S. K. Intermediate-frequency Raman modes for the lower optical transitions of semiconducting single-walled carbon nanotubes. *Phys. Rev. B* **75**, 205438 (2007).

[107] Luo, Z., Papadimitrakopoulos, F. & Doorn, S. K. Bundling effects on the intensities of second-order Raman modes in semiconducting single-walled carbon nanotubes. *Phys. Rev. B* **77**, 035421 (2008).

[108] Lim, Y.-S. *et al.* Ultrafast generation of fundamental and multiple-order phonon excitations in highly enriched (6,5) single-wall carbon nanotubes. *Nano Lett.* **14**, 1426–1432 (2014).

[109] Lefebvre, J. & Finnie, P. Excited excitonic states in single-walled carbon nanotubes. *Nano Lett.* **8**, 1890–1895 (2008).

[110] Uda, T., Yoshida, M., Ishii, A. & Kato, Y. K. Electric-field induced activation of dark excitonic states in carbon nanotubes. *Nano Lett.* **16**, 2278–2282 (2016).

[111] Capaz, R. B., Spataru, C. D., Ismail-Beigi, S. & Louie, S. G. Diameter and chirality dependence of exciton properties in carbon nanotubes. *Phys. Rev. B* **74**, 121401 (2006).

[112] Vialla, F. *et al.* Unifying the low-temperature photoluminescence spectra of carbon nanotubes: The role of acoustic phonon confinement. *Phys. Rev. Lett.* **113**, 057402 (2014).

[113] Sarpkaya, I. *et al.* Strong acoustic phonon localization in copolymer-wrapped carbon nanotubes. *ACS Nano* **9**, 6383–6393 (2015).

[114] Jeantet, A., Chassagneux, Y., Claude, T., Lauret, J. S. & Voisin, C. Interplay of spectral diffusion and phonon-broadening in individual photo-emitters: the case of carbon nanotubes. *Nanoscale* **10**, 683–689 (2018).

[115] Serrano, J. *et al.* Vibrational properties of hexagonal boron nitride: Inelastic x-ray scattering and ab initio calculations. *Phys. Rev. Lett.* **98**, 095503 (2007).

[116] Jin, C. *et al.* Interlayer electron-phonon coupling in WSe2/hBN heterostructures. *Nat. Phys.* **13**, 127 (2016).

[117] Hartmann, N. F. *et al.* Photoluminescence imaging of solitary dopant sites in covalently doped single-wall carbon nanotubes. *Nanoscale* **7**, 20521–20530 (2015).

[118] Fratini, S. & Guinea, F. Substrate-limited electron dynamics in graphene. *Phys. Rev. B* **77**, 195415 (2008).

[119] Tans, S. J., Verschueren, A. R. M. & Dekker, C. Room-temperature transistor based on a single carbon nanotube. *Nature* **393**, 49–52 (1998).

[120] Martel, R., Schmidt, T., Shea, H. R., Hertel, T. & Avouris, P. Single- and multi-wall carbon nanotube field-effect transistors. *Appl. Phys. Lett.* **73**, 2447–2449 (1998).

[121] Lin, M. *et al.* Dynamical observation of bamboo-like carbon nanotube growth. *Nano Lett.* **7**, 2234–2238 (2007).

[122] Collins, P. G., Bradley, K., Ishigami, M. & Zettl, A. Extreme oxygen sensitivity of electronic properties of carbon nanotubes. *Science* **287**, 1801–1804 (2000).

[123] Star, A., Gabriel, J.-C. P., Bradley, K. & Grüner, G. Electronic detection of specific protein binding using nanotube FET devices. *Nano Lett.* **3**, 459–463 (2003).

[124] Dean, C. R. *et al.* Boron nitride substrates for high-quality graphene electronics. *Nat. Nanotechnol.* **5**, 722–726 (2010).

[125] Xue, J. M. *et al.* Scanning tunnelling microscopy and spectroscopy of ultra-flat graphene on hexagonal boron nitride. *Nat. Mater.* **10**, 282–285 (2011).

[126] Engels, S. *et al.* Etched graphene quantum dots on hexagonal boron nitride. *Appl. Phys. Lett.* **103**, 073113 (2013).

[127] Manca, M. *et al.* Enabling valley selective exciton scattering in monolayer WSe_2 through upconversion. *Nat. Commun.* **8**, 14927 (2017).

[128] Cadiz, F. *et al.* Excitonic Linewidth Approaching the Homogeneous Limit in MoS_2 -Based van der Waals Heterostructures. *Phys. Rev. X* **7**, 021026 (2017).

[129] Ajayi, O. A. *et al.* Approaching the intrinsic photoluminescence linewidth in transition metal dichalcogenide monolayers. *2D Mater.* **4**, 031011 (2017).

[130] Wierzbowski, J. *et al.* Direct exciton emission from atomically thin transition metal dichalcogenide heterostructures near the lifetime limit. *Sci. Rep.* **7**, 12383– (2017).

[131] Allan, D. W. Should the Classical Variance Be Used As a Basic Measure in Standards Metrology? *IEEE Trans. Instrum. Meas.* **IM-36**, 646–654 (1987).

[132] Barnes, J. A. *et al.* Characterization of frequency stability. *IEEE Trans. Instrum. Meas.* **1001**, 105 (1971).

[133] Robinson, H. & Goldberg, B. Light-induced spectral diffusion in single self-assembled quantum dots. *Phys. Rev. B* **61**, 5086(R)–5089(R) (2000).

[134] Santos, S. M. *et al.* All-optical trion generation in single-walled carbon nanotubes. *Phys. Rev. Lett.* **107**, 187401 (2011).

[135] Kumamoto, Y. *et al.* Spontaneous exciton dissociation in carbon nanotubes. *Phys. Rev. Lett.* **112**, 117401 (2014).

[136] Xiao, Y.-F., Nhan, T. Q., Wilson, M. W. B. & Fraser, J. M. Saturation of the photoluminescence at few-exciton levels in a single-walled carbon nanotube under ultrafast excitation. *Phys. Rev. Lett.* **104**, 017401 (2010).

[137] Kuhlmann, A. V. *et al.* Charge noise and spin noise in a semiconductor quantum device. *Nat. Phys.* **9**, 570 (2013).

[138] Cleland, A. N. & Roukes, M. L. A nanometre-scale mechanical electrometer. *Nature* **392**, 160–162 (1998).

[139] Pelton, M., Grier, D. G. & Guyot-Sionnest, P. Characterizing quantum-dot blinking using noise power spectra. *Appl. Phys. Lett.* **85**, 819–821 (2004).

[140] Zhang, Y., Moser, J., Güttinger, J., Bachtold, A. & Dykman, M. I. Interplay of driving and frequency noise in the spectra of vibrational systems. *Phys. Rev. Lett.* **113**, 1–6 (2014).

[141] Hooge, F. N., Kleinpenning, T. G. M. & Vandamme, L. K. J. Experimental studies on l/f noise. *Rep. Prog. Phys.* **44**, 479–532 (1981).

[142] McWhorter, A. L. *1/f noise and germanium surface properties; Semicond. Surf. Phys.* (University of Pennsylvania Press, 1957).

[143] Terman, L. An investigation of surface states at a silicon/silicon oxide interface employing metal-oxide-silicon diodes. *Solid-State Electron.* **5**, 285 – 299 (1962).

[144] Xiang, R. *et al.* One-dimensional van der Waals heterostructures. *arXiv e-prints* arXiv:1807.06154 (2018).

[145] Ma, X. *et al.* Influence of exciton dimensionality on spectral diffusion of single-walled carbon nanotubes. *ACS Nano* **8**, 10613–10620 (2014).

[146] Vamivakas, A. N. *et al.* Nanoscale optical electrometer. *Phys. Rev. Lett.* **107**, 166802 (2011).

[147] Houel, J. *et al.* Probing single-charge fluctuations at a GaAs/AlAs interface using laser spectroscopy on a nearby InGaAs quantum dot. *Phys. Rev. Lett.* **108**, 107401 (2012).

[148] Hauck, M. *et al.* Locating environmental charge impurities with confluent laser spectroscopy of multiple quantum dots. *Phys. Rev. B* **90**, 235306 (2014).

[149] Dolde, F. *et al.* Electric-field sensing using single diamond spins. *Nat. Phys.* **7**, 459 (2011).

[150] Dolde, F. *et al.* Nanoscale detection of a single fundamental charge in ambient conditions using the NV^- center in diamond. *Phys. Rev. Lett.* **112**, 097603 (2014).

List of abbreviations

1D	one-dimensional
2D	two-dimensional
3D	three-dimensional
AFM	atomic force microscopy
APD	avalanche photodiode
CCD	charge-coupled device
CNT	carbon nanotube
CVD	chemical vapor deposition
cw	continuous wave
DNA	deoxyribonucleic acid
DOC	sodium deoxycholate
DOS	density of states
FWHM	full-width at half-maximum
hBN	hexagonal boron nitride
iTA	in-plane transverse acoustic
iTO	in-plane transverse optical
KPFM	Kelvin probe force microscopy
LA	longitudinal acoustic
LO	longitudinal optical
oTO	out-of-plane transverse optical
PL	photoluminescence

PLE photoluminescence excitation

RBM radial breathing mode

RTN random telegraph noise

SEM scanning electron microscopy

SiO_2 silicon oxide

VHs Van Hove singularity

List of publications

- M. S. Hofmann, J. T. Glückert, J. Noé, C. Bourjau, R. Dehmel & A. Högele
  Bright, long-lived and coherent excitons in carbon nanotube quantum dots
  Nature Nanotechnology **8**, 502–505 (2013)

- D. Ehberger, J. Hammer, M. Eisele, M. Krüger, J. Noé, A. Högele & P. Hommelhoff
  Highly coherent electron beam from a laser-triggered tungsten needle tip
  Physical Review Letters **114**, 227601 (2015)

- M. S. Hofmann, J. Noé, A. Kneer, J. J. Crochet & A. Högele
  Ubiquity of exciton localization in cryogenic carbon nanotubes
  Nano Letters **16**, 2958–2962 (2016)

- M. S. Hofmann, J. Noé, M. Nutz, A. Kneer, R. Dehmel, L. Schaffroth & A. Högele
  Synthesis and cryogenic spectroscopy of narrow-diameter single-wall carbon nanotubes
  Carbon **105**, 622–627 (2016)

- T. Hümmer, J. Noé, M. S. Hofmann, T. W. Hänsch, A. Högele & D. Hunger
  Cavity-enhanced Raman microscopy of individual carbon nanotubes
  Nature Communications **7**, 12155 (2016)

- J. Noé, M. Nutz, J. Reschauer, N. Morell, I. Tsioutsios, A. Reserbat-Plantey, K. Wakanabe, T.Taniguchi, A. Bachtold & A. Högele
  Environmental electrometry with luminescent carbon nanotubes
  Nano Letters **18**, 4136–4140 (2018)

Danksagung

Hiermit möchte ich allen danken, die mich während meiner Promotion unterstützt und begleitet haben. Ihr alle habt dazu beigetragen, dass ich meine Doktorandenzeit, trotz der üblichen Rückschläge und Frustrationen, sehr genossen habe!

Besonderer Dank gilt Alexander Högele, der mir die Möglichkeit gegeben hat in seiner Gruppe zu forschen und zu promovieren und der gerade in schwierigen Episoden immer sehr motivierend und unterstützend war. Danke dir auch für die inspirierenden Gespräche und die Unterstützung beim Proof of Concept Antrag, die dazu geführt hat, dass ich voll Freude und Spannung auf die Zeit nach meiner Promotion blicken kann!

Vielen Dank an meine beiden Nanotube-Kollegen Matthias Hofmann und Manuel Nutz. Euer trockener Humor und das richtige Verhältnis von Ernsthaftigkeit, Spaß und Ironie bei der Arbeit haben meinen Alltag sehr bereichert. Danke dir Matthias für die Einführung in alle Experimente, die Möglichkeit immer nachfragen zu können und die tolle Zeit in Japan. Vielen Dank Manuel für das Teilen des Leides im Labor (Ethalon!), die Unterstützung bei Experimenten, die hilfreichen Anmerkungen beim Paperschreiben und Datenauswerten und das Korrekturlesen dieser Arbeit. Nicht zu vergessen die umfangreiche Hilfe bei allen Computerproblemen die es fast erträglich gemacht hat mit Windows zu arbeiten.

Neben Manuel und Matthias auch noch Danke an meine übrigen Bürokollegen Jessica Lindlau, Jonathan Förste, Michael Förg, Victor Funk (Boulderinstructor und Hüttenguru) und Enrico Schubert für die lustigen Gespräche, die gemeinsamen Mittagessen, die Filmabende, Wiesnbesuche und Bartouren. Vielen Dank auch an die anderen Nanophotoniker Jan Glückert, Matthias Hauck, Sarah Wittig, Andre Neumann, Leo Colombier und Samarth Vadia für die entspannte Atmosphäre und Hilfsbereitschaft, sowie an Jiaxiang Zhang und die Masterstundenten Jodok Happacher und Jonathan Reschauer für die Hilfe im Labor. Es waren tolle fünf Jahre mit euch und ich werde diese Zeit in sehr guter Erinnerung behalten.

Jörg Kotthaus möchte ich dafür danken, dass er diesen tollen Lehrstuhl aufgebaut hat, und Bert Lorenz dafür, dass er Sorge trägt, dass nicht alles zusammenbricht. Dank geht auch an Reinhold Rath für die Hilfe mit Strom, Wasser, Pumpen und beim Durchbohren dicker Wände zusammen mit Anton Heindl der dafür gesorgt hat, dass immer genug Helium und Stickstoff da waren. Für die kompetente Beratung und Hilfe beim Abarbeiten jeglicher Unibürokratie danke ich Martina Edenhofer. Danke an Philipp Altpeter

für die tolle Betreuung bei allen Reinraumarbeiten, ganz besonders bei der Mikrostrukturierung und an Stephan Manus für die große Unerstützung in elektrotechnischen Angelegenheiten.

Danke auch an Thomas Hümmer und David Hunger, für die gemeinsamen Projekte in der Vergangenheit und in der Zukunft.

Großer Dank geht an meine Eltern Doris und Christian, die mir meine Ausbildung ermöglicht haben und mich immer darin unterstützt haben, der Mensch zu werden, der ich heute bin.

Vielen Dank Eva, dass du ein so wunderbarer Ausgleich zu meiner Arbeit bist, dich immer für das Befinden meiner Nanoröhren interessiert hast und mir in stressigen Zeiten den Rücken freigehalten hast!